Emanuele Lange

Master of Science

Characterization of Electronic States of Volatile Anaesthetics by Electron Energy Loss Spectroscopy and Synchrotron Radiation

Thesis submitted in partial fulfillment
of the requirements for the degree of

Doctor of Philosophy in
Radiation Biology and Biophysics
Applied Atomic and Molecular Physics

Adviser: Professor Paulo Manuel Assis Loureiro Limão Vieira, Full Professor, Universidade NOVA de Lisboa

Co-adviser: Prof. Filipe Ferreira da Silva, Assistant Professor, Universidade NOVA de Lisboa

Examination Committee

Chairperson: Professor Luís Manuel Marques da Costa Caires
Raporteurs: Professor Benilde Simões Mendes
Dr. Samuel Peter Eden
Members: Professor Gustavo Garcia Gomez-Tejedor
Professor Paulo Manuel Assis Loureiro Limão Vieira
Professor Denis Duflot

FACULDADE DE CIÊNCIAS E TECNOLOGIA
UNIVERSIDADE NOVA DE LISBOA

October, 2019

Characterization of Electronic States of Volatile Anaesthetics by Electron Energy Loss Spectroscopy and Synchrotron Radiation

This document was created using the (pdf)LaTeX processor, based in the "novathesis" template[1], developed at the Dep. Informática of FCT-NOVA [2].
[1] https://github.com/joaomlourenco/novathesis [2] http://www.di.fct.unl.pt

Acknowledgements

My most sincere acknowledgements to Professor Paulo Limão-Vieira and Dr. Filipe Ferreira da Silva for their supervision, constant availability, patient, dedication, and for sharing their knowledge with me over these four years. It was an amazing journey.

To Professor Denis Duflot, for receiving me so well at the University of Lille, patiently teach me the calculation procedures, and clarifying all the countless doubts by email.

To Professor Gustavo García, Professor Márcio Bettega and MSc. Leticia Maioli for the electron scattering calculations and for the collaborative work.

To CNPq agency and the *science without borders* program for the grant scholarship that made this work possible, and to COST Action CM1401 for financial support in the short term scientific mission in University of Lille.

To CEFITEC, the Atomic and Molecular Collisions Laboratory and the department of physics of Universidade NOVA de Lisboa, the RABBIT program and all its coordinators and professors, for making this work possible. To Ana Cruz and Afonso Moutinho, for all the given assistance.

To all the colleges CEFITEC and LCAM lab, Mónica Mendes, Ana Isabel Martínez, Filipa Pires, Alexandra Loupas, Telma Silva, Sara Pereira, Rebecca Meißner, Diego Farago Pastega, Diogo Almeida and Ana Fonseca. And particularly to MSc. Guilherme Meneses for guiding me through the first contacts with the apparatus, to José Romero for develop the data acquisition software, and to MSc. João Ameixa, for all the joint work and partnership.

To my mother, for all the support and encouragement, not just in those five years, but throughout my whole life. You are my strength.

To all the friends I made in Portugal, which were essential to make my life lighter and more enjoyable, especially my dears Patricia, Victor and Alessandra, who were my family in a foreign land.

To my lifetime friends who, even from afar, have always been by my side. Hellen,

Heidemann, Ju, Zé, Ana, Wili, Rose, Maya, Marina, Canziani, Anita, Karine, Feli, Karol, Fer, Celi, Rodolfo, Cris, Uila, Dani e Lucas. Somehow, you were always close to me.

To Francisco Freire, for all your love, kindness, patience and everything else. You are my peace.

The scientist does not study nature because it is useful to do so. He studies it because he takes pleasure in it, and he takes pleasure in it because it is beautiful. If nature were not beautiful it would not be worth knowing, and life would not be worth living. I am not speaking, of course, of the beauty which strikes the senses, of the beauty of qualities and appearances. I am far from despising this, but it has nothing to do with science. What I mean is that more intimate beauty which comes from the harmonious order of its parts, and which a pure intelligence can grasp.

Henri Poincaré

Abstract

Volatile anaesthetics are widely used in clinical practice to induct and maintain anaesthesia through inhalation. The major atmospheric effects that may arise from emission of volatile anaesthetics are their contributions to ozone depletion in the stratosphere and to greenhouse global warming. In this thesis we present spectroscopic studies on UV-radiation and electron interaction with three of the volatile anaesthetics currently in use, sevoflurane ($C_4H_3F_7O$), isoflurane ($C_3H_2ClF_5O$) and halothane ($C_2HBrClF_3$), in order to comprehensively describe the underlying molecular mechanisms of these molecules yielding dissociation. Electron scattering elastic differential cross sections (DCS) by the three mentioned molecules were measured for energies from 8.0 eV to 50 eV. The experimental DCSs and integral cross sections (ICSs) were compared with theoretical calculations, performed by collaborating groups, using two different methodologies, the Schwinger multichannel method (SMC) and the independent atom model–screening corrected additivity rule (IAM-SCAR). Moreover, we present, for the same compounds, results from VUV photoabsorption measurements over the wavelength range 115-220 nm, together with *ab initio* theoretical calculations of the vertical excitation energies and oscillator strength. This combined experimental and theoretical study allows a comprehensive description and characterization of the electronic states of these chemical compounds. The measured photoabsorption cross sections were also used to calculate the photolysis lifetime of the molecules in the Earth's atmosphere from ground level up to the limit of the stratopause.

Keywords: Electron scattering, VUV photoabsorption, isoflurane, sevoflurane, halothane.

Resumo

Anestésicos voláteis são amplamente utilizados na prática clínica, para induzir e manter a anestesia, através da inalação. Os principais efeitos atmosféricos, que podem surgir da emissão de anestésicos voláteis, são suas contribuições para o aquecimento global, e depleção do ozônio na estratosfera. Nesta tese são apresentados estudos sobre interação de electrões e radiação UV com três dos anestésicos voláteis atualmente em uso, sevoflurano ($C_4H_3F_7O$), isoflurano ($C_3H_2ClF_5O$), e halotano ($C_2HBrClF_3$), a fim de descrever de forma abrangente os mecanismos moleculares desses compostos. Secções eficazes diferenciais de dispersão de elétrões pelas três moléculas citadas foram medidas para energias de 8,0 eV a 50 eV. As DCSs e as ICSs experimentais foram comparados com cálculos teóricos, realizados por grupos colaboradores, utilizando duas diferentes metodologias, o método multicanal de Schwinger (SMC) e o *"independent atom model–screening corrected additivity rule"* (IAM-SCAR). Também são apresentados, para os mesmos compostos, os resultados de medidas de fotoabsorção UV na faixa de 115-220 nm, juntamente com cálculos teóricos *ab initio* das energias de excitação verticais e força do oscilador. Este estudo teórico-experimental permite uma descrição abrangente da caracterização dos estados eletrônicos desses compostos químicos. Os espectros de fotoabsorção foram também utilizados para calcular o tempo de vida de fotólise das moléculas citadas.

Palavras-chave: Dispersão de eletrões, espalhamento de elétrons, fotoabsorção, isofluorano, sevofluorano, halotano.

Contents

List of Figures

List of Tables

Acronyms

ASTRID Aarhus storage ring in Denmark.

ASTRID2 Aarhus storage ring in Denmark 3rd generation light source.

CEFITEC Centre of Physics and Technological Research.

CFC chlorofluorocarbons.

CFC-11 trichlorofluoromethane.

CSIC Consejo Superior de Investigaciones Científicas.

DCS differential cross section.

DFT density functional theory.

EOM-CCSD equation-of-motion coupled cluster method restricted to single and double excitations.

FBA first Born approximation.

FCT-UNL faculty of science and technology of NOVA university of Lisbon.

FWHM full width at half maximum.

GWP global warming potential.

HOMO highest occupied molecular orbital.

HOMO-2 third highest occupied molecular orbital.

HOMO-1 second highest occupied molecular orbital.

HREELS high resolution electron energy loss spectrometer.

IAM independent atom model.

IAM-SCAR+I independent atom model - screening corrections additivity rule plus interference.

IAM-SCAR independent atom model - screening corrections additivity rule.

ICS integral cross section.

IE ionisation energy.

LCAM atomic and molecular collision laboratory.

LiF lithium fluorine.

LUMO lowest unoccupied molecular orbital.

LUMO+1 second lowest unoccupied molecular orbital.

MgF_2 magnesium difluorine.

MO molecular orbital.

NTOs natural transition orbitals.

ODP ozone depletion potential.

OVGF Outer Valence Greens Function.

P3 Partial Third Order.

RE radiative efficiency.

SCAR screen corrected additivity rule.

SCF self consistent field.

SE static-exchange.

SE+P static-exchange plus polarization.

SMC Schwinger multichannel.

SMC-PP Schwinger multichannel method implemented with pseudopotential.

STSM short term scientific mission.

TD-DFT time dependent density functional theory.

UFPR Universidade Federal do Paraná.

UV ultraviolet.

VUV vacuum ultraviolet.

Chapter

1 Introduction

There are two objectionable types of believers: those who believe the incredible, and those who believe that 'belief' must be discarded and replaced by 'the scientific method'.
— Max Born, Natural Philosophy of Cause and Chance

1.1 Volatile Anaesthetics

Volatile anaesthetics are commonly used during surgery and other medical, dental and veterinary procedures, with the purpose of making the experience less unpleasant for the patient. Two different types of chemical compounds are present in the most frequently used volatile anaesthetics: nitrous oxide (N_2O) and halogenated compounds. For the purpose of this study, we will leave aside N_2O and focus on the halogenated compounds, more particularly on halothane, sevoflurane and isoflurane.

Methoxyflurane was the first halogenated anaesthetic ever used, in the 1950s, but was phased out in the late 1970s due to medical side effects [1, 2]. Halothane was the most extensively used inhalation anaesthetic until recently, it is no longer used in human anaesthesiology in most developed countries, due to hepatic side effects [1, 3], but it is still used in many underdeveloped countries and also in veterinary procedures. Desflurane is not frequently used, it has several disadvantages which has precluded its use. The most relevants are: it is difficult and expensive to synthesise; its high vapour pressure makes it incompatible with the standard vaporizer machines; it has a pungent smell and can cause irritation on the airways. Desflurane is only recommended to very specific patients, as morbidly obese for example [4]. Enflurane was used from the 1970s to the 1990s [2, 5] and was gradually replaced by isoflurane in the early 1980s, an isomer with some superior medical properties, which continues to be used until today [1, 2, 6]. Sevoflurane is one of

the most recently introduced inhalation anaesthetic, in the mid-1990s [2, 7] and also still in use.

Halogenated compound	**Commercial name**
Halothane	Fluothane
Methoxyflurane	Penthrane
Enflurane	Ethrane
Isoflurane	Forane
Desflurane	Suprane
Sevoflurane	Ultane

Table 1.1: Volatile halogenated anaesthetics compounds most commonly used in medical, dental and veterinary procedures and their respective commercial names. Fluothane is a registered trademark of Wyeth-Ayerst Laboratories, Inc., Penthrane, Ethrane, and Ultane are registered trademarks of Abbott Laboratories, Forane and Suprane are registered trademarks of Baxter Healthcare Corporation. Adapted from [8].

The halogenated compounds are liquid at room temperature, they are vaporized by the anaesthesia machine and then administered to the patient through a mask or breathing tube [8]. It is known that more than 80% of all the inhalation anaesthetic agent is exhaled unchanged by the patient [9] and therefore emitted into the lower atmosphere, which may have environmental consequences. In fact, for isoflurane and sevoflurane, less than 5% of these anaesthetics are metabolised by the patient [8, 10]. Although the total amount of these compounds used globally are not precisely known, it is estimated in the order of 10-12 kilotons per year [9, 11].

1.2 Environmental effects

With the exception of nitrous oxide, all volatile anaesthetics are halogenated chlorofluorocarbons or fluorinated hydrocarbons, which are potentially damaging to the Earth's ozone layer and also contribute to global warming. Although the environmental damage caused by chlorofluorocarbons (CFC) compounds has been discussed since the early 1970s, the first regulation of their use was set only in 1987, with the Montreal Protocol. "*Recognizing that worldwide emissions of certain substances can significantly deplete and otherwise modify the ozone layer in a manner that is likely to result in adverse effects on human health and the environment*"[1], the Montreal Protocol regulated and restrained the use of CFC and halogenated compounds for technical and industrial applications. However the use of some compounds for medical applications was considered as "essential use"and therefore remained unrestricted.

[1] citation from "1987 MONTREAL PROTOCOL ON SUBSTANCES THAT DEPLETE THE OZONE LAYER AS AMENDED 1990, 1992, 1995, 1997, 1999, 2007, 2016".

1.2.1 The Earth's Atmosphere

The atmosphere of the Earth is a gaseous envelope and is divided in layers, according to its temperature profile. It is composed by approximately 78% of nitrogen, 21% of oxygen, and small amounts (less than 1%) of other gases, including carbon dioxide, with a concentration of about 0.04% [9, 12]. The lowest layer is termed troposphere and its temperature decreases with altitude. Its upper limit varies between an altitude of 18 *km*, in the tropics, and 8 *km*, in polar regions. Being denser at low altitudes, this layer contains about 75% of all the atmosphere's mass. Atop the troposphere is located the stratosphere, where temperature increases again with the altitude, and the border between them is the tropospause, which is an inversion region. This temperature behaviour in the stratosphere is due to the absorption of the sun's ultraviolet (UV) radiation by the ozone layer, which is mainly located in the lower portion of the stratosphere, at about 20 to 30 *km* in altitude, however, the presence of ozone gas extends throughout the stratosphere, that reaches 50 *km* above the Earth's surface. The stratosphere is followed by the mesosphere and thermosphere, with upper limit of 80 and 500 *km*, respectively [9, 12]. Processes occurring in these last two layers are not of interest in this study. Hence, in this work, the term "atmosphere"is used to refer to the troposphere and stratosphere.

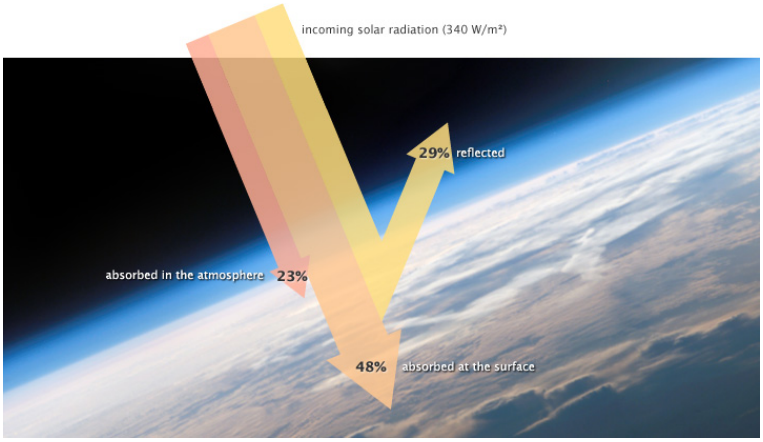

Figure 1.1: Representation of the incoming solar flux: 340 W/m^2 solar energy that falls on the Earth, 29% is reflected back into space, 23% of incoming energy is absorbed in the atmosphere, and the remaining 48% is absorbed at the surface. NASA illustration by Robert Simmon, taken from [13].

The Earth's atmosphere receives energy radiated by the sun, which can be reflected or absorbed and then partially re-emitted. This flow of incoming and outgoing energy is known as *Earth's energy budget*. The energy budget must balance in order to maintain the average temperature on Earth stable over long periods of time. This means that the incoming and outgoing energy have to be equal. The average effective solar flux of incident energy arriving at the top of the atmosphere per unit of time is approximately 340 W/m^2. About 29% of this radiation is reflected back to space by atmospheric particles, clouds, or bright ground surfaces like sea, ice, and snow. The incident energy absorbed in the

atmosphere, by ozone, water vapour and other particles, is 78 W/m^2, and 163 W/m^2 passes through the atmosphere and is absorbed by the Earth surface [12, 14, 15]. So together, approximately 71% of incoming solar radiation is absorbed, and the same amount of energy must leave the atmosphere, in order to balance the Earth's energy budget, thus the average temperature of the planet remains stable.

Three different processes lead the absorbed energy to leave the Earth's surface, represented in Figure 1.2: Thermal radiation, evaporation and convection. About 17% of the incident solar flux is re-emitted as thermal infrared energy, since the Earth works as a blackbody at 288K, and therefore the emission peaks in the infrared spectrum. Approximately 25% is emitted in the form of latent heat, as the incoming solar energy evaporates liquid water and its molecules are spread through the atmosphere. When they condense back into rain, the latent heat is released to the surrounding atmosphere. Around 5% of incoming solar energy leaves the surface through convection, by air in direct contact with the surface heated by the sun.

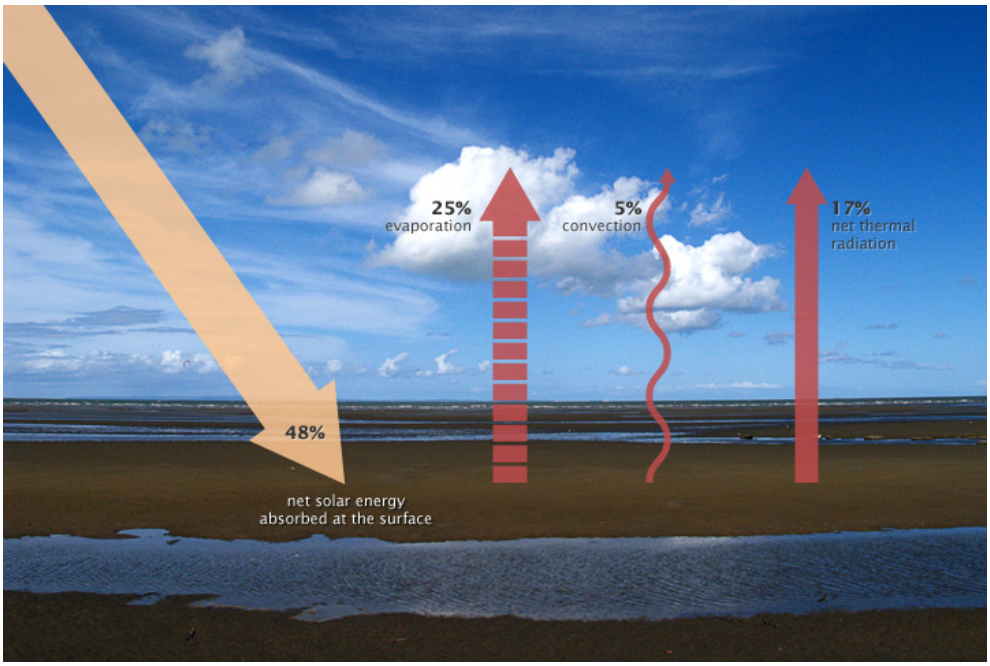

Figure 1.2: Representation of the Earth's surface energy emission. NASA illustration by Robert Simmon. Taken from [13].

1.2.2 Greenhouse Effect

As occurs on the Earth's surface, the energy flow into the atmosphere must be balanced, out of the top of the atmosphere. The gases with the highest concentration in the atmosphere (oxygen and nitrogen) are transparent to incoming sunlight (typically for higher wavelengths, i.e. above 150 nm) and to outgoing thermal infrared. However, some molecules are stronger infrared absorbers than others, as water vapour, carbon dioxide, methane, and other trace gases. Such molecules with high potential for absorbing infrared radiation are

known as *greenhouse gases*. The transmittance of the Earth's atmosphere in the infrared region and the main molecular absorption bands are shown in Figure 1.3. In some regions of the spectrum, the transmittance may be about 60% – 90%, but in others most of the radiation is absorbed, due to the presence of infrared active bands of atmospheric molecules such as O_3, CO_2 and H_2O.

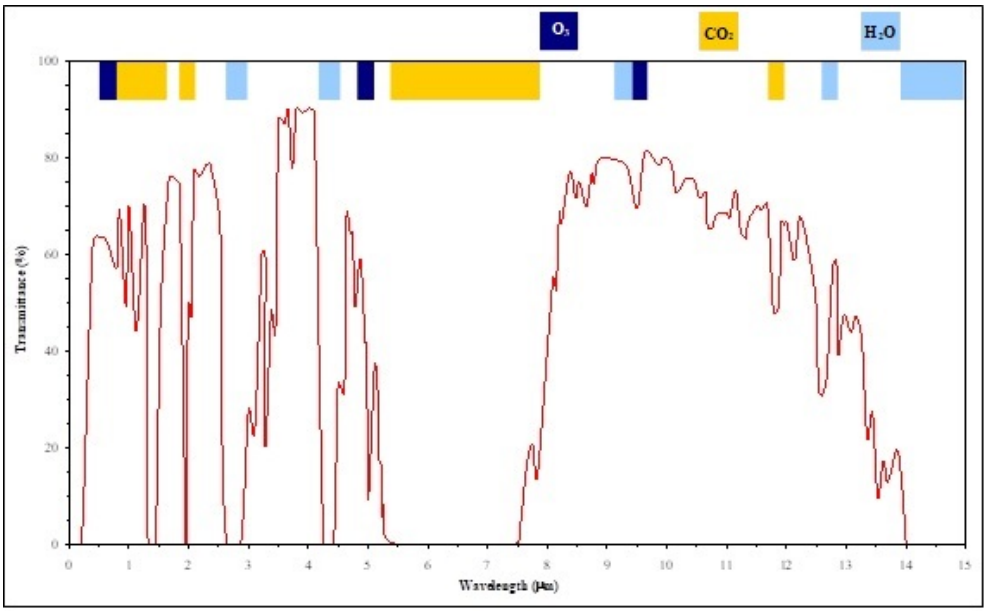

Figure 1.3: Transmittance of the Earth's atmosphere in the infrared region and the main molecular absorption bands. Taken from [12].

Of the infrared irradiated from the Earth's surface, only 12% of incoming solar energy escapes directly through the top of the atmosphere, the remaining 5% is absorbed by greenhouse gas molecules present in the atmosphere, as shown in Fig. 1.4. When these molecules absorb thermal infrared energy, their temperature increases and they radiate thermal infrared energy back in all directions[2]. Heat radiated upward continues to encounter greenhouse gas molecules; those molecules absorb the heat, their temperature rises, and the amount of heat they radiate increases. Above 5 km from the surface, the concentration of greenhouse gases decreases considerably, so that the heat is irradiated out of the atmosphere, which represents about 59% of the incoming solar energy [12, 13].

Once the molecules in atmosphere radiate thermal infrared energy in all directions, some of it spreads downward and comes back into contact with the Earth's surface, where it is absorbed. This additional heating, that makes the temperature of the Earth's surface warmer than it would be if it were heated only by direct solar radiation, is the natural greenhouse effect. If the Earth did not have an atmosphere, the temperature at the surface of the planet would be about 30°C lower than it is currently. The natural greenhouse

[2]The amount of heat radiated is proportional to the fourth power of its temperature. If the temperature of the Earth rises, the planet rapidly emits an increasing amount of heat to space. This large increase in heat loss in response to a relatively smaller increase in temperature — referred to as radiative cooling — is the primary mechanism that prevents unrestrained heating on Earth.

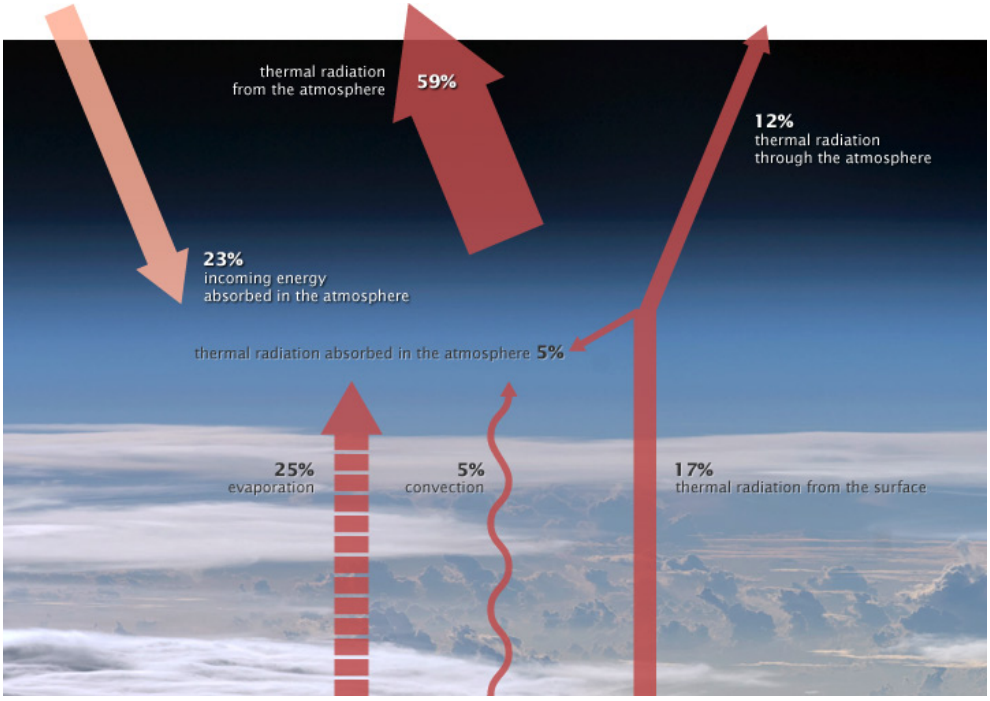

Figure 1.4: Representation of the Earth's atmosphere energy flux: About 23% of incoming sunlight is absorbed directly by the atmosphere. Of the thermal infrared energy from the surface, 12% passes through the atmosphere and escapes to space and around 5% is transferred to the atmosphere. NASA illustration by Robert Simmon. Taken from [13].

effect maintains the average temperature on the surface of the Earth at around 15 degrees Celsius.

The surface absorbs about 48% of the incoming solar radiation, while it only radiate heat equivalent to 12% of the incoming radiation out of the atmosphere. As for the particles in the atmosphere, they absorb about 23% of the radiation and emit out the equivalent to 59% of the incoming radiation. In other words, most solar heating happens at the surface, while most radiative cooling happens in the atmosphere. Although the retention of thermal energy by the greenhouse effect is a natural phenomena, the anthropogenic emissions are increasing at a very high rate, which leads to an increase in the average temperature of the planet.

The measure of the net energy change in the atmosphere is defined as radiative efficiency (RE), which is strongly related to the effectiveness of a greenhouse gas in changing the Earth's atmosphere budget, and can be used to assess and compare anthropogenic and natural drivers of climate change [16]. The radiative efficiency of a molecule is associated with the presence of infrared absorption bands in the region of the spectrum where the Earth's transmittance is high, particularly between 7.5 μm and 14 μm. That is because such molecules will absorb radiation at a wavelength that otherwise would be emitted out of the top of the atmosphere. This is the case of the halothane[3] molecule, which has peaks

[3]The transmittance spectra for isoflurane and sevoflurane molecules were not found in the literature, however, both show fairly high values for radiance efficiency and global warming potential (Table 1.2)

of infrared absorption between $7.5\mu m$ and $9\mu m$, shown in Figure 1.5. In fact, its radiative efficiency, of $0.13 W m^{-2} ppb^{-1}$, is very high, which becomes quite clear when compared to other relevant greenhouse gases, as we can see in table 1.2.

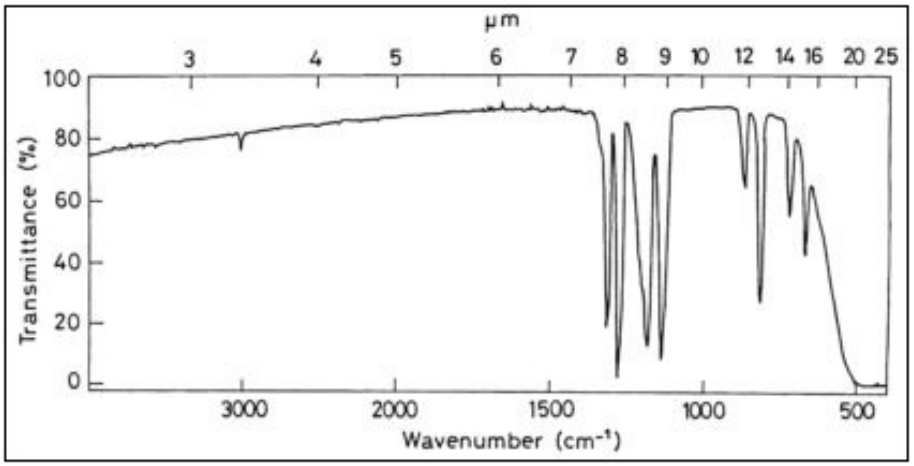

Figure 1.5: Transmittance of Halothane molecule, from [17].

The RE allows to obtain global warming potential (GWP), which is a measure of how much heat the emissions of 1 ton of a gas will trap in atmosphere over a given period of time, relative to the emissions of 1 ton of carbon dioxide (CO_2), given by [16]:

$$GWP_{gas} = \frac{RE_{gas}}{RE_{CO_2}} \frac{\tau_{gas}(1 - e^{-t/\tau_{gas}})}{\tau_{CO_2}(1 - e^{-t/\tau_{CO_2}})}, \tag{1.1}$$

where τ is the atmospheric lifetime of the compound, and t is the time horizon, usually of 100 years. It is clear in equation 1.1 that the two most important characteristics of a greenhouse compound are how efficiently it absorbs energy and how long it remains in atmosphere. In addition to being a determining factor in the determination of the GWP, the atmospheric lifetime plays a further role in the RE, since the heterogeneity in the distribution of the molecules in the atmosphere depends on its residence time. For molecules with lifetimes of less than a few months, the atmospheric distribution is dependent on where and when the gases are emitted, and the global average may not reflect the local atmospheric lifetimes. The atmospheric lifetime of the volatile anaesthetics will be discussed further in section 1.2.3.

The values for the global warming potential and radiative efficiency of the volatile anaesthetics and others molecules of notorious environmental interest are presented in table 1.2. Although all greenhouse gases shown in the table are present in very small atmospheric concentrations, collectively, these gases can have an appreciable influence on radiative efficiency, which leads to a substantial contribution to the global radiation budget. Since the beginning of the industrial revolution, atmospheric concentrations of carbon dioxide have increased nearly 30%, methane concentrations have more than doubled,

obtained from frequency calculations.

	Chemical formula	RE ($Wm^{-2}ppb^{-1}$)	GWP (100 years)
Halothane	$C_2HBrClF_3$	0.13^{ae}	41^{a}
Sevoflurane	$C_4H_3F_7O$	0.35^{b}	210^{b}
Isoflurane	$C_3H_2ClF_5O$	0.45^{b}	510^{be}
Methane	CH_4	$3.7 \cdot 10^{-4cd}$	25^{cd}
Carbon dioxide	CO_2	$1.4 \cdot 10^{-5cd}$	1^{cd}
Nitrous oxide	N_2O	$3.3 \cdot 10^{-3cd}$	298^{cd}
CFC-11	CCl_3F	0.26^{a}	4660^{a}

Table 1.2: Properties of the volatile halogenated anaesthetics and main greenhouse gases. Global warming potentials (GWP) are based on a 100 year time scale, and radiative efficiency (RE) is expressed in parts per billion (ppb).
[a] Hodnebrog *et. al.* [16].
[b] Andersen *et. al.* [11].
[c] IPCC Fourth Assessment Report: Climate Change 2007 [18].
[d] Cherubini *et. al* [19].
[e] Vollmer et. al. [2].

and nitrous oxide concentrations have risen by about 15%. These increases have enhanced the heat-trapping capability of the Earth's atmosphere [12]. As for the volatile anaesthetics, it is speculated that they were barely found in the atmosphere before the 1950s[4], when their industrial and clinical usage begun. However, recent studies show that there is a significant concentration of these molecules in the Earth's atmosphere (Table 1.3).

	Clinical introduction	Abundance (ppb)	Emission ($t\,yr^{-1}$)
Halothane	1956	9.2	250
Isoflurane	1981	97	880
Sevoflurane	1993	130	1200

Table 1.3: Abundance and emission of volatile anaesthetics in the atmosphere, expressed as dry air mole fractions in parts per billion (10^{-9}), from [2].

The global emission of halothane has been declining, from $490t\ yr^{-1}$ in 2000 to $250\,t\,yr^{-1}$ in 2014. In contrast, over the same period, isoflurane doubled its emission, from $440\,t\,yr^{-1}$ to $880\,t\,yr^{-1}$, while for sevoflurane, the earliest emissions data are from 2004, of $1100\,t$, which rose to $1200\,t\,yr^{-1}$ in 2014 [2].

1.2.3 The Ozone Layer

As mentioned before, most of the ozone present in the Earth's atmosphere is concentrated in the lower portion of the stratosphere. Ozone is a minor constituent of the Earth's atmosphere, composing only 0.2% of the atmospheric mass. However, located at an

[4] There is no data about the abundance of those molecules in the atmosphere before their clinical use.

altitude above 20 km, where the gases are rarefied, the ozone layer extends for about 10km.

Also known as ozone shield, this region of the Earth's stratosphere absorbs most of the sun's UV radiation between $210-300nm$, as can be observed in the absorption spectrum of ozone, in Figure 1.6. The absorption of radiation at high altitudes, prevents it reaching the surface of the planet, acting as a shield, and this is essential for life on Earth [20–23]. At low dosage, UV radiation is beneficial to human beings, while at high dosage it can be very dangerous and has harmful effects. The high exposure to UV radiation has some immediate health effects, such as damages in the epithelial cells [24, 25], alteration of the DNA [26–28] and releases organic substances that promote inflammation and dilation of the blood vessels [29, 30]. In the long term, UV radiation high exposure can induce degenerative changes in cells, fibrous tissues and blood vessels, cause inflammatory reactions in the eyes [31], with chronic effects such as cancer and cataracts [32], and lead to premature aging of the skin [33], melanoma and non-melanoma skin cancer [34–36].

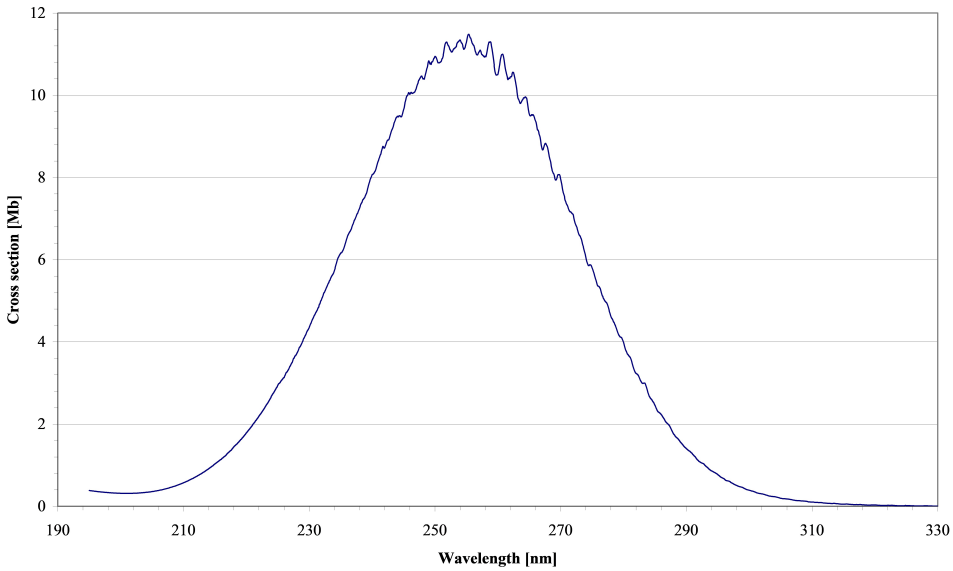

Figure 1.6: Absorption spectrum of ozone in the wavelength region 190-330nm, from [12].

The ozone molecule is a triatomic allotrope of oxygen, much less stable than the diatomic O_2, constantly formed and destroyed in the stratosphere by natural photolysis. Photolysis or photo-dissociation is a chemical process in which the absorption of electromagnetic radiation results in the breaking of chemical bonds of a molecule, i.e., dissociation. When sunlight UV radiation bellow $240nm$ [20, 37] is absorbed by oxygen molecules, it may excite the O_2 molecule, initially in a triplet ground state $(^3\Sigma_u^-)$. This excitation can lead to the dissociation into two oxygen atoms, one in the ground triplet state $O(^3P)$ and one in a metastable excited state $O(^1D)$ [12]:

$$O_2(^3\Sigma_u^-) + h\nu \rightarrow O_2(^3\Sigma_g^-) \rightarrow O(^3P) + O(^1P). \tag{1.2}$$

Atomic oxygen, which is very unstable, reacts with O_2 to form O_3, as shown in Figure 1.7. This process occurs in the presence of a third element (M), an atom or molecule, capable of absorbing the energy released by the exothermic reaction:

$$O + O_2 + M \rightarrow O_3 + M, \tag{1.3}$$

The same figure also shows a second process in the "ozone-oxygen cycle", when UV radiation of $240 - 315nm$ is absorbed by ozone, which is then excited and may be dissociated into a O_2 molecule and an oxygen atom. Usually this atomic oxygen quickly reacts with another oxygen atom to form O_2, or with an oxygen molecule to form another ozone molecule. Other pathway for the ozone destruction is the reaction between two O_3 molecules, forming three molecules of O_2 [12, 20–23].

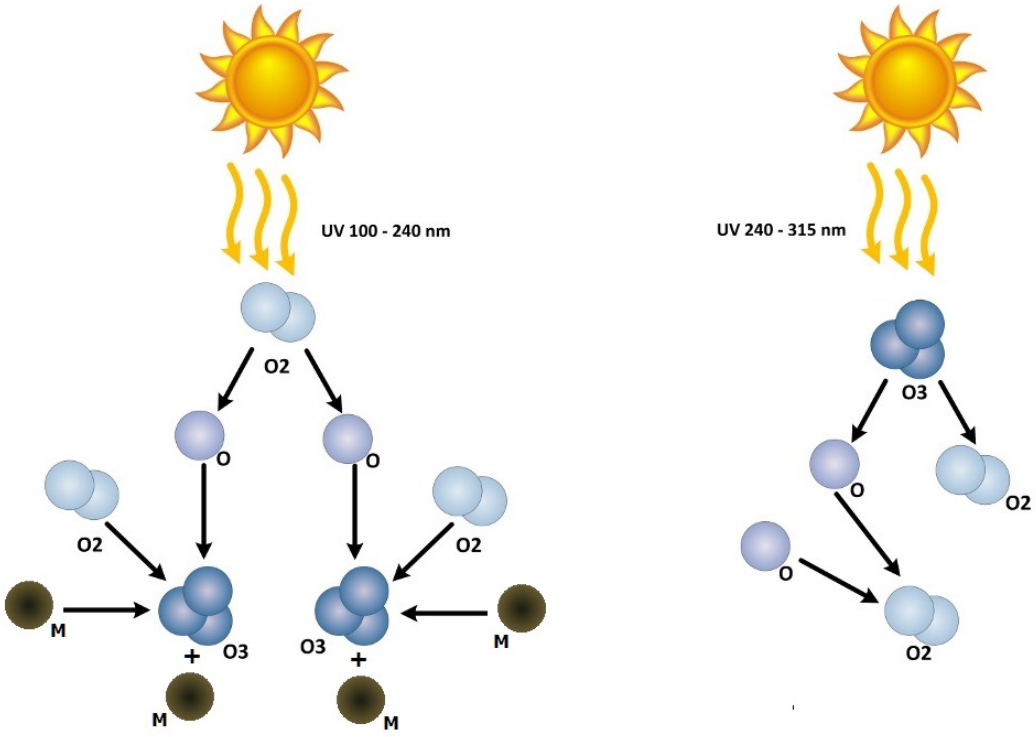

Figure 1.7: Representation of the ozone molecule formation (left) and destruction (right). Adapted from [38].

Over the Earth's lifetime, the ozone concentration in the atmosphere has maintained a dynamic balance, through the cyclical mechanism of formation and destruction. However, in the early 1970's, the scientific community found evidence that anthropogenic emission of gases was disrupting this balance, resulting in depletion of the ozone layer. The monitoring of the ozone layer began in 1956, when the British Antarctic Survey started the measurements using a Dobson spectrophotometer at the Halley Bay Observatory on Antarctica, with the related data shown in Figure 1.8 in red, leading to the first publication on depletion of the ozone layer, in 1985 [39].

Between 1980 and 1994, satellite data from the total ozone mapping spectrometer (TOMS), together with data from the Halley Bay Observatory, have shown that the deflection of the ozone layer increased dramatically, reaching concentrations below 200 Dobson[5] (Figure 1.8). The Ozone Monitoring Instrument (OMI), the latest generation technology in ozone monitoring, is flying on board NASA's Aura satellite since 2005, can distinguish between aerosol types, such as smoke, dust, and sulphates, which provides more accurate data [40].

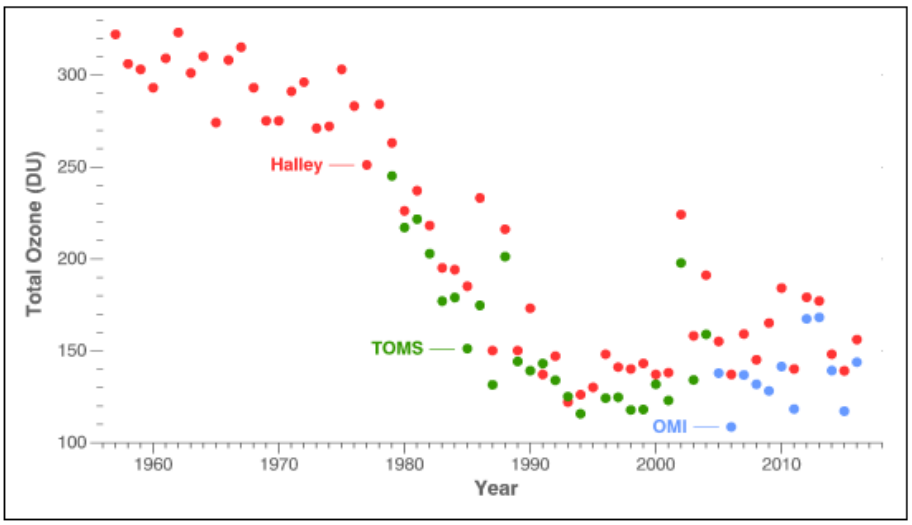

Figure 1.8: Concentration of ozone above Antarctica: data from the ground Dobson spectrophotometer at the Halley Bay Observatory in red, satellite data by the total ozone mapping spectrometer (TOMS) in green, and by the ozone monitoring instrument (OMI) in blue, from [40].

Earth's natural shield became drastically thin over the years, especially above the south pole. This large thin spot in the polar region has been termed the ozone hole. Several studies relate the cause of depletion in the ozone layer to atmospheric chemistry, particularly caused by the increased concentration of CFC gases [42–44] and halogenated compounds [45–50], among many others. Nowadays the relation between depletion of the ozone layer and the emission of these gases is very well established, despite some controversial opinions. The production of chlorofluorocarbons and halogenated compounds for industrial, commercial and medical purposes yielded a large increase in the presence of these in the stratosphere. Once exposed to UV radiation, these compounds may dissociate by photolysis, releasing atoms of chlorine, bromine, nitrogen, hydrogen and others. As the ozone molecule and atomic oxygen are both highly unstable, they easily react with these atoms. The reaction of such atoms with the first, represents an additional mechanism for destruction of the ozone molecule. While the reaction with the second results in fewer atomic oxygen available in the stratosphere, which means fewer ozone molecules

[5]Dobson is the unit commonly used for measuring the concentration of ozone. One Dobson is the amount of ozone required to create a $0.01mm$ layer of pure ozone at $1atm$ and $0°C$ and corresponds to $2.69 \cdot 10^{16}$ molecules of ozone for every square centimetre of area.

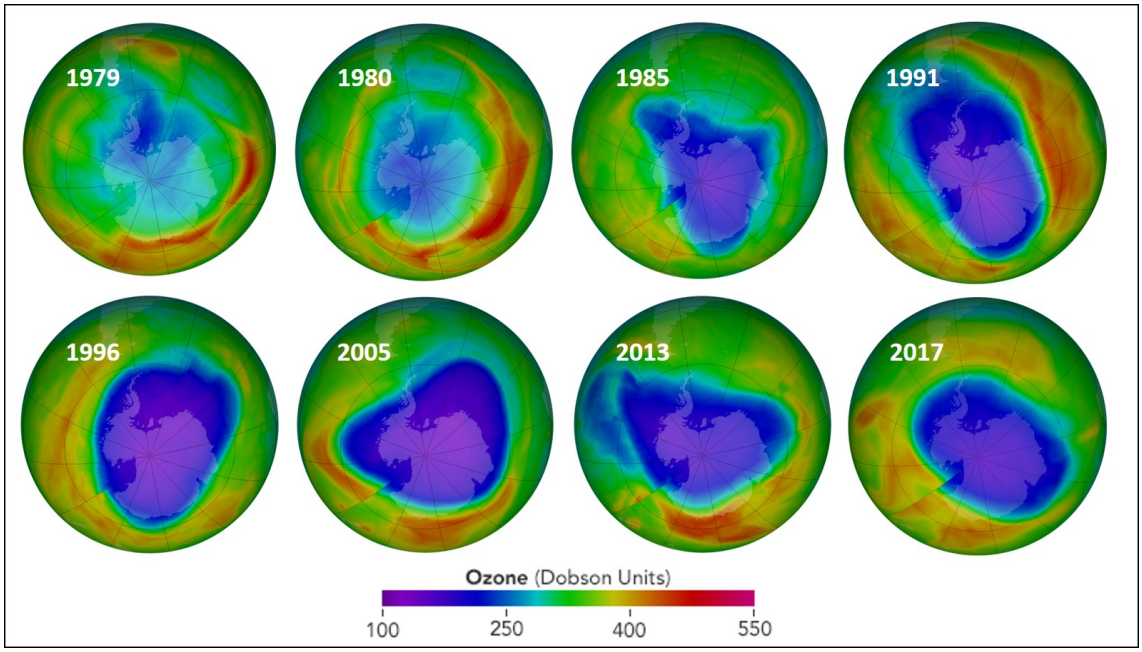

Figure 1.9: Monitoring the ozone hole over Antartica, from the ozone mapping spectrometer (TOMS) instrument, on the Nimbus satellite, between 1979 and 2003, and by the Royal Netherlands Meteorological Institute's ozone monitoring instrument (OMI) on NASA's Aura satellite from 2004 to present. Purple and dark blue areas are part of the ozone hole, adapted from [41].

being formed, since the efficiency of O_3 formation is sensitive to the presence of atomic oxygen. In other words, the anthropogenic emission of chlorofluorocarbons and halogenated compounds interferes in the dynamic balance of the "ozone-oxygen cycle", with ozone molecules being destroyed at a much higher rate than being created.

The ozone concentration has been monitored by several research institutes and environmental agencies in the past decades. It is estimated that about 80% of chlorine and bromine currently present in the stratosphere are a consequence of anthropogenic sources [41]. In the 1990's, a new lower ozone concentration fell below 100 Dobson units for the first time. Since then, concentrations below 100 Dobson have been commonly reported. The global recognition of the destructive potential of CFC emission led to the 1989 Montreal Protocol, banning the production of ozone-depleting chemicals. However, as mentioned before, some substances considered of essential use have remained uncontrolled, among them are the inhalable anaesthetics.

Most portion of the inhaled doses of anaesthetics will end up in the troposphere, but the amount of each species that will reach the stratosphere, and thereby potentially affect the ozone layer, is determined by its lifetime. It must be considered that the solar radiation that reaches the Earth's surface is limited to wavelengths grater than 292 nm (below 4.2 eV) and only photons with wavelengths grater than 180 nm (below 6.9 eV) are able to penetrate altitudes below 30km [51–53]. The lifetime of a trace gas in the troposphere depends mainly on its chemical reaction with the hydroxyl (OH) radical, which is the main

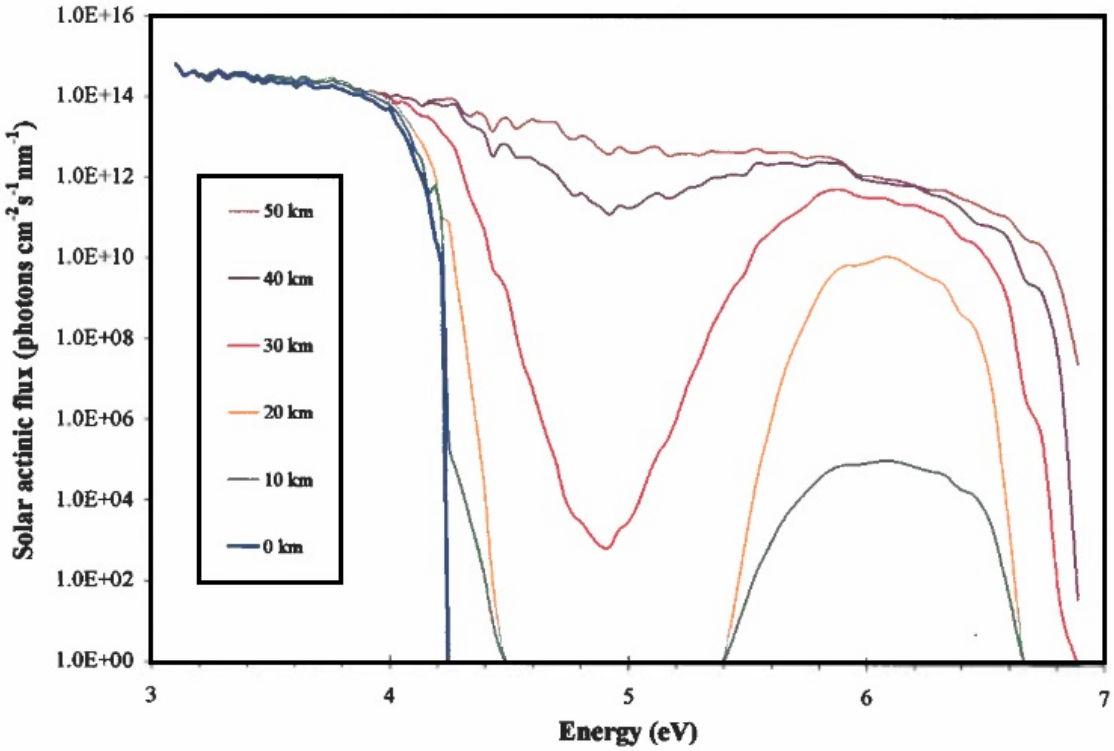

Figure 1.10: Energy profile of the solar actinic flux in atmosphere for several altitudes, from [51].

homogeneous sink for these species in the troposphere, while most significant stratospheric loss occurs due to photolysis. Thus, the total atmospheric lifetime of a compound (τ_{comp}) must consider both chemical and photochemical lifetimes.

$$\tau_{comp} = \left(\frac{1}{\tau_{OH}} + \frac{1}{\tau_{photo}} \right)^{-1} \tag{1.4}$$

The effectiveness of any anthropogenic compound in damaging the ozone layer is generally expressed by the ozone depletion potential (ODP), which is given relatively to a standard compound, the trichlorofluoromethane (CFC-11). The ODP will depend on de molecular weight of the species (M), its lifetime (τ) in the atmosphere, and is given by:

$$ODP = \frac{\tau_{comp}}{\tau_{CFC11}} \times \frac{M_{CFC11}}{M_{comp}} \times \frac{n_{Cl} + \alpha n_{Br}}{3} \tag{1.5}$$

where n_{Cl} and n_{Br} are, respectively, the number of Cl and Br atoms in the molecule of interest, and α is the relative effectiveness in destroying ozone in the stratosphere between these two atoms [6].

The CFC-11 compound, which is used as a reference, and thus its ODP is 1, has a very long lifetime in the troposphere, and therefore 100% of the emitted compound reaches the

[6] It is estimated that the efficiency of bromine to destroy ozone molecules in the stratosphere is between 35 and 80 times higher than that of chlorine [54], because of the significant differences of the α local value. The global average of the relative effectiveness α in the lower stratosphere is calculated by *Daniel et. al.* [55] as 50.

stratosphere as listed in Table 1.4. In 1985 it was estimated that CFC-11 was the source of about 22% of the total amount of chlorine present in the atmosphere [48]. However, CFC total emissions were reduced considerably since the Montreal Protocol, CFC-11 including, while the use of halogenated volatile anaesthetic, and consequently its emission into the atmosphere, has grown significantly in the last 50 years. Therefore, the effects of these anaesthetics on the ozone layer should be taken into account.

	Chemical formula	τ_{OH} (years)	τ_{photo} (years)	τ_{comp} (years)	ODP	Imput into stratosphere (%)
Halothane	$C_2HBrClF_3$	7.0	105	6.6	1.56	13.2
Sevoflurane	$C_4H_3F_7O$	4.0	-	4.0	0	12.6
Isoflurane	$C_3H_2ClF_5O$	5.9	3130	5.9	0.03	14.6
CFC-11	CCl_3F	-	50	50	1.00	100

Table 1.4: Tropospheric lifetime (τ_{OH}), stratospheric lifetime (τ_{photo}) up to 36 km, ODP value of the halogenated volatile anaesthetics, together with the percentage of each compound that does not degrade in the troposphere, and therefore, reaches the stratosphere. Calculated by Langbein *et. al.* [9].

Halothane is the inhaled anaesthetic most dangerous for the ozone layer, with a large ODP value of 1.56. Although its emission has been declining over the years, since many countries have ceased its prescription to patients, several underdeveloped countries still do it, in addition to its continuing use for veterinary purposes. Therefore, the concentration of halothane in the atmosphere, that was of 9.2 parts per billion in 2015 [2], should not be overlooked.

The isoflurane molecule has a lifetime in the stratosphere of 5.9 years, which amounts 12.6% of its total anthropogenic emissions reaching the stratosphere. Its ODP is 0.03 and may be considered small, but taking into account its significant abundance in the atmosphere, 97 parts per billion [2], the effects of isoflurane on depletion of the ozone layer can not be disregarded.

Sevoflurane molecule has no role in the depletion of the ozone layer, because it has no bromine or chlorine atoms in its composition, and therefore its ODP is zero. According to Daniel and co-workers [55], fluorine atoms "*have a negligible impact on ozone because of rapid conversion to tightly bound fluorine reservoir species*". Despite this, sevoflurane is one of the objects of this study due to its high environmental impact related to global warming.

In the literature, the data found for the stratospheric lifetimes, and ODP values of anaesthetics are considerably discrepant. These vary from 1.0 to 7.0 years for halothane, 0.6 to 2.2 years for sevoflurane and 2.0 to 3.2 for isoflurane [2, 11, 16, 54]. In most cases, the studies consider in their calculations the OH concentration at ground level, making the lifetime value to be underestimated. In the data from Langbein and co-workers [9], presented in Table 1.4, the tropospheric lifetime was calculated from the experimental OH rate coefficients considering the variation of the OH concentration with altitude.

1.3 Summary

In the present work, VUV photoabsorption spectra have been measured for the anaesthetics between 5.6 to 10.8 eV (220-115 nm). Quantum chemical calculation were performed to determine the excitation energies of the neutral molecules in order to complement electronic state spectroscopy studies, low-lying excited singlet valence and Rydberg states are investigated and assigned. The Rydberg series converging to the ionisation energy limits are identified according to the magnitude of the quantum defects. The measured absolute cross-sections have been used to calculate the photolysis lifetimes of the molecules in the Earth's atmosphere.

For a complete spectroscopic investigation of the subject molecules, we also performed a experimental study on the elastic differential cross section (DCS) and integral cross section (ICS) for electron interactions with the anaesthetics in the energy range from 7 to 50 eV. The measurements were complemented with calculations of DCS and ICS performed by collaborating groups, obtained using two different theoretical methodologies.

Energetic electrons in the upper atmosphere can yield ionization and secondary electron processes, where the latter may trigger elastic and inelastic scattering within the medium. In such elastic scattering processes, the collision dynamics can be probed through wild range of angular distribution. As so, differential elastic scattering measurements also represent a key step to determine the role of the electronic structure. Furthermore, the inelastic processes related to energy loss, give information on the chemical nature of those molecular compounds. Such electron energy loss spectra can give a more complete characterization of the electronic state of the studied molecules, including information about the transitions to triplet states.

Low-energy to intermediate electron-impact DCSs are obtained using two different but complementary theoretical methodologies, the Schwinger multichannel method implemented with pseudopotentials (SMCPP) and the independent atom model–screening corrected additivity rule plus interference (IAM-SCAR+I). This methodology together with experimental data has recently proven to provide an accurate description of the electron scattering processes in different molecular targets

This thesis has been organized in seven chapters, where in chapter two we present the basic concepts of molecular theory used in this work. Chapter three presents in detail the experimental procedures and calculation methods used. In chapters four and five, are presented the results obtained concerning the characterization of electronic states by synchrotron radiation and concerning electron-molecule collision, respectively, for the anaesthetics. Chapter six show the characterization of electronic states by synchrotron radiation of Methanol, being a well-known and widely studied molecule of environmental interest, has the purpose of a prototype molecule for comparison. Chapter seven brings the final considerations about this work, and presents suggestions for future works.

Chapter

2 Molecular Theory

Not explaining science seems to me perverse. When you're in love, you want to tell the world. My lifelong love affair with science

— Carl Sagan, The Demon-Haunted World: Science as a Candle in the Dark

This chapter describes the main concepts of electron-molecule and photon-molecule interactions. It begins with general considerations about molecular electronic structure, electronic transitions and the description of the molecular target. Section 2.2 is dedicated to electron collisions with molecules, which comprises the electron scattering theory; and section 2.3 is devoted to photoabsorption, in which photo-molecule interactions and generalized oscillator strengths are considered.

2.1 Molecular Structure and Interactions

2.1.1 Target Description

When dealing with molecular interaction, whether this is with radiation or with a particle, it is necessary first to consider, besides the interaction itself, the description of the target molecule.

For this purpose, the molecule is described as a problem of N electrons with M nuclei, using the *Born-Oppenheimer* fixed nuclei approximation, which considers the decoupling between the electronic and the nuclear parts of the molecule. Therefore, the Hamiltonian of the target is

$$\mathcal{H}_e = -\sum_{i=1}^{N} \frac{1}{2}\nabla_i^2 - \sum_{i=1}^{N}\sum_{A=1}^{M} \frac{Z_A}{r_{iA}} + \sum_{i=1}^{N}\sum_{j>i}^{N} \frac{1}{r_{ij}}, \tag{2.1}$$

in atomic units[1], were the first term is related to the kinetic energy of the electrons, the second is related to the Coulomb interaction between the electrons and the nuclei and the third the repulsion between electrons [56, 57].

In most cases, obtaining the exact numerical solution for the many electron system is computationally impracticable. For this reason an approximation method is required. The *Hartree-Fock* approximation [58, 59] is a variational method used to obtain the wave function of the fundamental electronic state of the molecule, and its formalism is described in appendix A. It is the most used approximation method in quantum chemistry for this purpose, and it was used in the calculations presented in this work. This method uses a single *Slater* determinant to describe the electronic wave function ψ which, considering a closed-shell target, can be written as:

$$\psi = \frac{1}{\sqrt{N!}} \sum_{i=1}^{N/2} (-1)^{p_i} \mathcal{P}_i \{\chi_1(\vec{r}_1,\omega_1), \chi_2(\vec{r}_2,\omega_2), \cdots, \chi_N(\vec{r}_N,\omega_N)\}, \tag{2.2}$$

where $\mathcal{P}_i$ is the operator responsible for the *i-th* permutation of $\vec{r}_i$ and p_i, which can be written in the form of a determinant. The *Slater* determinant is given in terms of the spin-orbitals $\chi_i(\vec{r},\omega)$, were $\vec{r}$ is the position and ω is the spin state. Spin-orbital is a wave function that describes each electron of the molecule, given by

$$\chi(\vec{r},\omega) = \varphi(\vec{r})\alpha(\omega) \; ou \; \chi(\vec{r},\omega) = \varphi(\vec{r})\beta(\omega) \tag{2.3}$$

where φ depends only on the spatial coordinates of an electron, known as the molecular orbitals, α and β represent the up and down spins, respectively.

Molecular orbitals are described through a set of base functions $\{\phi_\mu\}$, which are the expansion of molecular orbitals in terms of k atomic orbitals:

$$\varphi_i = \sum_{\mu=1}^{k} C_{\mu i}\phi_\mu. \tag{2.4}$$

The wave function of the ground state of the target molecule, the eigenstate $|\psi\rangle$, is described as a set of base functions in the form of *Cartesian Gaussian* functions[2] [61] that describes the molecular orbitals, and are defined as

$$\phi(x,y,z) = N_{\ell mn}(x-x_0)^\ell (y-y_0)^m (z-z_0)^n e^{-\alpha|\vec{r}-\vec{r_0}|^2}, \tag{2.5}$$

[1] The calculations in molecular physics are usually expressed in terms of atomic units, where the Planck's constant, the mass and charge of electrons are equal to 1 ($\hbar = m_e = e = 1$). The atomic unit of length is the Bohr radius, given by $\frac{h^2}{m_e e^2} \equiv 1$ bohr , and the atomic unit of energy is expressed by $E_h = \frac{e^2}{a_0} \equiv 1$ hartree. Unit conversion is made by the relation $1a_0 = 0.529$Å and 1 hartree $= 27.211eV$.

[2] Cartesian Gaussian functions are use for the expansion of the scattering wave function in order to be applicable to polyatomic molecular targets with arbitrary geometries. The square integrable (L2 type) feature in this type of function allows to put all exit channels in a Green's function, which is presented in section 3.4.1. The strategy is based on the fact that 2-electron integrals involving 4 Cartesian Gaussian functions or one-plane wave and 3 Cartesian Gaussian functions could be evaluated analytically As a result the variational method would be transformed in simple matrix multiplications involving these integrals [60, 61].

where $N_{\ell mn}$ is the constant of normalization, $\vec{r} = (x, y, z)$ is the position, $\vec{r}_0 = (x_0, y_0, z_0)$ is the position were the wave function is centred, α is the Gaussian exponent, and ℓ, m and n are whole numbers.

The *Hartree-Fock* calculations used in the target description (and also the scattering calculations later) depend, in terms of processing time, on the set of basis functions used to describe the atomic orbitals of the target molecule. The more electrons need to be described, the bigger the set of basis functions should be, and consequently, the longer the processing time.

2.1.2 Molecular Electronic Transitions

Electrons occupy the orbitals in a molecule according to its internal energy, the configuration that corresponds to the lowest electronic energy is known as the ground state. The absorption of energy by molecules may lead to electronic transitions, which involve changes in the distribution of electrons over the molecule, and the electron is excited to an upper orbital. Such process is usually described as *vertical transition*, meaning that the molecular geometry is preserved, and known as the *Frank-Condon principle* [62, 63]. There are two types of excited electronic states: valence and Rydberg states. There is also the possibility of a mixed character excited state, combining both valence and Rydberg states. Two types of mixed character may occur in electronic transitions and excited states: delocalization of the frontier orbitals involved in electronic transitions (i.e. the valence/Rydberg states) and the combination of more than one one-electron excitations in an electronic transition [64].

Valence transition is the promotion of a single electron from an occupied orbital into an unoccupied orbital of the valence shell. Valence states are described in terms of σ, π, (bonding) σ^*, π^* (anti-bonding) and n (non-bonding) orbitals. In general, electrons in the σ orbitals are more strongly bound to the nuclei than the π bond and n electrons, thus requiring more energy to be excited.

A Rydberg transition is the excitation of one electron into orbitals corresponding to higher energy levels (higher principal quantum number) than the valence orbitals. Rydberg states can be seen as an electron in an orbital with a large radius, distant from the core, resembling a *hydrogen-like* molecule. Because of their large size, typical Rydberg orbital are non-bonding rather than bonding or anti-bonding [65].

Rydberg states occur in series whose energy obey the Rydberg formula [65–68]:

$$E_n = IE - \frac{R}{(n-\delta)^2} \tag{2.6}$$

where IE is the ionization energy towards which the series converges, R is the Rydberg constant (13.606 eV), δ is the quantum defect and n is the principal quantum number. The quantum defect δ expresses the deviation from the *hydrogen-like* behaviour, and it is helpful in the assignment of the Rydberg state. Considering atomic species belonging to the second row of the periodic table, states for which $0.7 \leq \delta \leq 1.1$ are labelled $''s''$,

those with $0.3 \leq \delta \leq 0.7$ are *"p"* states and those with $0 \leq \delta \leq 0.3$ are *"d"* states [62, 63, 65]. From the experimental point of view, Rydberg states appear generally in electronic excitation spectra as sharp and intense peaks, in contrast with valence states, that show up as a large and diffuse structure.

2.1.3 Vibrational Excitation

Vibrational spectroscopy is related to the motion of nuclei to each other within the molecule, where the equilibrium positions of vibrations are determined by the balance of repulsive forces between positively charged nuclei, the repulsive forces of the electrons surrounding each nucleus, and the attractive forces between the nucleus and the electrons throughout the part of the molecule.

When all these forces are balanced in order to obtain a minimum state of energy, the inter-nuclear equilibrium distances are defined as bonding lengths. For a molecule containing N nuclei, their positions and motions can be described by 3N coordinate values. The number of vibrational modes is given by 3N-6 (or 3N-5 for linear molecules), since nuclear rotations and translations do not affect the vibration motion [62, 69, 70]. As a consequence, each vibrational mode can be treated as a harmonic oscillator approximation, and the total vibrational energy of the molecule is given by the sum of all its n vibrational modes, with ν_j frequency:

$$E_{vib} = \sum_{j=1}^{n} h\nu_j \left(v_j + \frac{1}{2} \right), \tag{2.7}$$

where $v_j = 0, 1, 2, 3 \ldots$

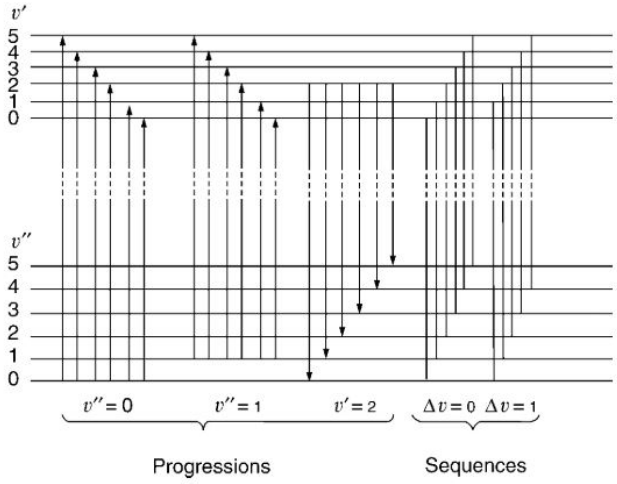

Figure 2.1: Vibrational progressions and sequences in the electronic spectrum of a diatomic molecule, from [71].

At low temperatures, the molecules start out in the $v = 0$ vibrational level, which is the ground vibrational state, and have energy equal to $1/2h\nu_j$. When the molecule absorbs a quantum of energy, a vibrational transition from $v = 0$ to $v = 1$ is induced, this is refereed

to as fundamental vibrational transition. Transitions from the ground vibrational state to a $v > 1$ state are termed overtone. At room temperature, the ground state molecules may have different amounts of vibrational energy, some will be unexcited, while others may have one or more quanta of vibrational energy. The number of vibrationally excited molecules on the ground state increases exponentially with temperature, and the relative concentration of molecules with two distinct vibrational energies, i.e. the relative population of molecular occupancy between two vibrational species[3] is estimated based in the Maxwell-Boltzmann distribution [72–76]. The relative population ratio (n_j/n_i) between the species j and i, with respectively energies ϵ_j and ϵ_i, is given by the Boltzmann's factor:

$$\frac{n_j}{n_i} = \frac{e^{-\epsilon_j/kT}}{e^{-\epsilon_i/kT}} = e^{-\Delta\epsilon/kT}, \tag{2.8}$$

where k is the Boltzmann constant and T is temperature.

An electronic transition accompanying by one of more sets of vibrational bands are referred to as vibronic transitions, which in turn can be classified as progressions or sequences bands. A group of transitions with common lower or upper level is referred to as progression, while a sequence involves a series of vibrational transitions with the same value of Δv [71, 77], as Figure 2.1 shows. It is important to notice that the Boltzmann factor is a dominant factor of such sequence bands, and its members are generally closely spaced. Long sequences are observed mostly in emissions, due to the population requirements.

2.2 Collision Theory - Electron Scattering

To describe the process of electron scattering by a target, let us consider an incident electron (e^-) with well defined energy and initial wave vector $\vec{k}_i$ that collides with a fixed target (AB) in the laboratory reference, where the incidence direction is along the z-axis $(\vec{k}_i = k_i\hat{z})$, and is scattered with final vector wave $\vec{k}_f$. The scattered electrons are then measured by a detector outside the region of influence of the interaction potential. The detector records the angle at which the particles were scattered after the collision [56].

Several processes may occur during a collision, which are known as scattering channels. The scattering channels are classified as either elastic or inelastic. They are termed elastic scattering when the kinetic energy of the incident electron is conserved, i.e. there is no transfer of energy between the incident electron and the target during the collision, with the exception of rotational excitation. Inelastic scattering occurs when the electron transfers some kinetic energy to the target. In this case, many different channels are possible, such as excitation and/or ionization of the target[4].

[3] It is convenient to think of all the molecules that have the same vibrational energy as a "chemical" species, with the purpose of simplifying its description.

[4] The * represents the excited state of an atom or molecule.

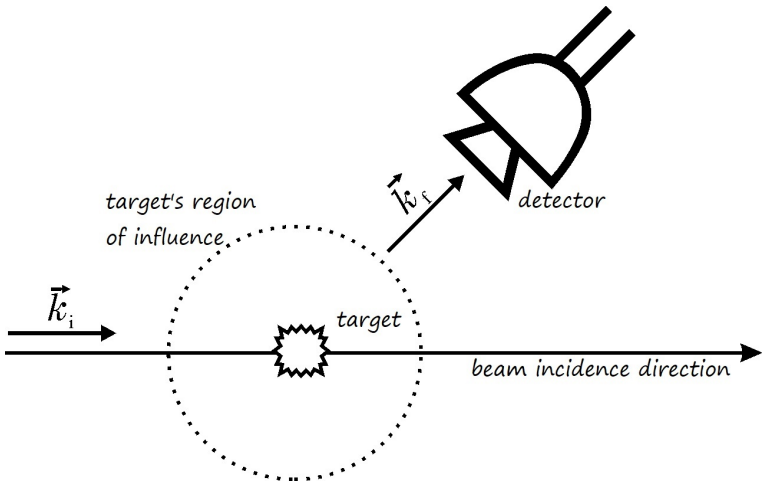

Figure 2.2: Representation of the collision process, were an electron with $\vec{k}_i$ initial momentum interacts with a target, and is scattered with $\vec{k}_f$ final momentum, adapted from [56].

$$AB + e^- \longrightarrow AB + e^- \qquad \text{Elastic scattering}$$
$$AB + e^- \longrightarrow AB^* + e^- \qquad \text{Electronic excitation}$$
$$AB + e^- \longrightarrow AB^+ + 2e^- \qquad \text{Ionization}$$

The collision process is described as fast when the velocity of the incoming electron is large compared to that of the target electrons, in this case the incident electron act as a perturbation on the target. In the cases were the velocity of the incident electron is close to that of the target, the incoming electron can be coupled to the target, forming a temporary negative ion, which later may induce fragmentation of the target molecule, though dissociative electron attachment, or the detachment of the electron from the molecule, known as auto-detachment.

$$AB + e^- \longrightarrow \left[AB^-\right]^* \longrightarrow AB^* + e^- \qquad \text{Auto-detachment}$$
$$AB + e^- \longrightarrow \left[AB^-\right] \longrightarrow A^- + B^* \qquad \text{Fragmentation}$$

A channel is said to be *open* if the process is allowed by the energy conservation laws, otherwise it is a *closed* channel.

2.2.1 Stationary Wave-Function for Scattering

The stationary eigenstates of the incident particle are obtained by solving the time-independent Schrödinger equation,

$$\mathcal{H}|\Psi(\vec{r})\rangle = \mathcal{E}|\Psi(\vec{r})\rangle, \tag{2.9}$$

were $|\Psi(\vec{r})\rangle$ is the eigenstate of the scattered particle, with energy $\mathcal{E}$, representing the total energy of the collision. $\mathcal{H}$ is the Hamiltonian of the free particle, which interacts with a potential V, and is expressed as:

$$\mathcal{H} = \frac{p^2}{2m} + V. \tag{2.10}$$

The solution for the Schrödinger equation, in the coordinate system described in Figure 2.3 in a region out of the potential range (asymptotic behaviour), is a superposition of a plane wave (e^{ikz}) which propagates along the direction of incidence and a spherical wave(e^{ikr}/r) modulated by the scattering amplitude $f(k,\theta,\phi)$ that depends on the angles θ and ϕ, and the wave vector module k, with a normalization constant N,

$$\Psi(\vec{r}) \underset{r\to\infty}{\longrightarrow} N\left[e^{ikz} + f(k,\theta,\phi)\frac{e^{ikr}}{r}\right]. \tag{2.11}$$

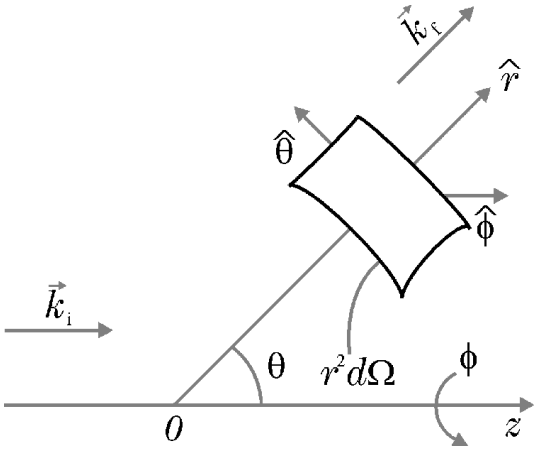

Figure 2.3: Representation of the coordinate system in the laboratory's frame, where the incident wave with momentum $\vec{k}_i$ in z direction focuses on the target, and is scattered with a final momentum $\vec{k}_f$. θ is the scattering angle and $r^2 d\Omega$ is the solid angle. From [56].

2.2.2 Scattering Cross Section

The analyses of the collision phenomena are expressed quantitatively in terms of the *cross section*, which is the probability of a certain process (channel) to occur. The DCS is obtained using the scattering amplitude $f(k,\theta,\phi)$ [56, 70, 78],

$$\frac{d\sigma}{d\Omega} = |f(k,\theta,\phi)|^2. \tag{2.12}$$

For the ICS, the integration over the solid angle is performed, considering all the possible orientations for the scattering.

$$\sigma = \int |f(k,\theta,\phi)|^2 d\Omega \ . \tag{2.13}$$

The cross section is defined by Bransden and Joachain [70] as:

> *"The cross-section for a certain type of event in a given collision as the ratio of the the number of events of this type per unit of time, per unit scattered, to the flux of the incident particles with respect to the target".*

In other words, considering the scattering process described in the beginning of this section in a classical point of view, the cross section σ is the constant of proportionality between the number of scattered electrons N^{sc} and the number of incoming electrons N^{inc}, along with an element of volume $\Delta\Omega$.

$$N^{sc}(\Delta\Omega) = \sigma(\Delta\Omega) N^{inc}. \tag{2.14}$$

The cross section $\sigma(\Delta\Omega)$ represents the part of the area in the target that scatters into $\Delta\Omega$, and is expressed in units of area [5]. For an elemental solid angle $d\Omega$, the cross section $\sigma(\Delta\Omega)$, where $d\Omega = sin\theta d\theta d\phi$, the quantity $d\sigma/d\Omega$ is the DCS and gives the probability of a given scattering channel in terms of the angles at which the particle is scattered. The ICS gives the probability of a scattering channel in all possible directions, and can be obtained through DCS integration.

2.2.3 Method of Partial Waves

The scattering amplitude contains the information concerning the scattering process, and one way of obtaining it is through the method of partial waves [70, 78, 79]. The simplest scenario for describing the method of partial waves is the scattering of a low-energy particle by a central potential. The stationary eigenstates are obtained by solving the time-independent Schrödinger equation, as described in section 2.2.1, whereas, the potential energy of the free particle Hamiltonian (equation 2.10) depends only on the distance r from the origin of the system, $V = V(r)$.

In this case, the scattering wave function Ψ, which is the solution of the Schrödinger's equation, can be expressed through a expansion in partial waves, with a radial part $R_\ell(k,r)$ and an angular part, given by spherical harmonics $Y_\ell^m(\theta,\phi)$, such as

$$\Psi(k,\vec{r}) = \sum_{\ell=0}^{\infty} \sum_{m=-\ell}^{+\ell} C_{\ell m}(k) R_\ell(k,r) Y_\ell^m(\theta,\phi), \tag{2.15}$$

where ℓ and m correspond to the quantum numbers of angular momentum and magnetic moment, respectively, and $C_{\ell m}(k)$ are the expansion coefficients. Thus, the Schrödinger equation can be written as

$$\left[\frac{d^2}{dr^2} + k^2 - \frac{\ell(\ell+1)}{r^2} - U(r)\right] r R_\ell(k,r) = 0, \tag{2.16}$$

where $k = (2mE)^{1/2}/\hbar$ is the system's energy, with $E = p^2/(2m)$, $\ell(\ell+1)/r^2$ is the centrifugal potential barrier of the incident particle associated with an angular momentum ℓ, and $U = 2mV/\hbar^2$ is the reduced potential of the target.

Applying the conditions for the asymptotic behaviour in the scattering wave function, given by equation 2.11, one obtain the scattering amplitude expressed in partial waves:

$$f(\theta) = \frac{1}{k} \sum_{\ell=0}^{\infty} (2\ell+1) e^{i\delta_\ell} \sin\delta_\ell P_\ell(\cos\theta), \tag{2.17}$$

[5] The cross sections are commonly expressed in Mbarn. $1barn = 10^{-28} m^2$

were δ_ℓ is the phase shift [56, 70, 78] and $P_\ell(\cos\theta)$ are Legendre's polynomials. The phase shift can be found using the expression [56, 70, 78],

$$\tan\delta_\ell = -k\int_0^\infty \jmath_\ell(k,r)U(r)R_\ell(k,r)r^2dr, \tag{2.18}$$

where $\jmath_\ell(k,r)$ is the spherical Bessel function, $U(r)$ is the reduced potential, and $R_\ell(k,r)$ is the radial function.

Thereupon, equations 2.12 and 2.13 are obtained and the integral cross section as a function of partial waves is given by:

$$\sigma \equiv \int d\Omega \frac{d\sigma}{d\Omega} = \frac{4\pi}{k^2}\sum_{\ell=0}^{\infty}(2\ell+1)\sin^2\delta_\ell(k) = \sum_{\ell=0}^{\infty}\sigma_\ell, \tag{2.19}$$

were

$$\sigma_\ell = \frac{4\pi}{k^2}(2\ell+1)\sin^2\delta_\ell, \tag{2.20}$$

is the contribution of each partial wave for the integral cross section. Thus it is essential to obtain the scattering amplitude, the phase shift carries the information of the interaction between the target and the incident particle.

2.2.4 The Optical Theorem

An important, and very useful, property of the scattering amplitude is known as the optical theorem, and was described for the first time by Feenberg [80]. It relates the imaginary part of a forward scattering ($\theta = 0$) to the total cross section [70, 80, 81]. For $\theta = 0$, scattering amplitudes expressed in partial waves (equation 2.17) become

$$f(\theta=0) = \frac{1}{k}\sum_{\ell=0}^{\infty}(2\ell+1)e^{i\delta_\ell}\sin\delta_\ell, \tag{2.21}$$

$$f(\theta=0) = \frac{1}{k}\sum_{\ell=0}^{\infty}(2\ell+1)(\cos\delta_\ell\sin\delta_\ell + i\sin^2\delta_\ell), \tag{2.22}$$

Comparing the above expression with equation 2.19, one has the optical theorem, given by:

$$\sigma_{total} = \frac{4\pi}{k}Im\left[f(\theta=0)\right]. \tag{2.23}$$

2.3 VUV Photoabsorption

The region of the electromagnetic spectrum below 200 nm (about 6.2 eV) is known as vacuum ultraviolet (VUV) region. Ultraviolet and visible radiation are very important for the study and characterisation in molecular spectroscopy. The energy of the photons in these wavelength regions is sufficient to cause electronic and vibrational excitation, when absorbed by molecules.

The use of synchrotron radiation in this type of studies is extremely important because it is possible to obtain intense, highly collimated and highly polarized coherent radiation in the plane of the storage ring with very high spectral resolution. This high intensity with wide spectral space when combined with other properties, such as a high level of polarization and collimation makes synchrotron radiation a powerful tool for research in physics, chemistry, biology and medicine, as well as in technological applications [69].

2.3.1 Photoabsorption Cross Section

When a monochromatic photon beam of known intensity I_0 is incident upon an absorbing sample, a fraction of this light is absorbed, with negligible losses caused by scattering. The photoabsorption process is proportional to the path length X and the particle density N. The constant of proportionality σ is defined as the total photoabsorption cross section, which is dependent of the photon energy. The attenuation of the radiation intensity is given by the Beer-Lambert law, expressed as

$$dI = -I_0 N \sigma dx. \tag{2.24}$$

Integrating over the transmitted intensity of the radiation I_T along the path length leads to

$$\int_{I_0}^{I_T} \frac{dI}{I} = -\int_0^X \sigma N dx, \tag{2.25}$$

$$\ln\left(\frac{I_T}{I_0}\right) = -\sigma N X. \tag{2.26}$$

That can also be written as

$$I_T = I_0 e^{-n\sigma x}. \tag{2.27}$$

Therefore, when the transmitted intensity of radiation I_T is measured from an incident beam of well-known intensity I_0, it is very simple to find the cross section σ, which represents the absorbed radiation. The photoabsorption cross section is clearly related to the quantity

$$\mathfrak{A} = \ln\left(\frac{I_0}{I_T}\right), \tag{2.28}$$

which is the absorbance [63].

The photoabsorption cross section of UV radiation provides results in molecular spectroscopic systems, giving extremely important information for a better understanding of the interaction between radiation and matter, such as the Rydberg and valence excited states, and vibrational states of the studied molecule.

2.3.2 Absorption intensity

As a result of the absorption process, there is a transition in the molecular target from the initial state i to a final state j. Considering n particles of the sample target, restricted in a slab of area A and thickness dx as shown in Figure 2.4, the transition rate $W_{,ij}$ [63, 82], is

$$-\frac{dn}{dt} = nW_{ij}. \tag{2.29}$$

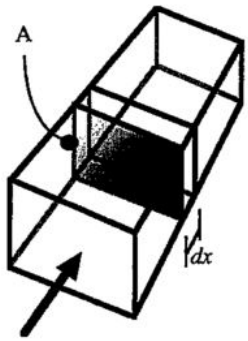

Figure 2.4: Sketch of the photoabsorption within the volume A.dx. Taken from [63].

This process leads to a reduction of the electromagnetic energy through the slab dx, by an amount of $-h\nu\frac{dn}{dt}$. The absorbed intensity I^{abs} is defined as the energy absorbed per unit of time, then the loss in intensity of the radiation dI along dx is:

$$dI = -dI^{abs} = -h\nu\frac{dN}{dt}dx = -h\nu N W_{ij} dx. \tag{2.30}$$

where $N = \frac{n}{Adx}$ is the absorber number density and $h\nu$ is the photon energy.

The transition rate W_{ij} is related to Einstein's coefficient for induced absorption of electromagnetic radiation by molecules in thermal equilibrium, B_{ij} [63, 83], by:

$$W_{ij} = B_{ij}\rho(\nu), \tag{2.31}$$

where $\rho(\nu) = \frac{I(\nu)}{c}$ is the density of radiation. The Einstein coefficient for absorption is expressed, in the electric dipole approximation, using the electric dipole operator μ_{ij}, as

$$B_{ij} = \frac{1}{6\varepsilon_0\hbar^2}\left|\langle\psi_j|\mu_{ij}|\psi_i\rangle\right|^2. \tag{2.32}$$

The integral $\langle\psi_j|\mu_{ij}|\psi_i\rangle$ is the transition dipole moment, which is the electric dipole moment associated with the transition between two states. ε_0 is the permittivity of the free space, and one should remember that $\hbar = h/2\pi$. Combining equations 2.30, 2.31, and 2.32 gives:

$$dI = -\frac{1}{6c\varepsilon_0\hbar^2} I h\nu_{ij} N \left|\langle\psi_j|\mu_{ij}|\psi_i\rangle\right|^2 dx. \tag{2.33}$$

The attenuation of the intensity may be related to a measurable macroscopic quantity, the photoabsorption cross section σ, by the Beer-Lambert law. Combining equations 2.24 and 2.33 results in:

$$\sigma = \frac{h\nu_{ij}}{c}\frac{1}{6\varepsilon_0\hbar^2}\left|\langle\psi_j|\mu_{ij}|\psi_i\rangle\right|^2, \tag{2.34}$$

or

$$\sigma = \frac{h\nu_{ij}}{c}B_{ij}. \tag{2.35}$$

2.3.3 Oscillator Strengths

The concept of oscillator strength emerges from a classical model of the electrical and optical behaviour of matter, dated from the 19th century. In this model, the electromagnetic radiation forces oscillations in the electrons of an atom, that otherwise were in a position of equilibrium with respect to the atom. The electrons actually have a statistical distribution of positions which is fixed under equilibrium conditions but is disturbed by weak perturbation, in the form of oscillations. Thus, the concept of oscillator strength continued to be used to designate the free oscillations of this distribution in atoms and molecules. The oscillator strength is a dynamical parameter which bears on numerous phenomena [84].

For sufficiently low radiation frequencies[6], the Einstein's coefficient and therefore, the transition moment is related to the oscillator strength of a discrete transition by the following expression [85, 86]:

$$f_{ij} = \frac{4m_e\varepsilon_0 h}{e^2}\nu_{ij}B_{ij}, \tag{2.36}$$

so, for a discrete transition:

$$f_{ij} = \frac{4\varepsilon_0 m_e c}{e^2}\sigma. \tag{2.37}$$

For a continuous absorption, the integral over the wavelength should be considered:

$$f_{ij} = \frac{4\varepsilon_0 m_e c}{e^2}\int \sigma(\nu)d\nu, \tag{2.38}$$

where f_{ij}, that is a pure number, is referred to as the optical oscillator strength. After proceeding with the derivative of expression 2.38 as a function of the energy:

$$\frac{d}{dE}\left[f_{ij}\right] = \frac{4\varepsilon_0 m_e c}{e^2}\frac{d}{dE}\left[\int \sigma(\nu)d\nu\right], \tag{2.39}$$

one deducts the spectral density of oscillator strength, given by

$$\frac{df}{dE} = \frac{m_e c}{h\pi e^2}\sigma(E). \tag{2.40}$$

The following chapter describes the theoretical and experimental methods for obtaining the photoabsorption and the electron scattering cross sections.

[6]The concept of low radiation frequencies, for this purpose, implies that the wavelength is much larger than the molecular absorber, and thereby the photon momentum and the Compton scattering can be neglected.

Chapter

3 Methods and Materials

There are two objectionable types of believers: those who believe the incredible, and those who believe that 'belief' must be discarded and replaced by 'the scientific method'.
— Max Born, Natural Philosophy of Cause and Chance

In this work two distinct equipments were used to perform a set of comprehensive experimental measurements: an electron impact spectrometer for scattering measurements and a VUV beamline of a synchrotron storage ring for photoabsorption measurements. Additionally, theoretical calculations were performed, to help interpreting the results, using three different methods: electronic excitation study was performed using the Gaussian package at the University of Lille; the calculations for DCS and ICS were performed by independent atom model - screening corrections additivity rule (IAM-SCAR) and Schwinger multichannel method implemented with pseudopotential (SMC-PP) methods, both provided from the joint research activities, in Consejo Superior de Investigaciones Científicas (CSIC), Spain, and in Universidade Federal do Paraná (UFPR), Brazil, respectively.

This chapter describes all the experimental set-ups and the major working procedures, as well as a brief description of the calculation methods used in this study.

3.1 Electron-Molecule Impact Spectrometer

For the electron-molecule collision measurements a high resolution electron energy loss spectrometer (HREELS) fully installed at the atomic and molecular collision laboratory (LCAM), Centre of Physics and Technological Research (CEFITEC), Universidade NOVA de Lisboa was used to obtain elastic electron measurements from selected molecules where DCS and ICS were obtained.

3.1.1 HREELS Apparatus Description

The HREELS apparatus is a commercial cross beam spectrometer, where the target gas and the electron beam intersect each other with a 90º angle, modified for gas phase measurement. The electron beam is generated in an electron gun, passes through a set of electrostatic lenses and an electron monochromator until it reaches the collision region, where interaction with the sample beam occurs. After the collision, the scattered electron at the chosen angle passes through another set of lenses and lastly is detected by a channeltron electron multiplier that sends the signal to the computer. The analyzer is assembled in a rotatable system, which allows the adjustment of the scattering angle from 0° to 120°. However, there is a restriction regarding small angles (typically $< 7°$) where the discrimination between scattered electron beam and incident electron beam is difficult to discern, due to the detector acceptance angle. From the experimental point of view, a background spectrum was subtracted from the scattering measurements. Yet, as the angle decreases, this background contribution (i.e. the primary beam) has a very significant magnitude increased, compare to the scattered beam, so all angular dependent cross section values were obtained for scattering angles greater than 7°.

The electron impact energy range varies from 5 to 100 eV. The resolution of the measurements, that is given by the full width at half maximum (FWHM) of the elastic peak, is typically between 100 and 250 meV. Figure 3.1 shows an image of LCAM's spectrometer and Figure 3.2 is a schematic representation of the HREEL spectrometer.

Figure 3.1: Picture of the HREELS apparatus, LCAM at faculty of science and technology of NOVA university of Lisbon (FCT-UNL)

The collision chamber, that encompasses the electron gun, the monochromator, the collision region, the analyser and the internal detection system, is made of *mu*-metal, which is a nickel–iron ferromagnetic material. This provides an effective magnetic shield, avoiding that any magnetic field, and particularly that of the Earth, affects the electrons' trajectories.

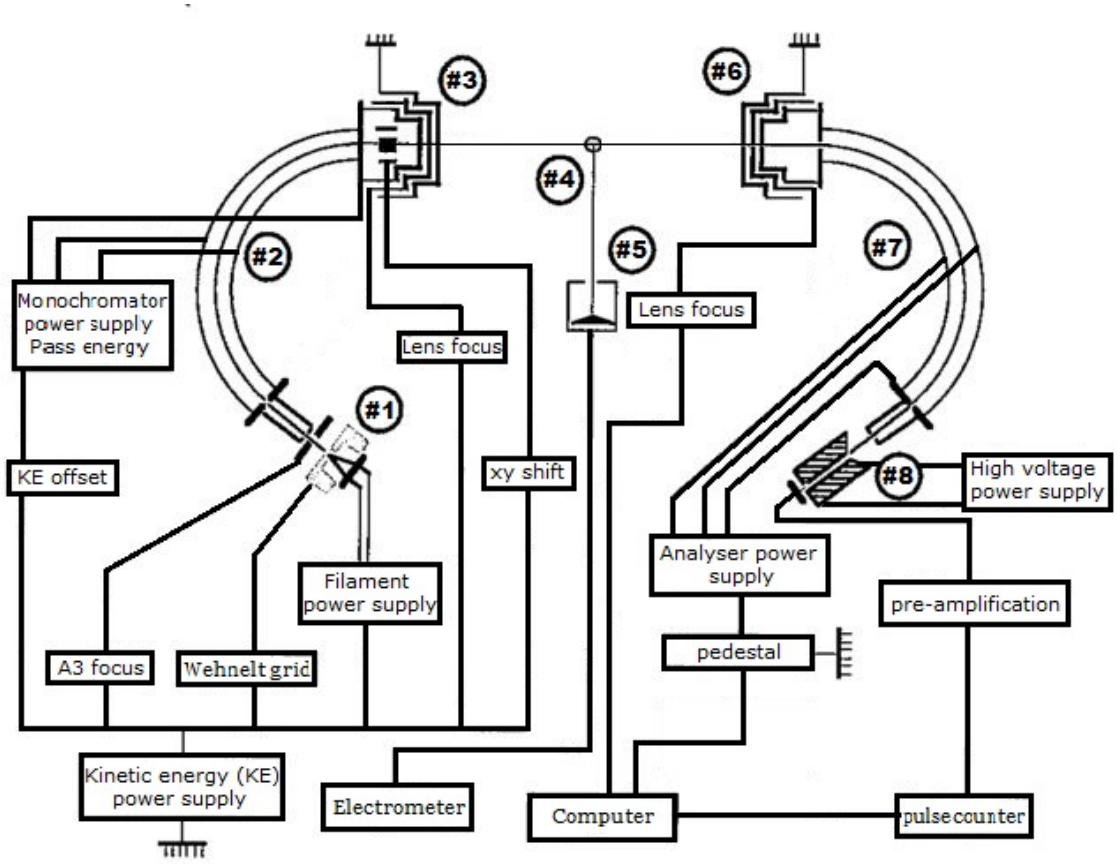

Figure 3.2: Schematic representation of the HREELS apparatus where numbers are related to: #1 electron gun, #2 monochromator, #3 set of lenses, #4 collision region, #5 Faraday cup, #6 set of lenses, #7 analyzer and #8 detection system. Adapted from [63].

◦ Electron Gun

The source of the electron beam is a v-shape toroidal tungsten filament of 1.25 mm thickness assembled at LCAM, exclusively for this apparatus. An electrical current around 2.5 A heats the filament, leading to emission of electrons by thermoionic effect. As for the other components of the electron gun, there are the *Wehnelt* grid and the $A3$ focus, referred in region #1 of Figure 3.2. The former is a cylindrical electrode responsible for the extraction of the electrons whereas the later has the purpose of focussing the emitted electrons onto the entrance slit of the monochromator [63, 87, 88]. The energy distribution of the electron beam at this point is considerably large, around 500 meV, and the total emission measured in the grid is proximally $5 \cdot 10^{-6} A$.

◦ Monochromator

The monochromator is an energy selector to improve the energy resolution delivered by the heated filament, referred in region #2 of Figure 3.2 and schematically represented in Figure 3.3.

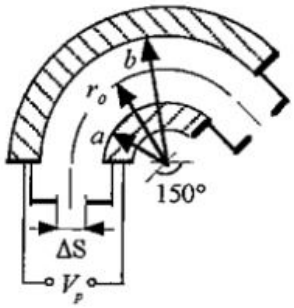

Figure 3.3: Schematic representation of the hemispherical electrostatic monochromator. From [63].

It consists of a pair of spherical electrodes with a curvature of 150° and separated by $9.5mm$, whereupon the pass energy E_0 is defined by the constant voltage V_p applied to the electrodes [63, 87, 89].

$$E_0 = \frac{qV_p}{\left(\frac{b^2 - a^2}{ab}\right)} \tag{3.1}$$

where q is the electronic charge, a and b are the inner and outer radius, respectively, as shown in Figure 3.3.

The entrance and exit slits are diametrically opposed in reference to the centre of the hemispheres. An adjustable constant magnetic field is applied to the monochromator, in order to help the spherical electrodes in leading the electron beam from the entrance to the exit slit. The energy resolution ΔE of the outgoing electrons, delivered by the monochromator is given by:

$$\frac{\Delta E}{E_0} = \frac{\Delta S}{2r_0} + \frac{1}{4}\alpha^2 \tag{3.2}$$

where ΔS is the entrance slit width and α is the angular divergence of the incoming beam between the entrance and exit slit [63, 87, 89, 90].

In order to accelerate the electrons up to the proper pass energy, both entrance and exit slits are biased to a V_0 potential. From there, the energy of the incident electrons E_i is:

$$E_i = qV_0 + E_0 + C \tag{3.3}$$

where C is a constant which depends on the surface potentials and the thermal energy of the electrons emitted by the filament.

A heating device is fixed on the selector and maintains it to approximately $150°C$, in order to reduce the adsorption of the gas target molecule on the surfaces and consequently avoid creating surface potentials [63].

- **Monochromator's Set of Lenses**

A set of electrostatic lenses, labelled #3 in Figure 3.1, are placed after the exit slit of the monochromator and are responsible for focusing the electron beam to the collision region, where it will cross the target beam. The first lens element has the same V_0 potential as the exit slit. The next element is composed by two pairs of plates used to centre the electron beam, named *xy shift*. Next, the beam is guided by the *lens focus* with a V_1 potential and the last element is grounded ($V_G = 0\ V$). The focusing strength is controlled by the ratio V_1/V_0 whilst the ratio V_G/V_1 changes the energy of the image point [63].

- **Collision region**

The collision region is delimited by a molybdenum cylinder, pierced by a circular slit of 130° and $8mm$ length, which allows the entrance of the incident electron beam for different scattering angles. The cylinder is fixed to the optical bench along with the analyzer, in the same rotating plate. The angular position of the analyzer, and consequently the position of the rotating plate, set the scattering angle of the measurement, ranging from 0° to 120º. A hypodermic needle of 1 mm diameter enters from the bottom of the cylinder, in the scattering centre, allowing the gas target beam, to intersect the electron beam. These elements are all grounded.

- **Faraday cup**

The Faraday cup is mounted along with the cylinder of the collision region, and gives the electron's current transmitted through the collision region. It is composed by a an outer cylinder, and a collector electrode placed inside, isolated from the cylinder. The collector is biased by a constant power supply of 12 V and connected to an electrometer. The typical current value measured at the Faraday cup is about $0.1 - 0.5 \cdot 10^{-10} A$.

- **Analyzer**

The analyzer is identical to the monochromator. It is used to energetically analyse the electrons scattered at a certain angle θ. A set of lenses, identical to the monochromator exit lenses, except for the *xy shift* element, is used to focus the scattered electron coming from the collision region onto the entrance slit of the analyser. The analyser and its set of lenses are referred as regions #7 and #6 in Figure 3.2, respectively. As in the monochromator, the third element of the set of lenses is at the same potential, V_{ret}, as the entrance slit of the analyser, known as the retarding potential. Hence, electrons allowed to enter the energy selector must have a residual energy E_r:

$$E_r = E_i - E_l \geq qV_{ret} \tag{3.4}$$

where E_i is the electron impact energy, the initial energy of the incident electron beam in the collision region, and E_l is the amount of energy lost by the electron during the collision, i.e. the amount of energy that is transferred to the molecular target during the interaction. Assuming an optimal adjustment of the analyser lens potential, the electrons will be focused to the analyser exit slit with de following condition:

$$E_r = E_0 + qV_{ret} \tag{3.5}$$

where E_0 is the pass energy of the analyser.

This condition allows scanning for the scattered electrons that lost a specifically chosen amount of energy, by varying the retarding potential V_{ret}. Furthermore, electrons with lower energy than the pass energy can not be analysed, which precludes the scan of very low residual electrons [63, 87].

- **Detection system**

The incoming signal from the analyser is amplified by an electron multiplier of the continuous dynode type channeltron. It is made of lead glass partially reduced, which has the ability to conduct electrons. The typical resistance is 50 $M\Omega$ and a 2.5 kV drop is applied to its terminals. When an electron enters the device and hits the surface, it generates a cascade of secondary electrons. The inner field of the device accelerates the latter and each electron also generates other several secondary electrons, and so on, which results in a controlled amplification of the incoming signal in a very short time, in the order of nanoseconds, turning into a detectable electron current at the output. The gain of an electron multiplier (G), typically of the order of 10^7, is given by the ratio of the output current I_{out} to the number of output pulses N:

$$G = \frac{I_{out}}{Nq_{e^-}} \tag{3.6}$$

Besides having high gains, such devices have little background noise, also known as black current. This appears even in the absence of an input signal, therefore, is produced by the device itself, and the typical value of the noise is of the order of 10^{-4} electrons per second [63, 87].

The output signal from the electron multiplier channeltron is pre-amplified and sent to a counter that accumulates the number of pulses during a chosen time period. The cumulative total is then sent to the desktop computer where it is further divided by the counting time, in order to give the detection rate in number of counts per second and then sent to the data acquisition system.

◦ **Data acquisition system**

In the desktop computer, the data acquisition system is a LabVIEW based software, exclusively developed for this apparatus. Apart from the analogic and power electronics, in order to operate the HREELS some additional digital instrumentation is needed, in particular two Digital to Analog Converters (DAC) and a HP universal frequency counter. The first DAC used allowed us to control the pedestal voltage, for this a octal formatted string is sent with the desired voltage by a simple linear expression, given that this DAC has a 12 bit resolution, the maximum voltage corresponds to 212-1 (decimal) while the minimum voltage to 0, and for the lens voltage a 16 bit DAC was used instead. Once the desired voltages are applied, in order to measure a signal, a formatted string had to be sent to the pulse counter, which will give a start counting signal and for how long it should last, where no command for stopping the counting is needed, once the specified counting time finishes the counter stops automatically. Once the counting is done a command to read the current output provides the amount of counts acquired and an additional command to clear the pulse counter is used after each reading to ensure that the counter will be ready for the next cycle. Communications between all devices were made through a GPIB interface, where a fixed computer acted as a master to all instruments and all devices as terminals. The code was written in LabVIEW, where the GPIB was interfaced through National Instrument's VISA driver.

◦ **Sample admission system**

The sample admission system transports the gas target to the collision region, through a needle. The system currently supports liquid or pressurized gas samples. A needle valve admits the sample from its container into the system, which allows a very precise control of the sample amount. An ionisation gauge mounted in the collision chamber gives a direct measurement of the pressure, which is connected to a pressure security system, that is activated when the pressure rises to $2.5 \cdot 10^{-5}$ *mbar*, shutting down the power supplies to the elements inside the chamber, thus protecting the integrity of those that can be damaged at high pressures. The base pressure inside the chamber reaches $3.0 \cdot 10^{-7}$ *mbar*, and after admission of the gas sample it is maintained between $1.0 \cdot 10^{-5}$ to $1.5 \cdot 10^{-5}$ *mbar*, this ensures that the scattering process is a two-body interaction process [91].

The collision chamber inlet may be closed by a safety valve, isolating the sample supply to it. This makes the maintenance of the apparatus easier and safer, and also allows the degassing of the liquid samples in three cycles of freeze-pump-thaw.

3.1.2 HREELS Operating Mode

In this work, two different types of measurements were performed, an angle resolved electron energy loss at a fixed impact energy and an angle resolved elastic scattering at fixed impact energy.

After the collision with the target, the electrons are scattered with a residual energy distribution, that is recorded in terms of their intensities versus the energy loss. It is therefore possible to analyse the elastic peak, i.e. electrons that are scattered at a particular scattering angle with no energy loss, as well as the energy loss or excitation energy transferred to the target, considering that the initial impact energy is well-known. Scanning the residual electron energy is achieved by applying a retarded voltage to the third element of the analyzer set of lenses, also known as the retarding potential.

Electron beam optimisation is performed by a set of preliminary tests in the Faraday cup, that are related to a fine tuning of the monochromator and its set of lenses, with the purpose of obtaining a current in the order of $10^{-11}A$ in the electrometer. Next, the potentials are re-adjusted in order to obtain an optimal well-resolved sharp elastic peak at a small angle (usually 7°), the intensity of the scattered electron beam in the elastic peak depends on the molecular target, as well as the FWHM, determining the accuracy of the measurements. The precision depends on the step size used for a particularly scan, that is typically 20 meV.

The calibration of the incident electron beam's energy is also performed in terms of the elastic peak, which corresponds to a zero energy loss. The energy value recorded by the data acquisition system, at the exact central position of the elastic peak, during a scan, corresponds to the energy shift. A simple subtraction allows the determination of the precise incident energy. Such a shift is essential, so that the entire curve corresponding to the elastic peak may be displayed by the software.

For each specific incident energy and scattering angle, a spectrum is obtained through a set of several scans, in order to accomplish a reasonable signal-to-noise ratio statistical data analyses, where each of the scans is individually verified and treated for black current, and any scan that shows signal from external sources is rejected. In this way, the methodology to obtain DCS is achieved by adjusting area the of a Gaussian curve to the respective spectrum. Since these values are not absolute, due to the absence of the relative flow system, they are normalized to the calculated data.

3.2 Photoabsorption Spectrometer

The VUV photoabsorption spectra were measured at the AU-UV beam line on the ASTRID2, at the Department of Physics and Astronomy, Aarhus University, Denmark.

The beam was designed to cover the low photon energy region about 700 to 100 nm (1.77 to 12.39 eV). The monochromator provides a high flux with high resolution, and preserves the high degree of linear polarization of the synchrotron radiation source. The synchrotron radiation, with the selected wavelength, passes through a static gas sample, after that a photomultiplier is used to measure the transmitted light.

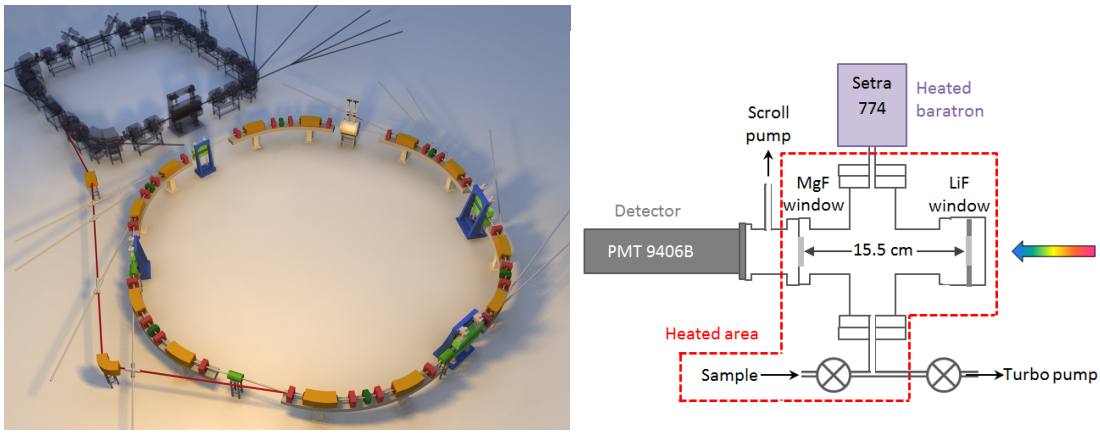

(a) ASTRID2 storage ring.

(b) Photoabsorption apparatus.

Figure 3.4: Left: Representation of ASTRID2 storage ring (in colour) with ASTRID in the background. Right: Schematic diagram of the gas phase photoabsorption apparatus. Both from [92].

3.2.1 ASTRID2 Apparatus Description

The AU-UV beam line was originally commissioned for Aarhus storage ring in Denmark (ASTRID) in 2000, as UV1 beam line [92] and is described in detail in *Eden at al* [93]. In September 2013 the Aarhus storage ring in Denmark 3rd generation light source (ASTRID2) (schematically shown in Fig. 3.4a), has experienced significant changes.

The energy of the circulating electrons in ASTRID2 is 580 MeV, it has a horizontal emittance of 12 nm and the source is optimized to produce synchrotron radiation in the few eV to 1 keV energy range. Beam lifetime is effectively infinite using top-up of the electron current with ASTRID. ASTRID2 has a diameter of 15 m.

- **The ultraviolet beamline of ASTRID2**

The original ASTRID beam line, at 1.70m of distance from the source to the first mirror, could not be directly attached to the new storage ring ASTRID2, as a radiation protection wall had to be accommodated. Therefore, a set of pre-optical mirrors, comprised by a toroidal mirror (TM1) and a plane mirror (PM), were installed to image the source to an

intermediate focus (IF), schematically depicted in Fig. 3.5, which acts as a source for the existing beam line without further alteration. From there, a toroidal mirror (TM2) focuses the incoming beam onto the entrance slit of the monochromator (ENS), which is typically set to 100 μm for photoabsorption measurements. The light then passes to a toroidal grating (G). There are two gratings available, a high energy grating with a line density of 2000 lines/mm covering 100 to 350 nm (12.40 to 3.54 eV) and a low energy grating with a line density of 1000 lines/mm covering 160 to 700 nm (7.75 to 1.77 eV), the wavelength is scanned by a simple rotation of the grating. The light exits the monochromator via a moveable slit (EXS), also set to 100 μm, and passes through a lithium fluorine (LiF) window which separates the beam line from the ultra-high vacuum chamber at the end of the station experiment. The monochromator has been designed to provide a high flux with a high resolution and to preserve the high degree of linear polarization of the synchrotron. The resolution of the monochromator, using the primary grating for high resolution photoabsorption measurements, has been measured as better as 0.08 nm over the operational range of the grating, close to the calculated value of 0.075nm [93, 94].

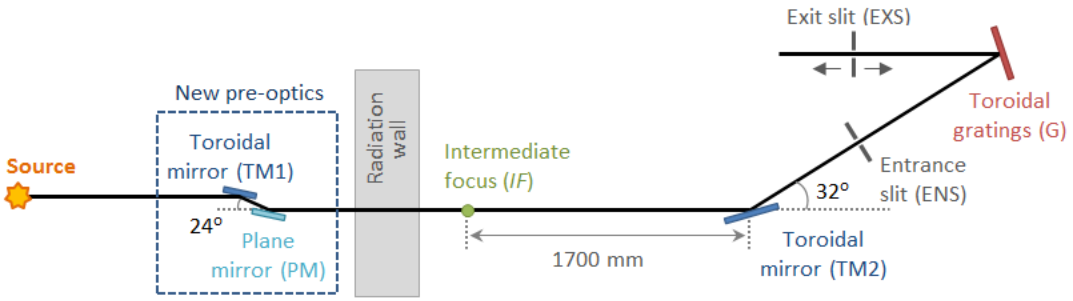

Figure 3.5: Schematic diagram of the gas phase photoabsorption apparatus, taken from [92].

◦ The VUV photoabsorption apparatus

The apparatus used for measuring of photoabsorption spectra has also undergone several alterations with the implementation of ASTRID2. The new chamber, shown in Fig 3.4b, which allows heating up to 80°C of the sample during measurements, has a path length of 15.5cm and is fitted with a heated 1$Torr$ Baratron capacitance manometer (Setra model 774).

After entering the absorption cell athwart the LiF window, the synchrotron radiation passes through a static gas sample. The light exits the cell through a magnesium difluorine (MgF_2) window, which sets the lower limit of detectable light to 115nm. A photomultiplier tube (PMT) detector is used to measure the transmitted light intensity. The gap between the detector and the absorption cell is evacuated using a scroll pump, for measurements below 200nm, Above 200nm, air is allowed into this gap to let oxygen absorb higher orders of light (at half the chosen wavelength) which may be passing through the cell.

Hence, photoabsorption measurements can be performed with spectrally pure radiation from $115nm$ to $320nm$, ensuring artefact-free spectra [92–95].

3.2.2 ASTRID2 Operating Mode

Using the intensity of the transmitted light and a background scan recorded with the cell evacuated, the absolute photoabsorption cross-sections (σ) are obtained using the Beer-Lambert law:

$$I_T = I_0 e^{-n\sigma x} \tag{3.7}$$

where I_T and I_0 are the detector signal transmitted through a gas and for an evacuated cell (background), respectively, n is the molecular density, which depends on the pressure measurement, and x is the cell path length, that is $15.5cm$.

First a spectrum of the whole wavelength range is performed, in order to evaluate the structure as a whole. After that, the VUV spectrum is recorded in small sections, typically of 5 or $10nm$, with at least $1nm$ overlap to the adjoining sections. For each section of the spectrum, a scan with no gas in the cell is recorded (I_0). Then, an appropriate pressure of sample for each range is selected so that the incoming light was attenuated by 40%-50%, which is low enough to prevent line saturation effects and two scans of the sample in a static gas cell are recorded (I_T). The cell is then evacuated and a second scan of the empty cell is recorded. Consistency between the two I_T scans recorded and the good overlap of the sections of the spectrum indicated no pressure changes of the sample in the cell during the time-scale of the measurements.

ASTRID2 is operated in a so-called top-up mode, keeping the stored electron beam current (and thus the intensity for a given wavelength) quasi constant by adding small amounts of current to ASTRID2 to make up for the constant beam decay. The beam current thus varies about 5% during a scan, and this is taken into account by recording and normalizing to an accurately determined beam current.

3.3 IAM-SCAR Method

The independent atom model (IAM) method assumes that when an electron scatters from a molecule, this process can be described by the interaction of an electron with the atomic constituents in the corresponding positions, so the electron–molecule collision is reduced to the problem of a collision with individual atoms. This approximation does not consider the simultaneous interaction of the incident electron with more than one atom. For this reason, despite the excellent behaviour for medium to large energies, good results for low energies (bellow 20 eV) are not to be expected due to its semiclassical nature [96, 97]. The screen corrected additivity rule (SCAR) procedure [96] incorporates the geometrical screening corrections, that is neglected by the IAM method in its simplest description.

3.3.1 Scattering amplitude

In the procedure used for calculating the corresponding atomic cross-section, the electron–atom interaction is represented by the approximate *ab initio*[1] optical potential

$$V_{opt}(r) = V_S(r) + V_e(r) + V_p(r) + iV^a(r), \tag{3.8}$$

where the imaginary part $V^a(r)$ stems for the absorption potential in complete form, proposed for the quasifree absorption model potential [98], and the real part $V(r)$ is the effective atomic potential including three terms: $V_S(r)$ is the static potential calculated by using the charge density deduced from Hartree-Fock [58] atomic wave functions[2]; $V_e(r)$ is the exchange potential for which the semiclassical energy-dependent formula derived by Riley and Truhlar [99] is used; and $V_p(r)$ represents the target polarization potential [100].

In order to obtain the *l-th* partial wave phase shift $\delta_l = \lambda + i\mu_l$, the scattering equation for the $\mu_l(r)$ radial wave functions has been numerically integrated [101] by means of an adaptive-step-size fourth-order Runge-Kutta algorithm [102] based on the variable-phase technique [103]. Once the corresponding δ_l phase shifts are obtained for the above potential, the elastic differential cross section result from the method of partial wave, shown in section 2.2.3, is given by the following expressions:

$$f(\theta) = \frac{1}{k}\sum_{\ell=0}^{\infty}(2\ell+1)e^{i\delta_\ell}\sin\delta_\ell P_\ell(\cos\theta), \tag{3.9}$$

$$\frac{d\sigma}{d\Omega} = |f(k,\theta,\phi)|^2. \tag{3.10}$$

For the elastic scattering process, calculations were carried out without the absorption therm $iV^a(r)$ in equation 3.8, and for the inelastic scattering this complex term remains.

3.3.2 Screen corrected additivity rule

Within the IAM methodology, calculation of the collision cross sections proceeds by means of the approximate expression for multi-centre dispersion [104]

$$F(\theta) = \sum_{atoms} f_i(\theta)e^{i\vec{q}.\vec{r}_i} \tag{3.11}$$

where $\vec{q}$ is the momentum transfer, $\vec{r}_i$ are the atomic positions and $f_i(\theta)$ are the atomic scattering amplitudes. According to the optical theorem, shown in section 2.2.4, the total cross section is then [98]

$$\sigma_{total} = \frac{4\pi}{k} Im\left[F(\theta=0)\right] = \frac{4\pi}{k}\sum_{atoms} Im\left[f_i(\theta=0)\right]. \tag{3.12}$$

In this method the overlapping between total atomic cross sections is calculated for every constituent atom with respect to all the other atoms of the molecule [105], screening

[1] *Ab initio* is a latin expression that means "from the beginning". By *ab initio* calculations is understood theoretical modelling processes that do not require the input of experimental data.

[2] The Hartree-Fock method is explained in detail in appendix A

corrections for molecular total cross sections can be introduced by means of a modified additivity rule [97]

$$\begin{aligned} \sigma_{total} &= \sum_i S_i \sigma_i^{total}, \\ \sigma_{elastic} &= \sum_i S_i \sigma_i^{elastic}, \end{aligned} \tag{3.13}$$

where the screening correction coefficients S_i account for the geometrical overlapping of the atoms in the molecule as seen by the incident electrons [96, 97, 105, 106]. The S_i factor is basically a $1-S_i$ fraction of each atom that are geometrically hidden by the surrounding atoms, which means that the incident flux in each atom is reduced by the S_i factor. Those multiple overlappings can be approximately calculated in a recurrent way, considering for each additional atom the screening with the previously corrected ones [105].

$$S_i = \sum_{k=1}^{N} \frac{(-1)^{k+1} \epsilon_i^k}{k!} \tag{3.14}$$

Here N is the number of atoms of the molecule, and each ϵ_i^k parameter arises from k-atoms overlapping and results from the sequence

$$\begin{aligned} \epsilon_i^1 &= 1, \\ \epsilon_i^k &= \frac{N-K+1}{N-1} \sum_{j(\neq 1)} \frac{\sigma_j \epsilon_j^{(k-1)}}{\alpha_{ij}}, \ (K = 2, ..., N) \end{aligned} \tag{3.15}$$

where the sum extends over all the atoms of the molecule except for the ith one. It can be noted that this treatment allows an approximate calculation of the multiple overlapping in arbitrary molecules, requiring only the corresponding atomic cross sections and the relative positions of its constituent atoms, without limitations from molecular symmetry considerations and using no adjustable parameters, where correction to the range of validity of the IAM-SCAR method might be extended down to about $20eV$ [96, 97, 105–107].

The DCS calculation, both for elastic and inelastic scattering, needs some additional considerations: a detail treatment is very difficult, for this reason a semiclassical interpretation is used, which gives a very good approximation in a simple approach.

It is important to notice that due to the average geometrical screening of the rest of the molecule the flux of incident electrons in each atom is reduced in a S_i factor ($\sqrt{S_i}$ factor for the scattering amplitude). However, the scattering amplitude of the outgoing molecular wave for the direct interaction with the atom is not $\sqrt{S_i} f_i$, but $S_i f_i$. That happens because the outgoing wave of the atom is reduced again in another $\sqrt{S_i}$ factor by the other atoms, i.e. the rest of the molecule, as represented in Figure 3.6.

Thereby, two distinctive contributions in the DCS should be consider, one contribution of the direct interaction with the atom and a second ensuing redispersed contribution, for both elastic and inelastic DCS.

$$\frac{d\sigma}{d\Omega} = \frac{d\sigma^{direct}}{d\Omega} + \frac{d\sigma^{redispersed}}{d\Omega}. \tag{3.16}$$

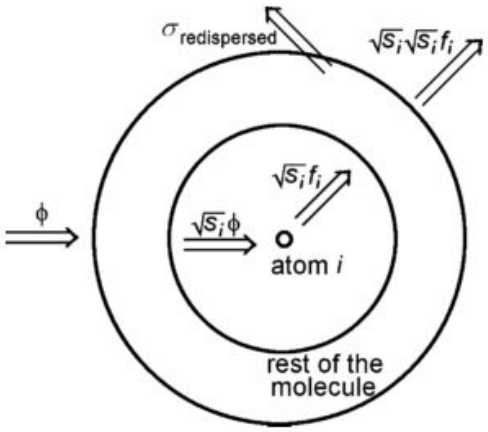

Figure 3.6: Schematic analysis of the screening coefficients for wave amplitudes corresponding to direct and redispersed contributions to the observed differential cross section, taken from [97].

So, the resulting expression for the DCS, considering both contribution is:

$$\frac{d\sigma}{d\Omega} \cong (1 - X_s)\frac{\sigma - \sigma_D}{4\pi} + \left[1 + X_s\left(\frac{\sigma}{\sigma_D} - 1\right)\right]\frac{d\sigma_D}{d\Omega} \tag{3.17}$$

Where σ_D, X_S and $\frac{d\sigma_D}{d\Omega}$ are defined by

$$\sigma_D = \sum_i S_i^2 \sigma_i, \tag{3.18}$$

$$\frac{d\sigma}{d\Omega} = \sum_{i,j} S_i S_j f_i(\theta) f_j^*(\theta)\frac{\sin(qr_{ij})}{qr_{ij}}, \tag{3.19}$$

and

$$X_s \approx \frac{\int_0^{\pi/4} \frac{d\sigma_D}{d\Omega}\sin\theta d\theta}{\int_0^{\pi} \frac{d\sigma_D}{d\Omega}\sin\theta d\theta} \tag{3.20}$$

considering that $q = 2k\sin(\theta/2)$ is the momentum transfer and $\sin(qr_{ij})/(qr_{ij}) = 1$ for $i = j$.

From the above description of the IAM-SCAR procedure, it is obvious that vibrational and rotational excitations are not considered in this calculation. However, for polar molecules additional dipole-induced excitation cross sections can be considered. Basically, the calculation is performed for differential and integral rotational excitation cross sections for a free electric dipole in the framework of the first Born approximation (FBA) which can be incorporated into the IAM-SCAR calculation by just adding the results as an independent channel [96].

In this work, the calculations with the IAM-SCAR method were performed by the work group of Professor Gustavo García, CSIC Madrid, Spain.

3.4 SMC Method

The Schwinger multichannel (SMC) method [78] is an *ab initio* method that uses $(N+1)$-particles[3] square integrable basis functions to obtain the scattering amplitude for electron-molecule collisions [56, 60, 108–111]. Based on the Schwinger variational principle [112], it is applicable to polyatomic molecular targets with arbitrary geometries.

The first step is the description of the target-molecule, which requires the solution for the *Schrödinger* equation for the problem of multiple electrons:

$$\mathcal{H}_e|\psi\rangle = \mathcal{E}_0|\psi\rangle, \tag{3.21}$$

were $\mathcal{E}_0$ is the eigenvalues of the electronic Hamiltonian $\mathcal{H}_e$, and $|\psi\rangle$ its eigenstate. The wave function of the ground state of the target molecule is obtained with the *Hartree-Fock* method[4] [58], where the description of the target molecule was presented in section 2.1.1.

3.4.1 Schwinger variational principle

Based on the *Schwinger* variational principle [78, 79, 113, 114], the SMC method is a variational strategy that considers the fixed nuclei *Born-Oppenheimer* approximation and includes important effects such as exchange, polarization, and electronic multichannel coupling.

The scattering wave function (the eigenstates $\Psi_{\vec{k}_{i,f}}$) is given by the *Lippmann-Schwinger* equation [56, 78, 115, 116]:

$$|\Psi^{(\pm)}_{\vec{k}_{i,f}}\rangle = |S_{\vec{k}_{i,f}}\rangle + G_0^{(\pm)} V |\Psi^{(\pm)}_{\vec{k}_{i,f}}\rangle, \tag{3.22}$$

that is basically the solution of the *Schrödinger* equation for the electron-molecule collision problem, given the sum of the general solution $S_{\vec{k}_{i,f}}$ (without considering the interaction between the incident electron and the molecular target) with a particular solution obtained by the method of Green's function. The V operator is the potential of interaction of the incident electron with the target-molecule, and G_0 is the Green function which carries the boundary conditions, given by

$$G_0^{(\pm)} = \lim_{\epsilon \to 0} \frac{1}{E - \mathcal{H}_0 \pm i\epsilon}. \tag{3.23}$$

that considers the total energy of the collision E and the Hamiltonian without interaction

$$\mathcal{H}_0 = T_{N+1} + \mathcal{H}_e \tag{3.24}$$

where T_{N+1} is the operator of kinetic energy of the incident electron [56, 60, 79, 113], the term $i\epsilon$ is a mathematical tool, inserted in the denominator to remove any possible

[3] The notation $(N+1)$ represents the N electrons of the molecular target plus the incident electron.
[4] The Hartree-Fock method is explained in detail in appendix A.

singularity of the function, and the superscript $(\pm)$ is associated with the behaviour of the wave function in the asymptotic region[5].

The equation 3.22 is multiplied by the interaction potential V and then projected into the open channels. After some considerations and mathematical strategies[6] one obtains

$$A^{(\pm)}|\Psi_{i,f}^{(\pm)}\rangle = V|S_{i,f}\rangle \tag{3.25}$$

with

$$A \equiv \frac{H}{N+1} - \frac{HP+PH}{2} + \frac{VP+PV}{2} - VG_PV, \tag{3.26}$$

in which $H = E - \mathcal{H}_0$, P is a projector onto the open energy-allowed target electronic channels, and G_P is the free-particle Green's function projected onto the P space.

The scattering amplitude is then given by the bilinear form of the Schwinger variational principle:

$$[f(\vec{k}_i,\vec{k}_f)] = -\frac{1}{2\pi}\left[\langle S_f|V|\Psi_i^{(+)}\rangle + \langle\Psi_f^{(-)}|V|S_i\rangle - \langle\Psi_f^{(-)}|A^{(+)}|\Psi_i^{(+)}\rangle\right]. \tag{3.27}$$

Since the scattering amplitude is expanded in a set of integrable square base functions, the method has limitations regarding long range interactions. For molecules with permanent dipole momentum, a procedure known as *Born closure* is used to fix that issue. In this procedure the physical information contained in the lower partial waves is recovered using the scattering amplitude of the dipole potential obtained by the FBA [78, 116] to complete the scattering amplitude obtained by the SMC method.

In the Schwinger multichannel method, the calculations can be performed at two approximation levels: the static-exchange (SE), and the static-exchange plus polarization (SE+P) approximations. In the SE approximation, only Coulomb's and exchange interaction are taken into account. In this approach the incident electron interacts with a static configuration of the electronic cloud of the molecule which does not provide a satisfactory description of the scattering process for lower energies (typically below 10 eV), but it is quite reasonable for higher energies. In the SE+P approximation are included the temporary electron cloud deformation effects of the target molecule due to the longer interaction with the incident electron in the low energy regime, which provides a more precise description of the scattering process for such cases.

A particularity of these calculations is the implementation of the method using pseudopotentials [117]. In the low energy scattering process, the incident electron does not interact with the atomic core, only valence electrons are accessible. Thus, it is possible to replace the innermost electrons of the molecule with a pseudopotential, in the description

[5] In the $(\pm)$ superscript, the $(+)$ sign means an outgoing wave, where there is an incidence plane wave and a divergent spherical wave scattered, the (-) sign means an incoming wave, where incidence of a convergent spherical wave and a scattered plane wave. Although it does not have a physical meaning, it is quite useful in terms of calculation.

[6] The strategy for numerical evaluation of the residue of the VG_PV term was developed by Gibson and is explained in detail in [60].

of the target molecule, without any loss in the description of the scattering process. Implementation using pseudopotentials has the advantage of reducing computational cost in scattering calculations, especially for large molecules.

In this work, the SMC method implemented with pseudopotentials in the SE and SE+P levels were used to calculate elastic differential cross-section, and were performed by the group of Professor Márcio Bettega, UFPR Curitiba, Brazil.

3.5 Gaussian

Ab initio calculations of the electronic structure and electronic excitation were performed with time dependent density functional theory (TD-DFT) to determine the excitation energies of neutral molecules [118].

The density functional theory (DFT) calculations were performed using the **LC-ωPBE** long range corrected functional [119–121] and has been implemented with the **Gaussian 09** code [122], using Dunning's basis sets aug-cc-pVTZ and aug-cc-pVQZ [123] for all atoms, and a set of diffuse (5s5p2d) orbitals, taken from Kaufmann *et al.* [124] were added to the centre of each molecule. The nature of the transitions was assessed by visual inspection of the natural transition orbitals (NTOs) [125], computed for each calculated triplet and singlet transitions [118]. Then the properties of the excited states (energies and oscillator strengths in the length gauge) were obtained using TD-DFT for both triplet and singlet states.

Those calculations were performed during a short term scientific mission (STSM) at the Universitè de Lille 1, under the supervision of Professor Denis Duflot, Lille, France.

Chapter

4 Results: Electron Scattering

But the reason I call myself by my childhood name is to remind myself that a scientist must also be absolutely like a child. If he sees a thing, he must say that he sees it, whether it was what he thought he was going to see or not. See first, think later, then test. But always see first. Otherwise you will only see what you were expecting.
— Douglas Adams, So Long and Thanks for All the Fish

4.1 Introduction

In this chapter we present the experimental results concerning elastic electron scattering by sevoflurane ($C_4H_3F_7O$), isoflurane ($C_3H_2ClF_5O$), and halothane ($C_2HBrClF_3$) molecules. Differential cross sections (DCS) were measured in the incident electron energy range from 10 to 50 eV, in a high-resolution electron energy loss spectrometer (HREELS), described in section 3.1.

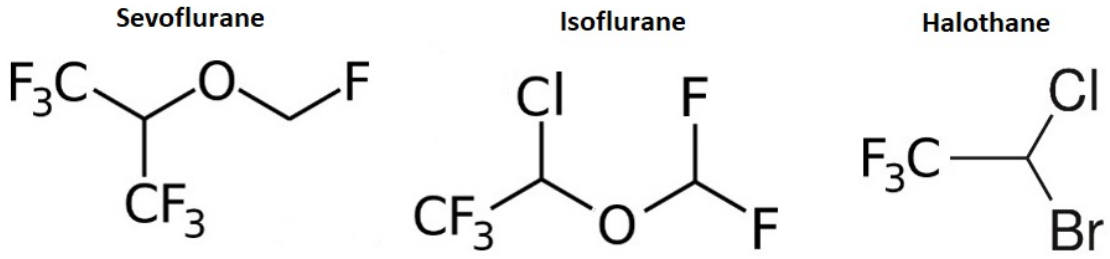

Figure 4.1: Representation of the isoflurane, sevoflurane and halotane molecules.

To assist in the interpretation of the results, the experimental data is combined with theoretical studies, obtained using two different but complementary methodologies: the

Schwinger multichannel method implemented with pseudopotentials ($SMC-PP$), independent atom model - screening corrections additivity rule plus interference (IAM-SCAR+I)[1]. Both methods were performed by collaborating work groups, and are described in chapter 3. These methods are complementary because, although the IAM-SCAR+I method has been proved to be very successful in describing the electron scattering process at intermediate to high energies (above 20eV) [126, 127], for low-energies the description does not follow the experimental findings, due to the interactions of the low energy incident electron with more than one atom of the target molecule at a time [97, 128] (more significant at lower energy due to the interaction time). On the other hand, the SMC-PP method has a very well-established efficacy in elastic scattering up to 20 eV of electron incident energies, whereas above this energy, the calculations tend to overestimate the experimental data. That is due to the inelastic channels that are considered closed, even though they should be open at those energies. As a consequence, there is no flux loss from the elastic channel into the inelastic ones, responsible for lowering the magnitude of the elastic cross sections [60], as actually happens. This joint experimental and theoretical procedure has provided an accurate description of the electron scattering processes in different molecular targets [129, 130]. It has been recently implemented in our laboratory in the case of electron scattering from acetone [131], chlorobenzene [132], and dichloroethane [133]. As far as we are aware, no other experimental elastic DCSs data of sevoflurane, isoflurane or halothane are available in the literature to compare with.

4.2 Experimental Details

In the experimental results presented in this chapter, the energy resolution (full width at half maximum, FWHM) of the incident electron beam was typically 230 meV. The incident electron current was of a few nA, depending on the initial electron energy, and the calibration of the energy loss scale has been obtained according to the position of the elastic peak, as discussed in section 3.1.2. The absolute scale of the present differential cross sections (DCSs) was set by the close comparison with theoretical results.

The experimental uncertainties of the differential cross sections lie in the range of 18%–35%. To estimate the uncertainty value (E_T), one must consider the instability of beam current (E_A) and of the target gas pressure (E_B), the number of total counts N ($E_C = 1/\sqrt{N}$), which is associated with the statistical accuracy, and the Gaussian fitting error (E_D).

$$E_T = \sqrt{E_A^2 + E_B^2 + E_C^2 + E_D^2} \tag{4.1}$$

High uncertainties ($\sim 35\%$) appear at the highest measured scattering angles, this is because at these angles the total number of counts is very small, leading to a high value of E_C. This

[1] All the data presented in this work, obtained through the independent atom model (IAM), were calculated using the screening-corrected additivity rule (SCAR) and including the interference terms, i.e., obtained through the IAM-SCAR+I procedure. However, it may be referred to, throughout this work, as IAM-SCAR, or only IAM, for the sake of simplification.

very low number of counts per second, leading to the inability of obtaining a reasonable signal-to-noise ratio, is also the reason why it was not possible to get experimental values for scattering angles higher than 70°, for sevoflurane and isoflurane molecules, and 100°, for halothane.

The present set of data has been obtained for electron scattering angles starting at 8°, so the dipole driven behaviour is not particularly enhanced among the DCS data, since the effects of the molecular dipole are most often seen at very small scattering angles. However the polarizability effect may contribute as the main factor, since elastic electron scattering is electron-energy-dependent and may either enhance or decrease the scattering cross section, as stated by Dolmatov *et al.* [134].

The integral cross sections (ICS) were obtained from the measured DCSs, extrapolated for scattering angles $\theta > 70°$ and $\theta < 10°$, by using the calculated angular distributions from the present IAM-SCAR+I calculations. Uncertainties on the integral cross sections are estimated to be about 20%.

4.3 Sevoflurane

Sevoflurane physicochemical properties relevant to the present electron scattering experiments are related to a permanent dipole moment of $2.27D$ [135] and a molecular polarizability (α) of significant magnitude, 8.95Å^3 [136]. The sample for which measurements were taken, is a sevoflurane liquid sample, supplied from Alfa Aesar, with a quoted purity of $\geq 98\%$ (under the name fluoromethyl 1,1,1,3,3,3-hexafluoroisopropyl ether, and CAS number 28523-86-6). The sample was degassed by repeated freeze-thaw pumped cycles.

The overall energy resolution of the incident electron beam was about 230 meV for 10 eV electron impact energy and better than 180 meV for 20, 30 and 50 eV electron impact energies. Since the experimental data have been obtained for electron impact energies $\geq$ 10 eV, and no appreciable vibrational contributions are expected in comparison with the elastic signal, the low-lying vibrational modes of sevoflurane [137] are not expected to make any significant contribution to the measured elastic cross sections.

The experimental data on electron scattering elastic differential cross sections (DCS) are shown in Figure 4.2 at four different impact energies, 10, 20, 30 and 50 eV for scattering angles from 8° to 70°, together with the complementary theoretical models. The absolute scale of the experimental elastic DCS is obtained through normalization with the IAM-SCAR+I calculation[2], at 20° scattering angle for 10, 20 and 30 eV, and at 30° scattering angle for 50 eV. The experimental normalized DCSs are tabulated as numerical values in Table 4.1.

The differential cross sections, in Figure 4.2, show that at 10 eV of electron incident energy there are two minima, the first around 50° and the second between 110° and

[2]The DCSs calculated using the independent atom model with (IAM-SCAR+I+Rot) and without (IAM-SCAR+I) considering the dipole interactions have practically identical magnitudes for angles higher than 10°. Therefore, the normalization of the experimental data using any of them is similar.

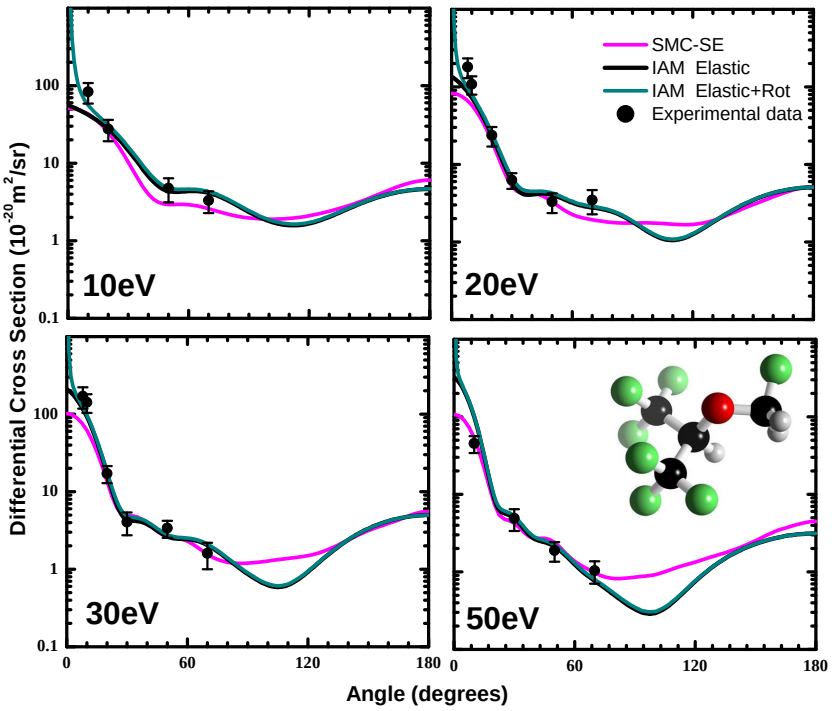

Figure 4.2: Differential cross sections (DCS) for electron scattering from sevoflurane molecule in the incident electron impact energy region 10–50 eV. Theoretical elastic scattering DCSs were obtained at the SMC-PP and IAM-SCAR+I levels.

120°. In the DCS obtained by the IAM-SCAR method these two structures are very recognizable, although not very prominent, while in the SMC cross section, the second minimum is extremely subtle. The two minima remain present in the DCSs for all the energies, and for both calculated methods, where the second shifts to lower scattering angles with the increase of the incident electron energy. In the IAM-SCAR cross section the second minimum also becomes more pronounced as the energy increases. This explains why we were not able to perform measurements at 100°. The calculations using both methods show a good agreement with the experimental data. At low scattering angles, the experimental data seems to overestimate the SMC cross section, but this is reasonable since the calculations have been performed without the Born closure procedure, which takes into account the effects of the permanent dipole moment, very significant at low scattering angles.

Interestingly to observe from a close inspection of Figure 4.2 is that the IAM-SCAR+I calculated differential cross sections, agree very well with the SMC-PP method for low-scattering angles, for all the energies investigated. This is another assertion of the validation of both methods in the description of elastic differential cross section. Given the experimental restriction to obtain reliable DCSs above 70° scattering angle, notwithstanding, above 20 eV electron impact, the shape of the differential cross sections are perfectly described by the two theoretical methods, where a third discernible minimum at 30° is also visible.

In Figure 4.3 we show the elastic integral cross section obtained from the experimental

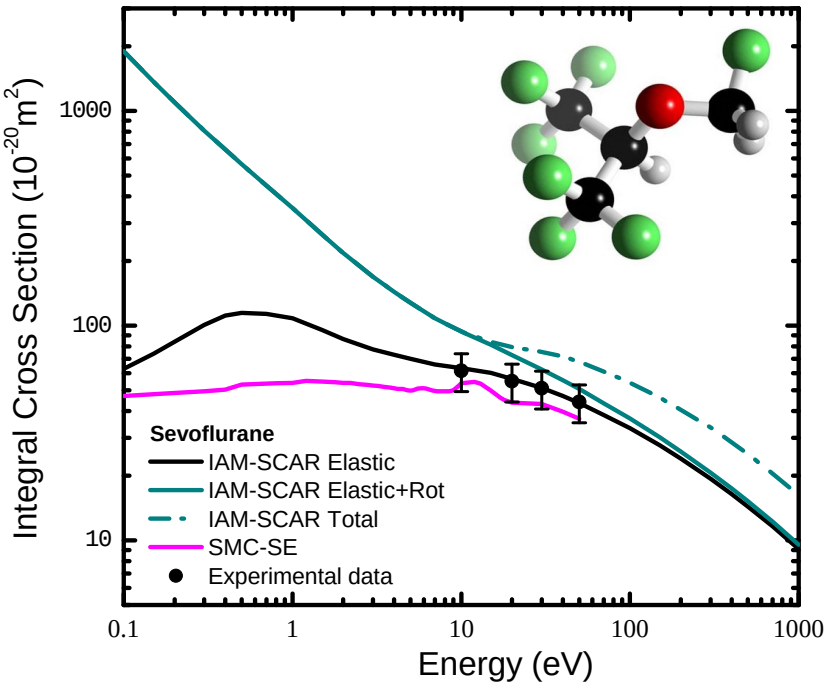

Figure 4.3: Integral cross sections ($10^{-20}m^2$) including the experimental data on electron scattering from sevoflurane molecule together with the theoretical calculations using the SMC-PP and the IAM-SCAR+I methods. Also included the IAM-SCAR+I+Rot cross section.

Angle	10 eV	20 eV	30 eV	50 eV
8°		180.9	170.0	
10°	83.4	108.0	142.2	45.2
20°	27.6	23.7	17.1	
30°		6.3	4.1	4.9
50°	4.8	3.3	3.4	1.9
70°	3.3	3.5	1.6	1.2
ICS	**61.6**	**55.1**	**51.1**	**44.1**

Table 4.1: Experimental differential and integral cross sections ($10^{-20}m^2$) for elastic scattering from sevoflurane molecule. Typical errors on the DCSs are 20% - 30% and for the ICSs are $\sim 20\%$.

elastic DCS, compared with the theoretical ICS calculated from both models. The experimental data is in perfect agreement with the IAM-SCAR+I ICS, and although the ICS from the SMC method shows a somewhat smaller magnitude, it is not very discrepant, within the estimated uncertainty of the data obtained from the experimental measurements. It is also possible to observe, in the total cross section obtained from the IAM-SCAR method, shown in Figure 4.3, that the inelastic scattering channels are opened around the electron incident energy of 11 eV[3], Such is also reinforced by the VUV spectrum of sevoflurane that shows several excited electronic states already operative above 9.0 eV [138].

[3]The ionization energies calculated through OVGF+P3 propagator method are shown in chapter 5.

4.4 Isoflurane

The relevant properties of the isoflurane molecule in the present electron scattering process are the permanent dipole moments and the molecular polarizability, which are $2.47D$ [139], and $\alpha = 9.10\text{Å}^3$ [136], respectively. The sample was degassed by repeated freeze-thaw pumped cycles.

Alfa Aesar was also the supplier of the isoflurane liquid sample used in the measurements, with a quoted purity of $\geq 97\%$ (under the name 1-chloro-2,2,2-trifluoroethyl difluoromethyl ether, and CAS number 26675-46-7).

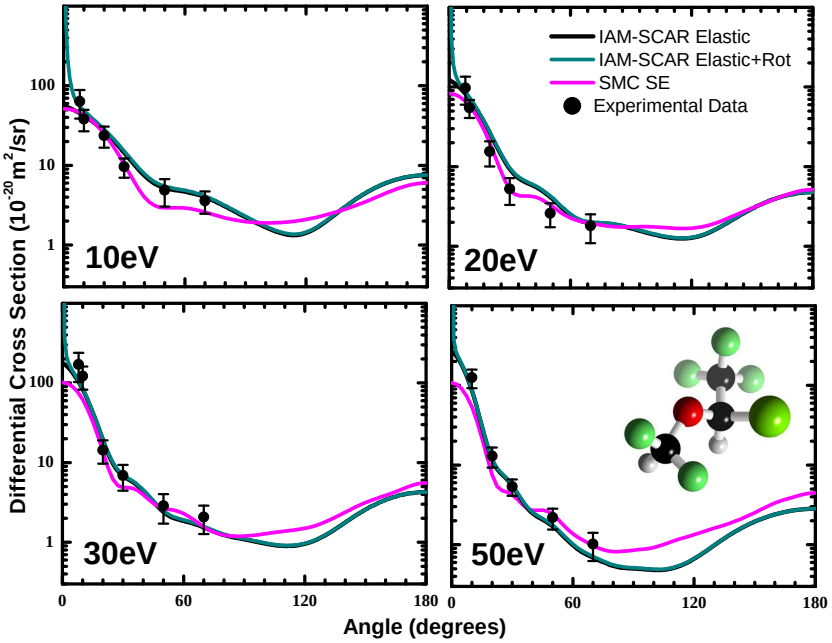

Figure 4.4: Differential cross sections (DCS) for electron scattering from isoflurane molecule in the incident electron impact energy region 10–50 eV. Calculated elastic scattering DCSs were obtained at the SMC-PP and IAM-SCAR+I levels.

The absolute scale of the experimental DCS is obtained by normalization with the IAM-SCAR+I calculation, at 30° scattering angle. Like in sevoflurane, no significant contribution of the the low-lying vibrational modes are expected in the measured elastic cross section for the isoflurane molecule [140], and any possible contribution of vibrational modes would not be resolved with the energy resolution achieved in these experiments. The experimental normalized DCSs are tabulated as numerical values in Table 4.2. The overall energy resolution of the incident electron beam was ~ 150 meV for 10 eV electron impact energy, ~ 200 meV for 20 eV, and ~ 240 meV for 30 and 50 eV electron impact energies.

The elastic differential cross sections for experimental electron scattering by isoflurane molecules are presented in Figure 4.4, and show a very good agreement with the calculated DCS obtained by both IAM-SCAR and SMC methods, for all incident electron energies measured. For 10 eV, the theoretical SMC elastic differential cross section presents a

minimum, between 40° and 50°. For the incident electron energy of 20 eV, a minimum shows up between 30° and 40°. For higher energies, 30 and 50 eV, the minimum moves to an even smaller angle, and appears between 20º and 30°, for both energies, but less pronounced. Despite such structures are neither present in the experimental data, nor in the IAM-SCAR cross section, the two theoretical models show a good agreement, especially for 20 and 30 eV electron incident energies. The cross-section from the IAM-SCAR method presents a broad minimum near 110° for all energies. In the SMC method, such structure is only observed at 50 eV, with a very subtle shape around 80°.

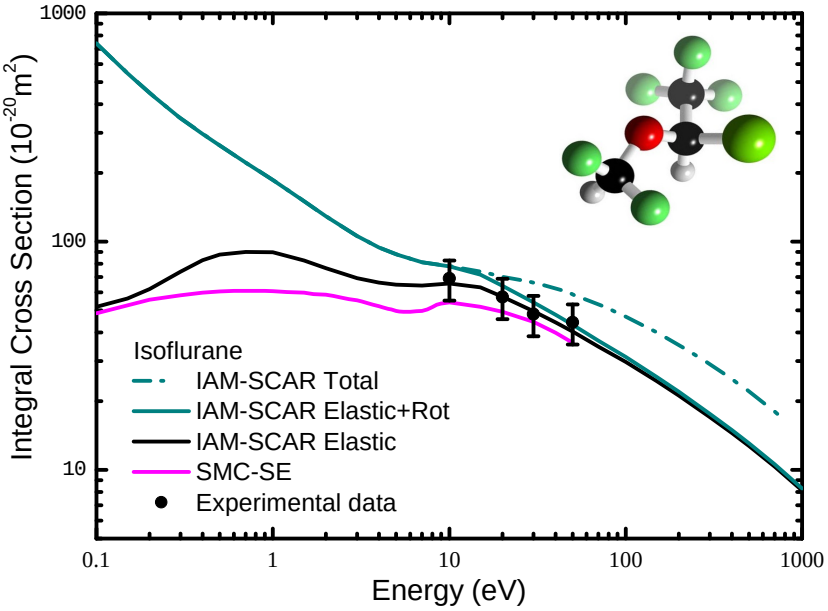

Figure 4.5: Integral cross sections ($10^{-20}m^2$) including the experimental data on electron scattering from isoflurane molecule together with the theoretical calculations using the SMC-PP and the IAM-SCAR+I methods. Also included the IAM-SCAR+I+Rot cross section.

It is worth mentioning that the DCSs calculated using the IAM-SCAR method, with and without considering the dipole interactions, labelled respectively *"Elastic+Rot"* and *"Elastic"* in Figure 4.4, are practically identical for almost the entire angular range, except for angles smaller than 10°. Due to the large dipole moment of isoflurane, this was indeed expected, since the significant increase in the forward scattering angles is a characteristic behaviour for polar molecules.

The integral cross section is shown in Figure 4.5. It is possible to observe a very good agreement between the experimental data and that obtained by the independent atom model IAM-SCAR. For low energies, the IAM-SCAR method shows a larger magnitude than the SMC cross section, yet they have a similar behaviour. The difference in magnitude between the two theoretical models is attenuated as the energy increases, and at high energies, both elastic cross sections converge. This is easily understood when one considers that the SMC method calculations were performed at the static-exchange SE approximation

Angle	10 eV	20 eV	30 eV	50 eV
8°	95.5	172.8	170.6	
10°	68.0	97.0	121.6	125.2
20°	35.2	27.4	14.3	13.0
30°	14.3	9.3	6.9	5.4
50°	7.2	4.6	2.9	2.2
70°	5.3	3.2	2.1	1.0
ICS	**68.9**	**57.2**	**48.2**	**44.3**

Table 4.2: Experimental differential and integral cross sections ($10^{-20}m^2$) for elastic scattering from isoflurane molecule. The errors on the DCSs are $23\% - 35\%$ and for the ICS are $\sim 20\%$.

level, and the effects of deformation of the target's electronic cloud due to the interaction with the incident electron was not included. This effect is quite significant in the integral cross section at low energies. We also observe in the total cross section, shown in the dotted line, that the inelastic scattering channels are opened around 11 eV of the electron incident energy, similar to sevoflurane molecule. Moreover, the isoflurane electronic state spectroscopy explored by experimental and theoretical methods is related to low-lying electronic states above 7.0 eV [138] The SMC integral cross section underestimate the one from IAM-SCAR, although it follows the same trend. At high energies both models converge.

4.5 Halothane

Halothane is an halogenated hydrocarbon that contains two heavy halogen atoms, chlorine and bromine. Its permanent dipole moment, $1.41D$ [141], is not so high in comparison with other anaesthetics studied in this work. The polarizability of halothane molecule is $\alpha = 9.37$Å [142].

The electron collision measurements were performed using a liquid sample supplied from Sigma Aldrich with a quoted purity of $\geq 99\%$ (under the name of 2-bromo-2-chloro-1,1,1-trifluoroethane and CAS number 151-67-7). The sample was degassed by repeated freeze-thaw pumped cycles.

Unlike the molecules mentioned earlier, some vibrational contributions were observed in the elastic scattering measurements performed for the halothane molecule. Distinguishable structures were observed in the elastic peak Gaussian fitting, at an incident energy of 10eV. Such contributions are corroborated by previous study of the vibrational modes of halothane [17], and were subtracted from the elastic peak in order to obtain a exclusively elastic contribution.

The experimental data of the elastic DCS of this molecule was normalized with the IAM-SCAR+I calculation, at 20° scattering angle for 10 eV and at 30° for all the other incident electron energies, in order to obtain the absolute scale. The tabulated numerical

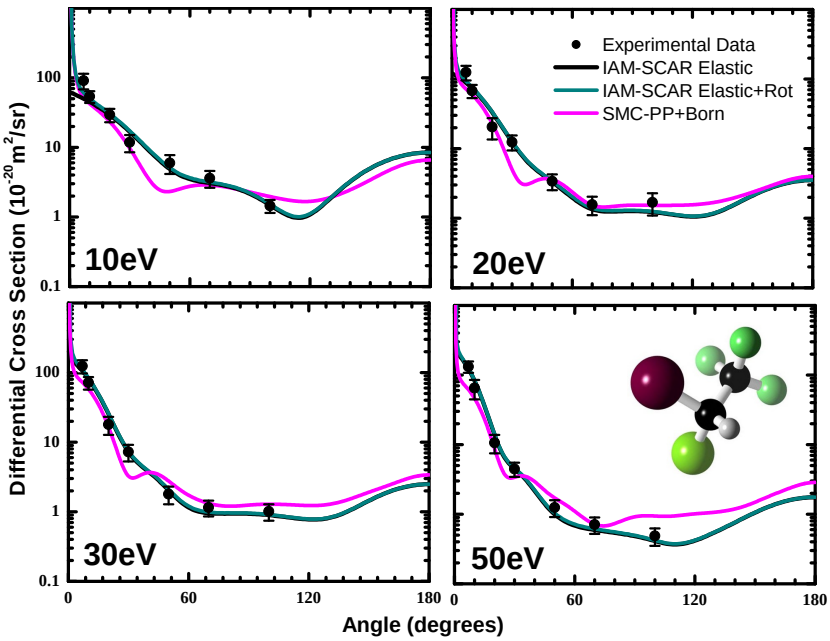

Figure 4.6: Differential cross sections (DCS) for electron scattering from halothane molecule in the incident electron impact energy region 10–50 eV. Calculated elastic scattering DCSs were obtained at the SMC-PP in the static exchange (SE) and static exchange plus polarization (SE+P) and IAM-SCAR+I levels.

values of the experimental normalized DCSs are shown in Table 4.3. The energy resolution for the measurements with halothane was ~ 180 meV for 10 eV electron impact energy and ~ 250 meV for all other electron impact energies.

A close inspection at Figure 4.6 shows that the elastic cross sections calculated by the independent atom method have a very good overlap with the experimental data. The DCS exhibits one distinct minimum at the scattering angle located between 110° and 120° for 10 eV electron incident energy. For other energies, some weak features are barely discernible. As far as SMC calculations are concerned, we also observe a reasonably good agreement especially for 20 and 30 eV, although it presents a structure that does not appear in the experimental measurements. This structure is a minimum that appears around 50° scattering angle, for 10 eV electron incident energy. For 20 and 30 eV it shows up between 30° and 40°, and for 50 eV is less prominent and appears between 20° and 30º. At 50 eV, we see a significant discrepancy for 100° scattering angle, however, as previously mentioned, it is not expected that the SMC method gives very precise description of the scattering process.

The integral cross section obtained from the experimental data in Figure 4.7, and, as in isoflurane and in sevoflurane ICSs, shows a remarkable concordance with the IAM-SCAR model. The calculations by the SMC method were performed in the static exchange plus polarization SE+P level. The polarization effect takes into account the deformation of the electronic cloud of the target molecule, due to the charge of the incident electron. This

Angle	10 eV	20 eV	30 eV	50 eV
8°	674.7	191.37	123.9	131.9
10°	53.7	67.6	71.7	53.9
20°	29.4	12.5	11.7	11.0
30°	7.5	12.4	7.2	4.5
50°	5.9	3.4	2.3	1.2
70°	3.3	1.9	1.3	0.7
100	1.4	2.1	1.2	0.7
ICS	**66.3**	**55.7**	**45.0**	**32.0**

Table 4.3: Experimental differential and integral cross sections ($10^{-20}m^2$) for elastic scattering from halothane molecule. The errors on the DCSs are $19\% - 26\%$ and for the ICS are $\sim 20\%$.

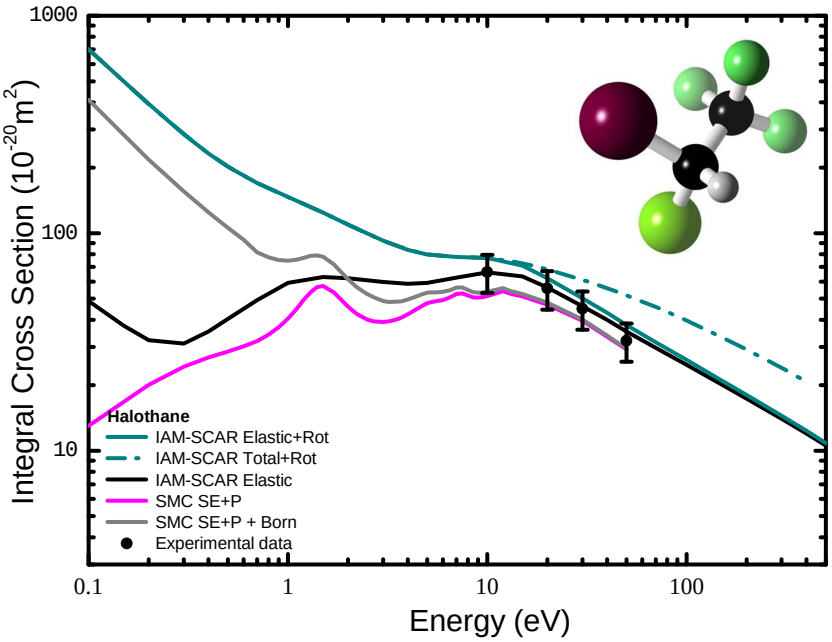

Figure 4.7: Integral cross sections ($10^{-20}m^2$) including the experimental data on electron scattering from halothane molecule together with the theoretical calculations using the SMC-PP and the IAM-SCAR+I methods. Also included the IAM-SCAR+I+Rot cross section.

effect is very relevant in very low energy collisions[4], which we can observe in the ICS. There is also the inclusion of the Born closure procedure[5], which improves the description of the long range interactions, such as permanent dipolar momentum, shown as the grey line in Figure 4.7. The ICS obtained from the Schwinger method also shows a good agreement with the experimental data, although it is slightly underestimated.

[4] As previous mentioned in section 3.4.1, at very low incident electron energy, there is a longer interaction with the target molecule, causing a significant polarization of its electronic cloud, which leads to an increase in the magnitude of the cross section.

[5] The Born closure procedure was mentioned earlier in section 3.4.1.

4.6 Discussion

The main focus of this contribution was to describe the scattering dynamics in electron collisions with anaesthetic compounds in the low- to intermediate-energy region and to validate the use of two different but complementary theoretical methods.

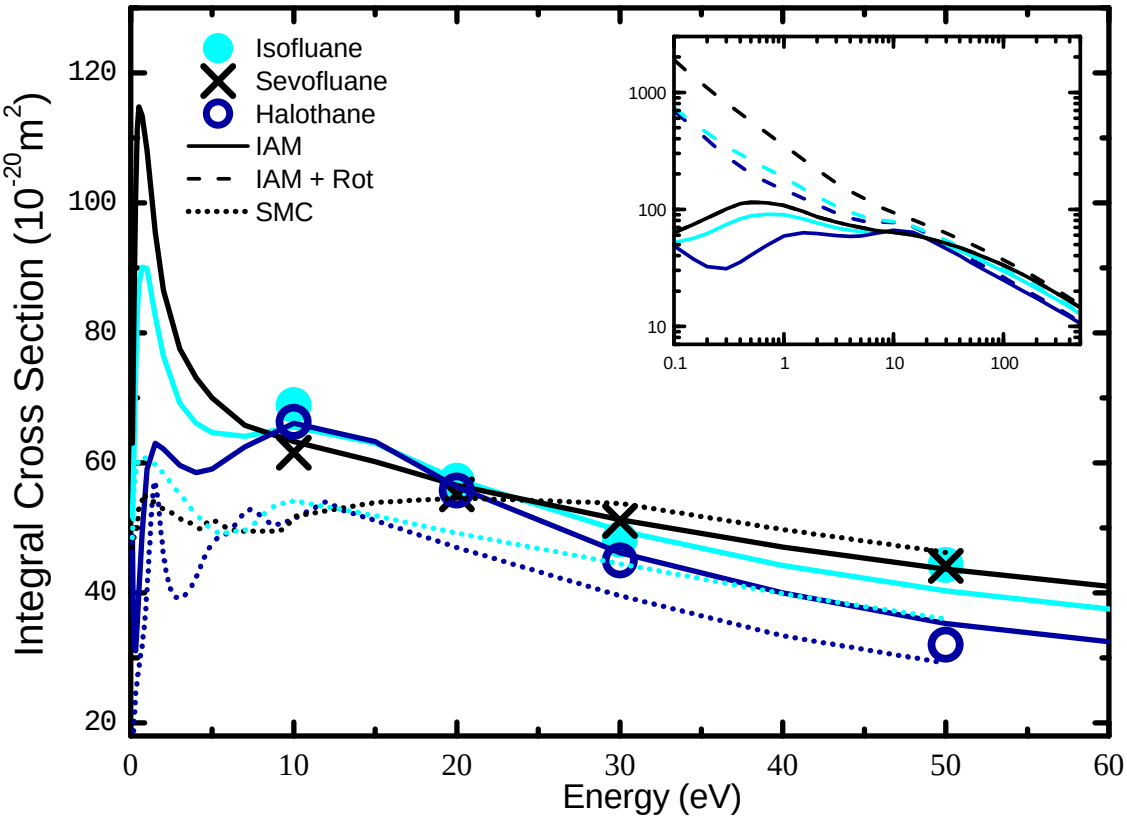

Figure 4.8: Comparative integral cross sections of isoflurane (light blue), sevoflurane (black) and halothane (dark blue) molecules, theoretical and experimental (circles and "X"). The dotted lines shows the SMC calculations. The dashed lines shows elastic scattering with the inclusion of rotational effects (in the small frame), while the straight line is without such effect, both from IAM-SCAR+I method.

In Figure 4.8 we show a comparison between the integral electron scattering cross sections for the three molecules studied in this work, sevoflurane (black), isoflurane (light blue) and halothane (dark blue). The solid line shows the IAM-SCAR+I calculations for the three molecules, while the ICS obtained from SMC are presented as a dotted line. It is possible to observe that, although the Schwinger data are underestimated, the same tendency between the three different molecules, observed on the IAM-SCAR data, is preserved: sevoflurane being the one with the greatest magnitude and halothane having the smallest in both methods. It can be noted that at 10eV the calculated ICSs for the three molecules follow the same trend. The dashed line in the inset shows the elastic scattering with the inclusion of rotational effects, while the solid line is without such effect, both from the IAM-SCAR calculations.

The experimental data also shows a good agreement for the three molecules at 10, 20 and 30 eV. For 50 eV, isoflurane and sevoflurane experimental ICSs are in perfect coincidence, while for halothane the magnitude is about 30% lower.

As far as these molecules are concerned, we have presented for the first time a joint experimental and theoretical investigation on the elastic differential cross sections. Below 20 eV electron impact, these results have shown a reasonable agreement between our experimental data and the SMC-PP method whereas above this energy the IAM-SCAR+I method describes very well the experimental findings. Also interesting to note is the excellent agreement of the IAM-SCAR+I calculation, including rotational excitations, to describe below 20 eV the asymptotic behaviour of the experimental DCS in the forward direction. Finally, for the entire energy region investigated, 10 - 50 eV, the methodology implemented shows the relevance of combining both theoretical methods to help describing the experimental finds.

Chapter

5 Results: Electronic State Spectroscopy of key Selected Anaesthetics Molecules

"We are not to tell nature what she's gotta be... She's always got better imagination than we have.
— Richard P. Feynman, Photons: Corpuscles of Light

In this chapter we report results on the electronic state spectroscopy of isoflurane and sevoflurane molecules by high resolution photoabsorption spectroscopy and comprehensive *ab initio* theoretical calculations on the lowest-lying valence (singlet and triplet), Rydberg and ionisation states. Our results are discussed with a comparison with other data, where available, including photoabsorption studies of halothane, previously explored at LCAM, together with the photolysis rates of these molecules calculated from 0 to 50 km altitude in the Earth's atmosphere.

Photoabsorption spectra were recorded using the UV beam line of the ASTRID2 synchrotron facility at Aarhus University, Denmark over the photon range of 5.0–10.8 eV. The experimental apparatus has been described in section 3.2. *Ab initio* calculations were performed within the Gaussian 09 package [122]. The ground-state geometries were optimized at the $DFT/LC{-}\omega PBE$ level [120, 121] [19]. For H, C, F, O and Cl, a Dunning's aug-cc-pVTZ basis set was used [123, 143]. The electronic spectra were calculated at the $TD-DFT/LC-\omega PBE/aug-cc-pVTZ$ level, using an extended basis set consisting of a (5s5p2d) set of Rydberg orbitals located at the mass centre of the molecule (aug-cc-pVTZ+R basis set). The exponents were obtained using the method proposed by Kaufmann et al. [124]. The oscillator strengths were obtained using the length gauge. The lowest vertical ionization energies were obtained from Koopmans' theorem and also with the Partial Third Order (P3) at the $LC-\omega PBE/aug-cc-pVTZ$ geometries [144] and Outer Valence Greens Function (OVGF) [145] propagator methods.

A literature survey reveals a UV absorption spectrum of anaesthetics in the range 200–350nm (6.20–3.54eV) by Langbein et al.[9] in order to obtain the atmospheric lifetimes of these compounds, however they state that "*all three anaesthetics had substantial UV absorption only below 250 nm*", it is not shown the absorption spectrum for sevoflurane, and for isoflurane the spectrum is presented only in the 200-230 nm range, which does not overlap the range investigated in our work, making a comparison impossible. A vibrational assignment of sevoflurane, $(CF_3)_2CHOCH_2F$ reported by Dom et al. [12] and non-linear Raman spectroscopy of sevoflurane and isoflurane by Nagashima and co-workers [13]. As far as molecular structures of isoflurane and sevoflurane are concerned, *ab initio* methods have been used by Lesarri et al. [10], Ren and Li [9] and Tang et al. [14]. Finally we note experiments on negative ion formation through dissociative electron attachment to isoflurane and enflurane by Matias et al. [15].

5.1 Sevoflurane

5.1.1 Eletronic structure of sevoflurane

From the present *ab initio* calculations at the $LC-\omega PBE/aug-cc-pVTZ$ level, sevoflurane has C_1 symmetry in its electronic ground state and the calculated electron configuration of the outermost valence orbitals of the $\tilde{X}^1A$ ground state is: ... $44a^2$ $45a^2$ $46a^2$ $47a^2$ $48a^2$ $49a^2$.

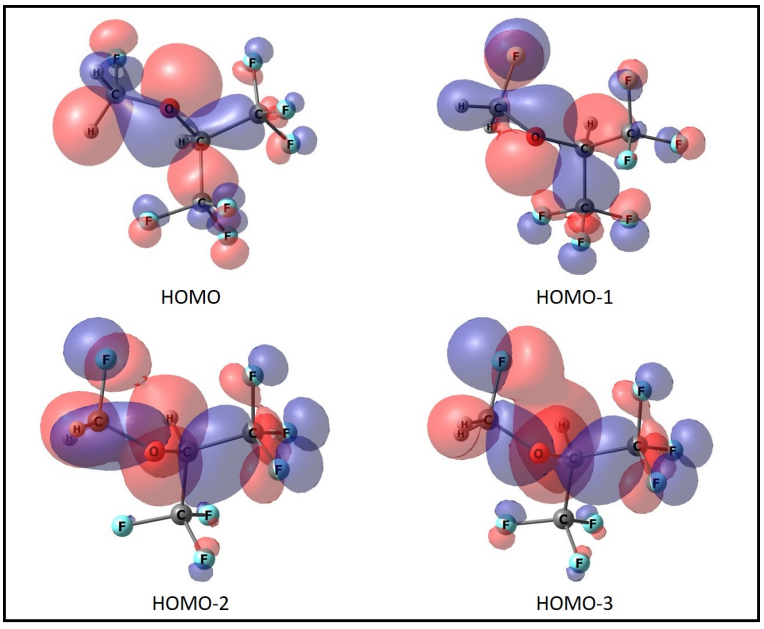

Figure 5.1: Representation of the four highest occupied molecular orbital (HOMOs) of sevoflurane, obtained by LC-ωPBE/aug-cc-pVTZ calculations using Gaussian 09 [122] and visualized using Chemcraft software [146].

Examination of the ground-state molecular orbitals (MOs), in Figure 5.1, shows that the highest occupied molecular orbital (HOMO), 49a, the second highest occupied molecular

orbital (HOMO-1), 48a, and the third highest occupied molecular orbital (HOMO-2), 47a, have mainly O lone pair character. We can anticipate that promotion of n_O electrons will result in the absence of vibrational excitation features since these do not participate in $C-O$ bonding. The lowest unoccupied molecular orbital (LUMO), 50a, is mixed $3s/\sigma^*$ character and the second lowest unoccupied molecular orbital (LUMO+1), 51a, is of antibonding valence character $\sigma^*(C-O)$, where the present theoretical studies have shown considerable overlap of the lowest Rydberg states with valence states mainly involving the $C-O$ bond.

5.1.2 Electronic excitation of sevoflurane

Figure 5.2 shows the VUV photoabsorption spectrum of sevoflurane ($C_4H_3F_7O$) in the 5.0–10.8 eV photon energy range. The calculated transition energies, oscillator strengths, and the main character of the wave function are shown in Table 5.1 for singlet and triplet states (TD-DFT results). A close inspection of this table reveals a reasonably good agreement between experiment and theory, within ±0.5eV, which is reasonable given the level of accuracy of the calculations. Some members of the Rydberg series are tentatively assigned for the first time with the help of the calculated vertical ionisation energys (IEs) at different levels of theory, presented in Table 5.2. The lowest energy 12.275 eV $(49a)^{-1}$ has been used to calculate the quantum defects associated with transitions to Rydberg orbitals.

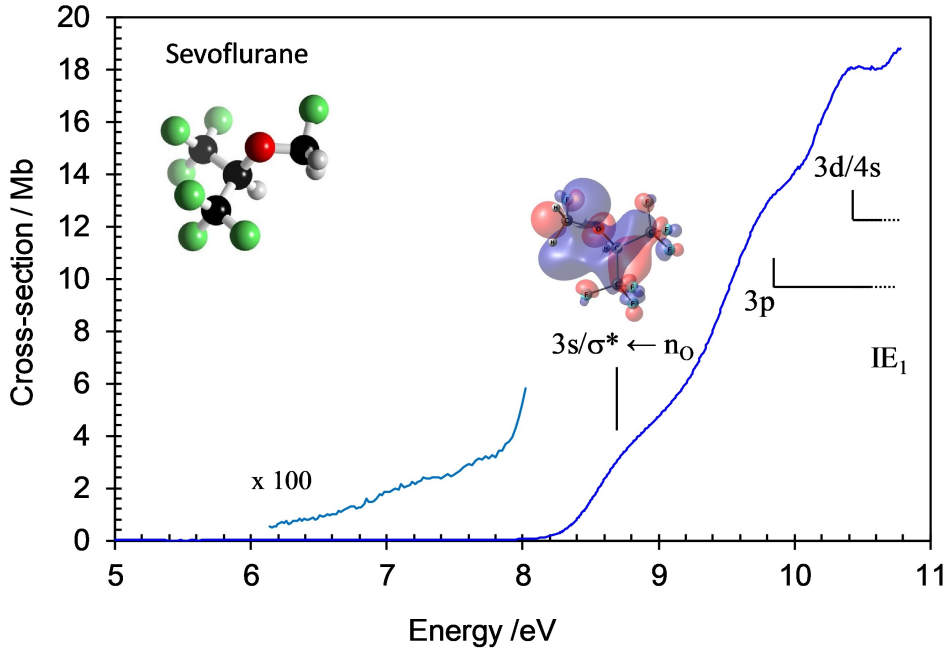

Figure 5.2: VUV photoabsorption cross-section of sevoflurane.

The major photoabsorption band of sevoflurane is classified mainly as valence transitions of $^1(\sigma^* \leftarrow n_O)$ character and members of Rydberg series converging to the lowest ionisation energies. We now discuss the valence and Rydberg excitation of sevoflurane highlighting the most relevant features assigned with the help of theoretical calculations.

5.1.2.1 Valence singlet excitation of sevoflurane

Some of the excited states of sevoflurane were assigned as valence/Rydberg mixed character, but most of them as Rydberg orbitals, as shown in Table 5.1. The photoabsorption spectrum of sevoflurane in Figure 5.2 shows that the lowest-lying singlet electronic state has a vertical value at 8.87(5) eV (4.1 Mb), which is in reasonably good agreement with the calculation result of 9.1794eV. Here this transition is assigned to $3^1A \leftarrow \tilde{X}^1A$, ($3s/\sigma^* \leftarrow n_O$, 49a) with a calculated oscillator strength $f_L = 0.012$. The other two major broad bands centred at 9.85(6) and 10.43(6) eV, with local cross-section values of 13.3 and 18.1 Mb, can be classified mainly as Rydberg transitions due to the promotion of an electron from the HOMO (49a) to *3p* and *3d* unoccupied MOs, and will be discussed latter. The representation of all molecular orbitals of the electronic transitions are shown in appendix B.

5.1.2.2 Valence triplet excitation of sevoflurane

As far as we are aware, these are the first set of theoretical calculations on the lowest-lying triplet states of sevoflurane presented in blue in Table 5.1. Although the VUV photo-absorption data shown in Figure 5.2 is related to optically allowed transitions, the particularly low intensities observed at 8 eV may be related to optically forbidden transitions. We note that in these energy regions the poor signal-to-noise ratio due to the considerable low cross-section values (< 0.1 Mb) in the present experiments make it difficult to obtain smoother VUV profiles.

The theoretical calculations in Table 5.1 report the sevoflurane lowest valence/Rydberg triplet transition energies calculated at the $TD-DFT/LC-\omega PBE/aug-cc-pVTZ+R$ level. The lowest lying electronic state at 8.757 eV is assigned to the $1^3A \leftarrow \tilde{X}^1A$, ($3s/\sigma^* n_O$, 49a) transition but is $1.5eV$ above the weakest feature at 7.230 eV. Unfortunately we are not aware of any available data in the literature to compare with.

			Assignment				
Transition	E(eV)	f_L	HOMO (49a)	HOMO-1 (48a)	HOMO-2 (47a)	HOMO-3 (46a)	E(eV) Exp.
$\tilde{X}^1A$							
1^3A	8.7571	0.0000	$3s/\sigma^*$				
2^3A	9.0856	0.0000	$3p$				
3^1A	9.1794	0.0120	$3s/\sigma^*$				$8.87(5)^{(s)}$
4^3A	9.4494	0.0000	$3p$				
5^1A	9.5738	0.0037	$3p$				
6^3A	9.6397	0.0000	$3p$	$3s/\sigma^*$			
7^1A	9.6660	0.0119	$3p$				
8^3A	9.7464	0.0000	$3p$				
9^3A	9.8204	0.0000	$3d$				
10^1A	9.9027	0.0081	$3p$	$3s/\sigma^*$			
11^1A	10.011	0.0258	$3p$				$9.85(6)^{(s)}$
12^3A	10.055	0.0000		$3p$			
13^3A	10.195	0.0000	$3d$				
14^1A	10.221	0.0165	$3d$	$3p$			
15^1A	10.347	0.0050	$3p$	$3p$			
16^3A	10.423	0.0000		$3p$		$3s/\sigma^*$	
17^3A	10.457	0.0000	$4s$				
18^3A	10.545	0.0000	$3d$	$3d$			
19^1A	10.557	0.0165	$3p$				
20^3A	10.615	0.0000	$3d$		σ^*		
21^1A	10.647	0.0254	$3d$				$10.43^{(s)}$
22^3A	10.647	0.0000	$3d$			$3s/\sigma^*$	
23^1A	10.678	0.0070	$3d$	$3p$			
24^3A	10.745	0.0000	$3d$			$3s/\sigma^*$	
25^1A	10.792	0.0247	$3d$				$10.43^{(s)}$
26^3A	10.824	0.0000	$4p$				
27^1A	10.831	0.0035	$3d$			$3s/\sigma^*$	
28^1A	10.866	0.0085	$3d$				

Table 5.1: Calculated vertical excitation energies ($TD-DFT/LC-\omega PBE/aug-cc-pVTZ+R$) and oscillator strengths of sevoflurane ($C_3H_2ClF_5O$) compared with experimental data.The singlet transitions are show in black, while the triplet transitions are shown in blue. $^{(s)}$ indicates shoulder structure (the last decimal of energy value is given in brackets for these less resolved features).

5.1.2.3 Ionisation energies of sevoflurane

Table 5.2 presents the calculated vertical ionisation energies (IEs) for sevoflurane at different levels of theory where intensities have been obtained with the $LC-\omega PBE/aug-cc-pVTZ$ geometry. A general overview of the tabulated values reveal that all the theoretical methods agree reasonably well with each other with the exception of Koopmans' theorem. Such discrepancy is not surprising in view of the improper electron correlation (and relaxation) treatment in the Koopmans' theorem. We are not aware of any experimental ionisation energies to compare with our calculations. However, our experience with several other molecular targets, in particular for the anaesthetic halothane [147] and more recently in the case of the XF_4 (X=C, Si and Ge) molecules [29,30], reveals that the P3 and OVGF results are very close to each other and reproduce the experimental data reasonably well, to within 0.6 eV. In order to assign the sevoflurane lowest lying Rydberg members converging to the ionic electronic ground state only, we have used the vertical IE value of 12.275 eV (Table 5.2).

Orbital	Koopmans'	OVGF		P3		P3+	
	E(eV)	E(eV)	PS	E(eV)	PS	E(eV)	PS
$31a^{-1}$	20.991	19.034	0.907	19.022	0.902	18.828	0.896
$32a^{-1}$	20.503	18.666	0.908	18.565	0.904	18.378	0.898
$33a^{-1}$	20.201	18.122	0.910	17.980	0.907	17.777	0.900
$34a^{-1}$	19.985	17.833	0.910	17.684	0.907	17.474	0.901
$35a^{-1}$	19.815	17.837	0.910	17.754	0.905	17.568	0.900
$36a^{-1}$	19.727	17.579	0.910	17.431	0.906	17.220	0.900
$37a^{-1}$	19.640	17.483	0.910	17.334	0.906	17.120	0.900
$38a^{-1}$	18.857	16.803	0.912	16.661	0.907	16.454	0.902
$39a^{-1}$	18.768	16.681	0.911	16.535	0.907	16.326	0.901
$40a^{-1}$	18.484	16.376	0.911	16.212	0.907	16.001	0.901
$41a^{-1}$	18.419	16.338	0.911	16.181	0.907	15.971	0.901
$42a^{-1}$	18.316	16.079	0.910	15.897	0.907	15.676	0.901
$43a^{-1}$	18.085	15.862	0.910	15.662	0.907	15.442	0.901
$44a^{-1}$	17.604	15.623	0.908	15.588	0.903	15.373	0.897
$45a^{-1}$	17.280	15.355	0.910	15.328	0.905	15.136	0.900
$46a^{-1}$	16.901	15.128	0.911	15.228	0.904	15.068	0.900
$47a^{-1}$	15.614	14.160	0.914	14.286	0.909	14.167	0.906
$48a^{-1}$	14.814	13.427	0.913	13.406	0.910	13.268	0.906
$49a^{-1}$	13.867	12.275	0.910	12.375	0.906	12.219	0.901

Table 5.2: Vertical ionization energies and intensities (pole strengths PS) of sevoflurane molecule, obtained from Koopmans' theorem and also with the Partial Third Order (P3) at the LC-ωPBE/aug-cc-pVTZ geometries [144] and Outer Valence Greens Function (OVGF) [148] propagator methods.

5.1.2.4 Rydberg excitation of sevoflurane

The peak positions, E_n, in the photoabsorption spectra consisting of structures superimposed on diffuse features extending to the lowest ionisation energies (IEs), have been compared using the Rydberg formula

$$E_n = E_i - \frac{R}{(n-\delta)^2} \tag{5.1}$$

where E_i is the ionisation energy, n is the principal quantum number of the Rydberg orbital of energy E_n, R is the Rydberg energy constant (13.61 eV), and δ the quantum defect resulting from the penetration of the Rydberg orbital into the core. The first members of the Rydberg features in the spectra are proposed with the quantum defect calculations as our only guide, so the values in Table 5.3 are just tentative assignments. Higher members of the Rydberg series, where $n \geqslant 4$ members are expected to lie, were not attempted since these features are beyond the energy region investigated. The identification of Rydberg states was based more firmly on the symmetry and shape of the single occupied orbitals and the values of the oscillator strengths (Table 5.1).

For the members of the Rydberg series converging to the ionic electronic ground state, we have assigned $3s$, $4s$, $3p$ and $4d$ features at 8.87(5), 10.43(6), 9.85(6) and 10.43(6) eV with quantum defects 1.00, 0.97, 0.63 and 0.28. Note that the 8.87(5) eV feature has mixed valence/ Rydberg character, $3s/\sigma^* \leftarrow 49a$, although the rather broad nature of the band correlates to the dissociative σ^* character of the $3s$ orbital.

Vertical energy	δ	Assignment
		(49a) $\rightarrow ns(a)$
8.87(5)$^{(s)}$	1.00	3s
10.43(6)$^{(b)}$	0.97	4s
		(49a) $\rightarrow np(a)$
9.85(6)$^{(s)}$	0.63	3p
		(49a) $\rightarrow nd(a)$
10.43(6)$^{(b)}$	0.28	3d

Table 5.3: Energies[1] (eV), quantum defects (δ), and assignments of the ns, np and nd Rydberg series converging to the ionic electronic ground state $(49a)^{-1}$, with $IE_1 = 12.275eV$.
$^{(s)}$ means a shoulder;
$^{(b)}$ means a broad feature.

[1] The last decimal of energy value is given in brackets for these less revolved features.

5.2 Isoflurane

5.2.1 Electronic structure of isoflurane

Sevoflurane ($C_4H_3F_7O$) and isoflurane ($C_3H_2ClF_5O$) molecules, represented in 5.3, are very similar, the main difference is the presence of a chlorine atom in the later, as a substitute of the CF_3 group in the former. Thus, it is not surprising that its electronic states have several resemblances. Like sevoflurane molecule, isoflurane also has C_1 symmetry and, from de calculations at the $LC-\omega PBE$ level, the outermost valence orbitals of the $\tilde{X}^1A$ ground state is: ... $40a^2$ $41a^2$ $42a^2$ $43a^2$ $44a^2$ $45a^2$.

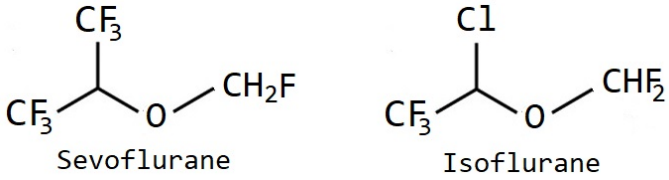

Figure 5.3: Representation of the sevoflurane (left) and isoflurane (right) formulas.

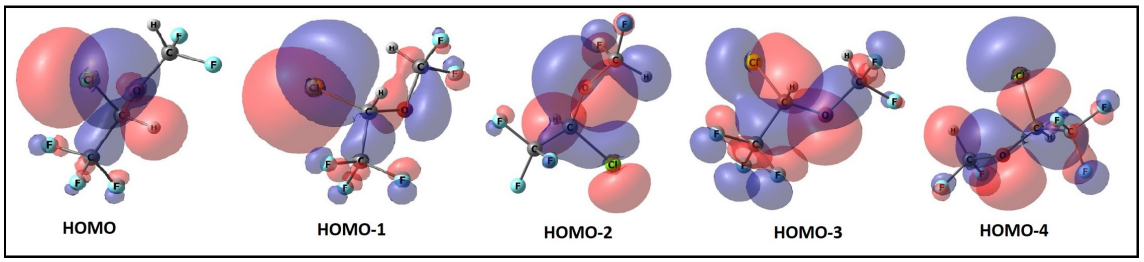

Figure 5.4: Representation of the five highest occupied molecular orbital (HOMOs) of isoflurane molecule, obtained by LC-ωPBE/aug-cc-pVTZ calculations using Gaussian 09 package [122] and visualized using Chemcraft software [146].

The ground-state MOs, in Figure 5.4, show that in the case of isoflurane the highest occupied molecular orbital (HOMO), 45a, and the second highest (HOMO-1), 44a, have Cl lone pair character, and the third highest occupied molecular orbital (HOMO-2), 43a, has O lone pair character. Promotion of n_{Cl} electrons will result in the absence of vibrational excitation features, because these do not participate in $C-Cl$ bonding. As far as the lowest unoccupied molecular orbitals are concerned, for isoflurane the (LUMO), 46a, is mainly $\sigma^*(C-Cl)$ and the (LUMO+1), 47a, of $\sigma^*(C-O)$ antibonding character. In the same way as for sevoflurane, a considerable overlap of the lowest Rydberg states with valence states mainly involving the $C-O$ bond are shown in the present theoretical calculations. The calculated transition energies, oscillator strengths, and the main character of the wave function is shown in Table 5.4 for singlet and triplet states and the calculated vertical IEs are presented in Table 5.5 and the lowest ionisation energy at 12.316 eV $(45a)^{-1}$ have been used to calculate isoflurane quantum defects associated with transitions to Rydberg orbitals.

			Assignment					
	E(eV)	f_L	HOMO (45a)	HOMO-1 (44a)	HOMO-2 (43a)	HOMO-3 (42a)	HOMO-4 (41a)	E(eV) Exp
$\tilde{X}^1A$								
1^3A	6.6963	0.0000	$\sigma^*(C-Cl)$					
2^3A	6.9288	0.0000		$\sigma^*(C-Cl)$				
3^1A	7.6293	0.0006	$\sigma^*(C-Cl)$					
4^1A	7.9194	0.0034		$\sigma^*(C-Cl)$				$7.64(4)^{(s)}$
5^3A	8.0999	0.0000					$\sigma^*(C-Cl)$	
6^3A	8.4813	0.0000			$\sigma^*(C-O)$			
7^3A	9.0130	0.0000	$3s/\sigma^*(C-H)$					
8^1A	9.0922	0.0614					$\sigma^*(C-Cl)$	9.096
9^3A	9.1784	0.0000	$\sigma^*(C-O)$					
10^1A	9.2933	0.0256	$3s/\sigma^*(C-H)$					
11^1A	9.3555	0.0465					$\sigma^*(C-O)$	
12^3A	9.3858	0.0000	$3s/\sigma^*(C-Cl)$					
13^1A	9.5755	0.0563		$3s/\sigma^*(C-Cl)$				$9.096/9.59(6)^{(b)}$
14^3A	9.5975	0.0000	$\sigma^*(C-O)$			$\sigma^*(C-Cl)$		
15^3A	9.6730	0.0000		$3s/\sigma^*$	$3s/\sigma^*(C-O)$			
16^3A	9.7370	0.0000	$\sigma^*(C-O)$					
17^1A	9.7402	0.0078	$\sigma^*(C-O)$					
18^3A	9.8291	0.0000					$3s/\sigma^*$	
19^3A	9.9470	0.0000	$3p$					
20^1A	9.9483	0.0094					$3s/\sigma^*(C-O)$	
21^1A	10.0755	0.0162		$3s/\sigma^*$	$3s/\sigma^*$			
22^1A	10.1734	0.o367		$3p$				$9.74(0)^{(s)}$
23^3A	10.1840	0.0000			$\sigma^*(C-O)$			
24^3A	10.2712	0.0000		$3p/\sigma^*(C-H)$				
25^1A	10.2852	0.0010			$\sigma^*(C-O)$			
26^1A	10.3157				$3p\sigma^*(C-O)$			10.105
27^3A	10.3474	0.0000	$3p$					
28^3A	10.3551	0.0000				$3p$		

Table 5.4: Natural transition orbitals (NTO) of isoflurane molecule, calculated using Gaussian 09 package [122].The singlet transitions are show in black, while the triplet transitions are shown in blue.
$^{(s)}$ indicates shoulder structure (the last decimal of energy value is given in brackets for these less resolved features).
$^{(b)}$ indicates broad feature (the last decimal of energy value is given in brackets for these less resolved features).

5.2.2 Electronic excitation of isoflurane

The VUV photoabsorption spectrum of isoflurane ($C_3H_2ClF_5O$) is shown in Figure 5.5 and the calculated vertical excitation energies and oscillator strengths (singlet and triplet states) are presented in Table 5.4, in which it is possible to observe a good agreement between experiment and theory, with the same level of accuracy as shown for sevoflurane. The representation of all the molecular orbitals of corresponding to the electronic transitions are shown in appendix C. This is the first assignments for some members of the Rydberg series, with the help of the calculated vertical ionisation energies (IEs) at different levels of theory.

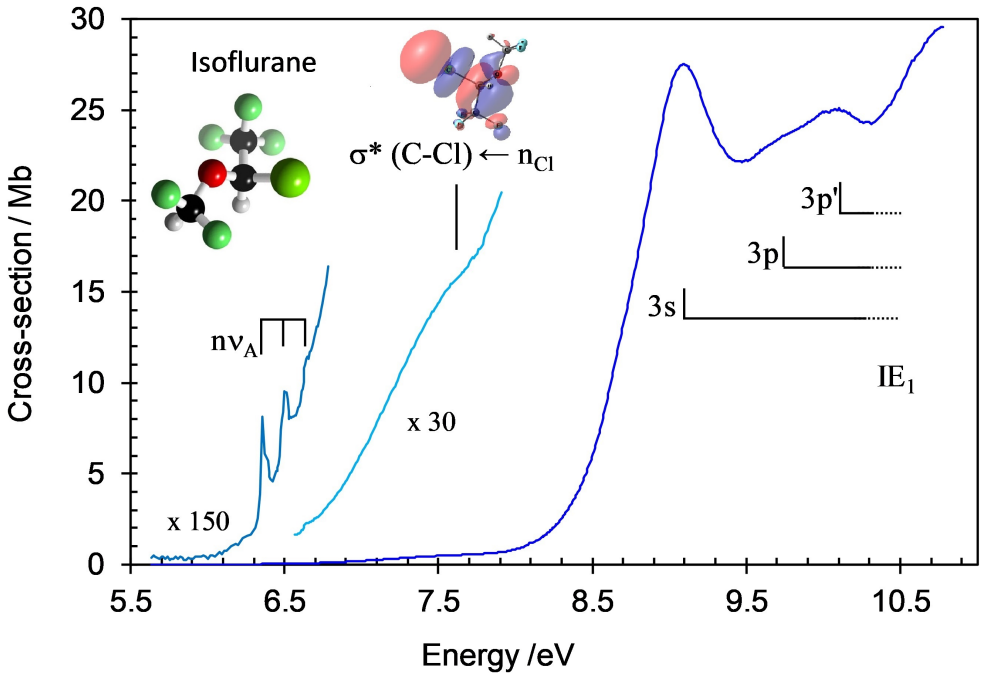

Figure 5.5: VUV photoabsorption cross section of isoflurane molecule.

For isoflurane, the major photoabsorption band is classified as valence transitions of $^1(\sigma^* \leftarrow n_{Cl})$ character. In fact, by carefully observing the Table 5.4, it can be observed that the vast majority of the transitions are to orbitals that have exclusive valence character, with only a few transitions to the Rydberg or mixed character orbitals. The broad and structureless nature of the VUV features may be indicative of dissociative-like character of the valence transitions, which is not surprising since the electronic excitation is mainly restricted to the promotion of chlorine lone pair electrons to σ^* antibonding orbitals. Additionally, we note in the photoabsorption profiles in Figure 5.5 the contribution of an underlying signal above $8.5eV$ which may be related to dissociative and/or pre-dissociative states contributing to a shift upwards from the base line of the VUV spectra. It is interesting to note that previous comprehensive description of the anaesthetic halothane ($CF_3CHBrCl$) electronic state spectroscopy [147] such behaviour has also been reported, although at slightly lower excitation energy ($7eV$).

5.2.2.1 Valence singlet excitation of isoflurane

Figure 5.5 shows isoflurane photoabsorption spectra in the 5.5–10.8 eV range, where several broad bands have been assigned to transitions from occupied molecular orbitals to valence and/or Rydberg orbitals, as listed in Table 5.4. The lowest-lying excited state at 7.64(4) eV (0.5 Mb) is assigned to the $4^1A \leftarrow \tilde{X}^1A$ ($\sigma^*(C-Cl)$, 44a) transition according to the theoretical calculation. The second absorption band with the most prominent feature in the VUV spectrum at 9.096 eV and a local cross-section of 27.5 Mb, is assigned to a $(\sigma^*(C-Cl) \leftarrow 41a)$ transition. Other weak features in the VUV spectrum are barely visible at 9.59(6), 9.74(0) and 10.105 eV and are tentatively assigned to $(3s/\sigma^*(C-Cl) \leftarrow 44a)$, $(3p \leftarrow 44a)$ and $(3p/\sigma^*(C-O) \leftarrow 43a)$ transitions respectively, where the Rydberg character will be discussed in section 5.2.2.4. Note that the $(3s/\sigma^*(C-Cl) \leftarrow 44a)$ transition has a calculated oscillator strength (~ 0.06) similar to the most intense transition at 9.096 eV and a term value of 2.72 eV which is too low for a Rydberg excitation. Thus this transition is assigned mainly of valence character.

5.2.2.2 Valence triplet excitation of isoflurane

As for sevoflurane, we are not aware of any previous theoretical calculations on the lowest-lying triplet states of isoflurane.

A close inspection of the MOs, in Figure 5.4, reveals that the HOMO (45a) also shows some $\sigma(C-C)$ character while the HOMO-1 (44a) has some $\sigma(C-O)$ character. The lowest valence triplet transition energy calculated at the $TD-DFT/LC-\omega PBE/aug-cc-pVTZ+R$ level assigns the features at 6.696 eV to $1^3A \leftarrow \tilde{X}^1A$, $(\sigma^*(C-Cl) \leftarrow n_{Cl}, 45a)$ and at 6.929 eV to $2^3A \leftarrow \tilde{X}^1A$, $(\sigma^*(C-Cl) \leftarrow n_{Cl}, 44a)$ (Table 5.4). However, the cross-section in the low photon energy of Figure 5.5 reveals three features at 6.358, 6.498 and 6.65(9) eV with an average energy spacing of 0.151 eV ($1220cm^{-1}$). The origin of the band, ν_{0-0}, is tentatively assigned to be 6.358 eV. The infrared spectrum of isoflurane has been reported by Andersen and co-workers [149] where intense absorption features are observed between 1100 and $1250cm^{-1}$. Although the authors do not give any assignments for those peaks, the fine structure energy spacing in the VUV spectrum is tentatively assigned to ν_A corresponding to the $C-O$ stretching mode from the ground state frequency of acetic acid 0.147 eV ($1182cm^{-1}$) [150]. Due to the considerable similarity in the $C-O-C$ geometry between isoflurane and sevoflurane, such an assumption seems reasonable since the work of Andersen et al. [11] for products of chlorine atom initiated oxidation of sevoflurane reveal an infrared feature at $1123cm^{-1}$ assigned to the $\nu(C-O)$ stretching mode. Another possibility is contamination in the sample during the measurements.

5.2.2.3 Ionisation energies of isoflurane

The vertical ionisation energies (IEs) of isoflurane are presented in Table 5.5 at different levels of theory where intensities have been obtained with the $LC{-}\omega PBE/aug{-}cc{-}pVTZ$ geometry. Alike with sevoflurane, the IEs of isoflurane obtained though OVGF, P3 and P3+ methods agree very well with each other, only the Koopmans' theorem shows some discrepancy, for the reason mentioned above. We are not aware of any experimental ionisation energies to compare with our calculations. The first vertical IE value of 12.316 eV was used in order to assign the lowest lying Rydberg members converging to the ionic electronic ground state.

Orbital	Koopmans'	OVGF		P3		P3+	
	E(eV)	E(eV)	PS	E(eV)	PS	E(eV)	PS
$31a^{-1}$	20.007	17.830	0.907	17.673	0.904	17.457	0.897
$32a^{-1}$	19.923	17.728	0.908	17.554	0.905	17.331	0.899
$33a^{-1}$	19.184	17.104	0.908	16.915	0.905	16.697	0.898
$34a^{-1}$	18.943	16.935	0.907	16.826	0.903	16.614	0.897
$35a^{-1}$	18.845	16.905	0.909	16.798	0.904	16.601	0.899
$36a^{-1}$	18.588	16.520	0.909	16.374	0.905	16.162	0.899
$37a^{-1}$	18.350	16.300	0.907	16.212	0.902	16.007	0.897
$38a^{-1}$	18.236	16.011	0.909	15.801	0.906	15.575	0.899
$39a^{-1}$	18.149	16.186	0.909	16.028	0.905	15.817	0.899
$40a^{-1}$	17.553	15.666	0.905	15.728	0.899	15.535	0.894
$41a^{-1}$	16.569	15.060	0.914	15.176	0.907	15.057	0.904
$42a^{-1}$	15.828	14.230	0.906	14.261	0.902	14.094	0.897
$43a^{-1}$	14.377	12.970	0.907	13.082	0.903	12.945	0.899
$44a^{-1}$	13.481	12.595	0.907	12.541	0.903	12.514	0.902
$45a^{-1}$	13.182	12.316	0.910	12.301	0.906	12.276	0.905

Table 5.5: Vertical ionization energies and intensities (pole strengths PS) of isoflurane molecule, obtained from Koopmans' theorem and also with the Partial Third Order (P3) at the LC-ωPBE/aug-cc-pVTZ geometries [144] and Outer Valence Greens Function (OVGF) [148] propagator methods.

5.2.2.4 Rydberg excitation of isoflurane

In the same way as in section 5.1.2.4, the values in Table 5.6 are just tentative assignments, since the first members of the Rydberg features in the spectra are proposed with the quantum defect calculations as our only guide. The identification of Rydberg states was based more firmly on the symmetry and shape of the single occupied orbitals and the values of the oscillator strengths. Unlike for sevoflurane, there are only few Rydberg orbitals within the first low-lying excited states of isoflurane, and most of them have a mixed valence character, as shown in Table 5.4. The feature at 9.59(6) eV in the VUV photoabsorption spectrum of isoflurane (Figure 5.5) is mainly valence in character, $\sigma^*(C-Cl) \leftarrow 44a$, but could have a Rydberg character as predicted by the calculations and assigned to the

$3s \leftarrow 44a$ transition, although with a low quantum defect ($\delta = 0.76$) for an ns series. However the feature at 9.096 eV fits much better a *3s* Rydberg member with a quantum defect $\delta = 0.94$. The other lowest-lying members of the *np* and *np'* series are assigned at 9.74(0) and 10.105 eV with $\delta = 0.70$ and $\delta = 0.52$.

Vertical energy	δ	Assignment
		(44a) $\rightarrow ns(a)$
9.096	0.94	3s
		(44a) $\rightarrow np(a)$
$9.74(0)^{(s)}$	0.70	3p
		(49a) $\rightarrow np'(a)$
10.105	0.52	3p'

Table 5.6: Energies[2] (eV), quantum defects (δ), and assignments of the ns, np and nd Rydberg series converging to the ionic electronic ground state $(45a)^{-1}$, with $IE_1 = 12.316eV$, of isoflurane.
$^{(s)}$ means a shoulder.

5.3 Discussion

The absolute cross-sections can be used in combination with solar actinic flux, measured as a function of wavelength, to estimate the photolysis rates of the molecules in the atmosphere. The photolysis rates J were calculated considering the spectroradiometry technique, where we used the solar actinic flux $F(z,\lambda)$[3], the experimental photoabsorption cross section $\sigma(\lambda)$ and the quantum yield for dissociation $\phi(\lambda)$[4] [152]:

$$J = \int\int F(z,\lambda)\sigma(\lambda)\phi(\lambda)d\lambda dz. \tag{5.2}$$

The photolysis lifetime is therefore simply reciprocal of the total photolysis rate, giving by J^{-1}.

Longer photolysis lifetimes of several hundreds of sunlit days were calculated for both sevoflurane and isoflurane, at altitudes below the stratopause. This indicates that these anaesthetics cannot be broken up efficiently by VUV absorption at these altitudes. However, once in the stratosphere, UV photoabsorption may be the dominant process that releases halogen atoms that can degrade the ozone layer.

The work of Andersen et al. [11], reports a comprehensive study on the reactions of isoflurane and sevoflurane with chlorine atoms and OH radicals. Sevoflurane has a

[2]The last decimal of energy value is given in brackets for these less revolved features.

[3]The solar actinic flux data used in the calculation of the photolysis rate is from a NASA report [53].

[4]The quantum yield for dissociation gives the rate of absorptions that results in dissociation of the target molecule, since this rate is not known for the anaesthetics subject of this work, in the present photolysis rate calculations, we assume to be unity. Studies have shown that the quantum yield for dissociation of halogenated compounds are usually very close to one [151], suggesting that this is a good estimated value.

rate coefficient for reactions with chlorine atoms at room temperature of $(1.1 \pm 0.1) \times 10^{-13} cm^3 molecule^{-1} s^{-1}$ while for isoflurane this is $(4.5 \pm 0.8) \times 10^{-15} cm^3 molecule^{-1} s^{-1}$ [11]. In the case of sevoflurane the room temperature rate coefficients for OH radicals are $(7.3 \pm 2.2) \times 10^{-14} cm^3 molecule^{-1} s^{-1}$ while for isoflurane the value is $(1.5 \pm 0.2) \times 10^{-14} cm^3 molecule^{-1} s^{-1}$ [11]. As far as atmospheric implications are concerned, these authors have pointed out that the interaction of isoflurane and sevoflurane with OH radicals and Cl atoms can determine their fate in the Earth's atmosphere, although the concentration of Cl atoms is not sufficient to determine the lifetime of these anaesthetics [11]. Additionally, the reactions initiated by the degradation products of these anaesthetics are not of environmental concern [11], yet these may provide one of the main sink mechanism of isoflurane and sevoflurane in the Earth's atmosphere. Nonetheless, compared with OH radical reactions for halothane, $(1.5 \times 10^{-14} cm^3 molecule^{-1} s^{-1}$ [54, 147]) UV photolysis is not expected to play a significant role in the tropospheric removal of the halothane molecules. Therefore, compared with radical reactions, UV photolysis is not expected to play a significant role in the tropospheric removal of these molecules.

At 20km, isoflurane has a photolysis lifetime of ~ 80 years, sevoflurane of ~ 50 years. Above to 30km, the lifetime rates drops to less than two years for sevoflurane, less than one year for isoflurane. For halothane[5] the calculation showed less than 100 sunlit days at altitudes above 20 km and less than a day above 30 km.

[5]The photoabsorption measurements of halothane molecule used for the calculation of the photolysis rate were carried out by LCAM research group prior to this work, and published by Ferreira da Silva at al.[147]. Such is shown here for the purpose of comparison.

Chapter

6 Results: Electronic State Spectroscopy of Methanol

"While I am describing to you how nature works, you won't understand why nature works that way. But you see, nobody understands that..
— Richard P. Feynman, QED: The Strange Theory of Light and Matter

Methanol is a molecule notorious for its greenhouse potential that occurs naturally during the decomposition of organic matter, and that is one of the reasons it's present in significant amounts in the Earth's atmosphere. It is the second most abundant tropospheric volatile organic compound, with mixing ratios regularly exceeding 10 parts per billion [153]. Another factor leading to an increase in the emissions of such species into the lower atmosphere is the current urgent need to use alcohols as renewable energy sources, making the interaction of alcohols with UV radiation extremely relevant from the environmental point of view [154]. It is the simplest of the alcohols, being extensively explored in the literature [154–159], which makes it a prototype molecule, and its comparison with other molecules of environmental interest a very useful tool. Methanol is also a vital molecule within the interstellar chemistry because the UV photodissociation of condensed methanol is thought to be the main mechanism that drives the formation of more complex molecules which are incorporated into the protoplanetary disks of new solar systems [155–159].

In this chapter we report results on the electronic state spectroscopy of methanol molecules by high resolution photoabsorption spectroscopy and comprehensive *ab initio* theoretical calculations on the lowest-lying valence (singlet and triplet), Rydberg and ionisation states.

6.1 Electronic structure of methanol

Methanol has C_s symmetry in its electronic ground state, with representations available A' and A". The *ab initio* calculations at the $LC-\omega PBE$, were performed with two different sets of basis functions: the $aug-cc-pVTZ$ [123, 143] already used for the molecules above, and the $aug-cc-pVQZ$ [124], both using the same extended set of diffuse functions (5s5p2d) located at the mass centre of the molecule for a better description of the Rydberg orbitals, as mentioned for the anaesthetics. The electronic configuration of the ground state $\tilde{X}^1A'$ of methanol is: $1a'^2\ 2a'^2\ 3a'^2\ 4a'^2\ 5a'^2\ 1a''^2\ 6a'^2\ 7a'^2\ 2a''^2$.

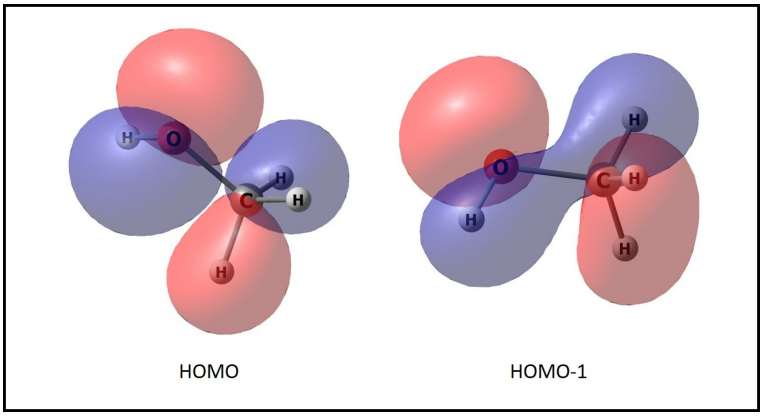

Figure 6.1: Representation of the two highest occupied molecular orbitals (HOMO and HOMO-1) of methanol, obtained by LC-ωPBE/aug-cc-pVTZ calculations using Gaussian 09 [122] and visualized using Chemcraft software [146].

The highest occupied molecular orbital (HOMO), $2a''$, is primarily the lone pair orbital of oxygen atom $O(2p)$, perpendicular to the plane of the molecule, and the second highest occupied molecular orbital (HOMO-1) is a combination of $C(2p)$, $O(2p)$ and $H(1s)$ atomic orbitals, both are shown in Figure 6.1.

6.1.1 Electronic excitation of methanol

In the photoabsorption cross section of methanol (CH_3OH), shown in Figure 6.2, there are four clearly distinct main structures: a weak continuous feature lying between 6.0-7.5 eV, two sharp intense vibronic structures, peaking at about 7.7 eV and 8.2 eV and a well-pronounced continuous increasing structure with some weak features, above 8.9 eV. The vertical excitation energies and oscillator strengths (singlet and triplet states), calculated at $TD-DFT/LC-\omega PBE$ level for the two sets of basis functions, are presented in Table 6.1.

The assignment of the transitions show some discrepancies from the available information in the literature. The week continuum lying between $6.0-7.5eV$ was first assigned as a transition to an unoccupied valence orbital (σ^*) [160–162] and latter re-assigned as a transition to a Rydberg orbital [163–165]. The two sharp vibronic progressions are both transitions to a 3p Rydberg states, were it is possible to identify some vibrational

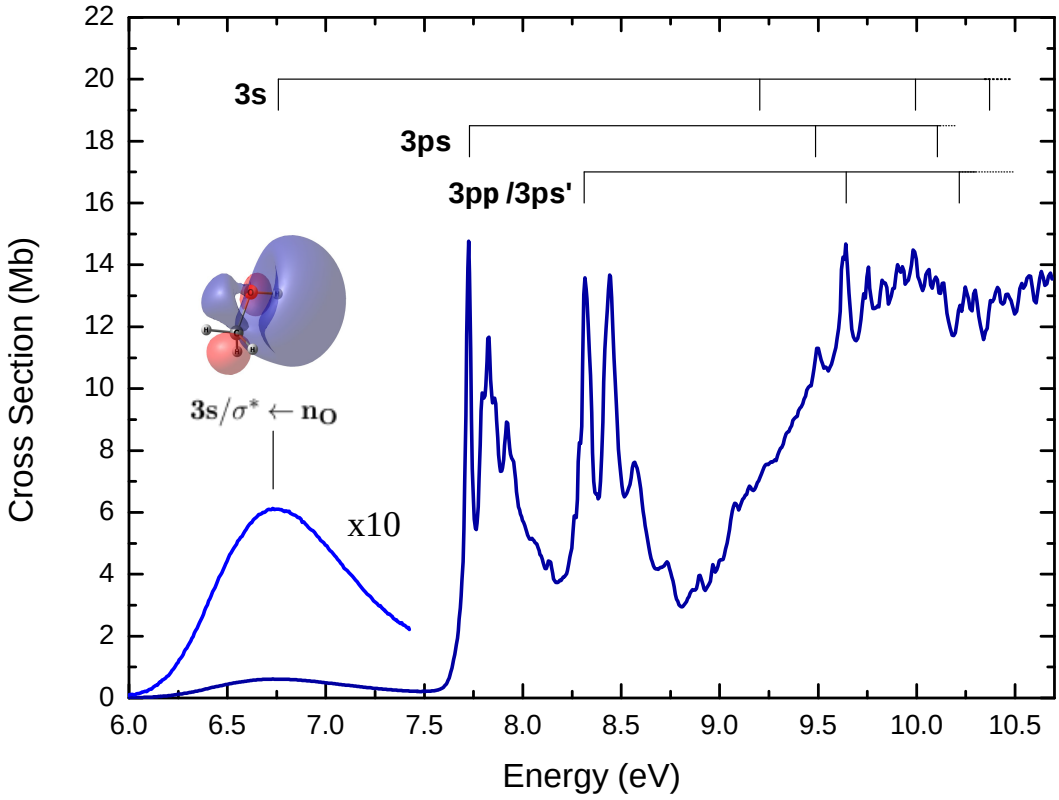

Figure 6.2: VUV photoabsorption cross-section of methanol.

structures. The pronounced increasing structure consists of an overlap of several transitions, with small spacings, which makes very difficult the identification of each one in the photoabsorption spectrum, as well as assignment of the vibrational modes present in this region.

6.1.1.1 Valence excitation of methanol

As shown in Table 6.1, the excited states are here assigned as valence/Rydberg mixed character or strictly Rydberg orbitals.

The continuous smooth feature lying between $6.0 - 7.5eV$ presents a broad and weak structure. This is a characteristic shape of a valence orbital, previously assigned in references [160–162]. In 1970, Robin and Kuebler [163] assigned this transition to a *3s* Rydberg orbital. According to this study *"the big-orbit, Rydberg nature of the first three singlet upper states of methanol can be demonstrated using the unique effect of high pressure gases on Rydberg transitions"* [163, 166]. The same study also compares methanol (CH_3OH) with water (HOH), together with a set of other $X - OH$ molecules, where it is pointed out that "*the first broad band at 6.8 eV in both the electron impact and optical spectra of methanol seems to be analogous to the broad, featureless band at 7.44 eV in water*"[163]. In 2002, Cheng et al. [165] reported that the first excited state of methanol is well described as a $3s$ Rydberg orbital rather than a valence character, through the inspection of the

electronic density of the lowest unoccupied molecular orbital (LUMO) of the ground state calculated with $TD-DFT$ method.

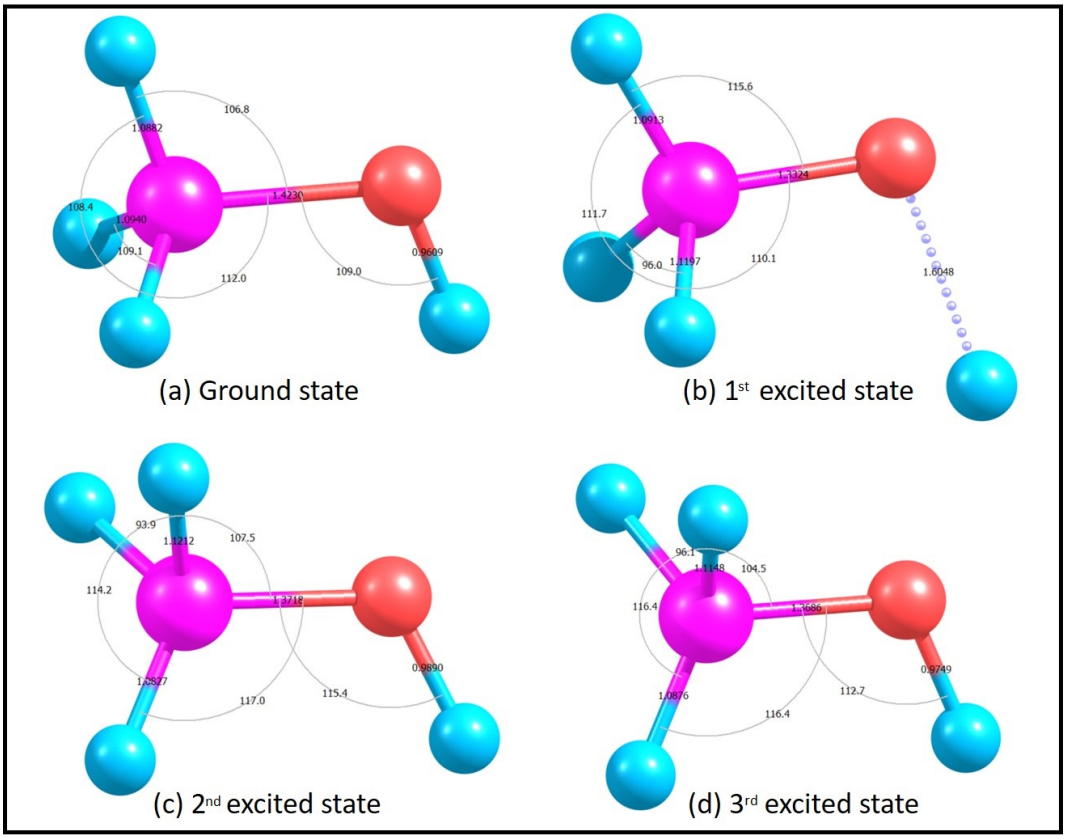

Figure 6.3: Geometry of methanol for (a) the ground state, (b) the first excited state $3s/\sigma^*(OH)$, which is nearly dissociative, (c) the second and (d) third excited states, both 3p Rydberg orbitals and eclipsed. Calculations were performed in TD-DFT level, using Q-Chem code, version 4.3 [167].

Nevertheless, we can not ignore the high value of the quantum defect obtained in this work, both for the experimental and for the theoretical data, of 1.20 and 1.16, respectively[1], such also highlighted by Salahub and Sandorfy [161]. Furthermore, the calculations for the molecular geometries, in Figure 6.3, show a distortion of the equilibrium geometry in the first excited state, at the $O-H$ bond, which means an antibonding valence orbital must be involved, since transitions from a nonbonding valence orbital to a purely Rydberg orbital should not result in a change of the distances between the atoms [168]. For this reason, we chose to assign the lowest unoccupied molecular orbital (LUMO) of methanol as being a valence/Rydberg mixed character $3s/\sigma^*$ orbital.

[1]The quantum defects of methanol, together with the Rydberg series, are presented in Table 6.2.

	aug-cc-pVQZ+R		aug-cc-pVTZ+R		Assignment		
Transition	E(eV)	f_L	E(eV)	f_L	HOMO	HOMO-1	E(eV) Exp.
$\tilde{X}^1A$'							
1^3A"	6.608	0	6.597	0	$3s\sigma/\sigma^*(O-H)$		
2^1A"	6.926	0.0027	6.916	0.0028	$3s\sigma/\sigma^*(O-H)$		6.75(3)$^{(b)}$
3^3A'	7.904	0	7.895	0	$3p\sigma$		
4^1A"	8.129	0.0293	8.120	0.0294	$3p\sigma$		7.72(0)
5^3A'	8.261	0	8.2585	0	$3p\pi$		
$6^3A''$	8.371	0	8.367	0	$3p\sigma'$		
7^3A'	8.386	0	8.378	0	$3s\sigma/\sigma^*(O-H)$		
8^1A'	8.424	0.0245	8.421	0.0247	$3p\pi$		8.31(5)
9^1A"	8.429	0.0072	8.425	0.0069	$3p\sigma'$		8.96(5)
10^1A'	8.724	0.0012	8.718	0.0012		$3s\sigma/\sigma^*(O-H)$	
11^3A"	8.929	0	8.924	0	$3d\sigma$		
12^1A"	9.012	0	9.008	0	$3d\sigma$		
13^3A"	9.142	0	9.146	0	$3d\sigma'$		
14^3A'	9.197	0	9.194	0		$3d\pi$	
15^1A"	9.222	0.0017	9.224	0.0018	$3d\sigma$		
16^3A"	9.281	0	9.277	0	$3d\sigma''$		
17^3A'	9.294	0	9.300	0	$3d\pi'$		
18^1A'	9.303	0.0010	9.311	0.0014		$3d\pi$	
19^1A"	9.326	0.0006	9.3219	0.0008	$3d\sigma''$		
20^3A'	9.382	0	9.379	0	$3d\pi'$	$3p$	
21^3A"	9.394	0	9.393	0	$3d\sigma/\sigma^*$		
22^1A"	9.413	0	9	0	$3d\sigma/\sigma^*$		
23^1A'	9.430	0.0032	9.428	0.0031	$3d\pi/\sigma^*$		
24^3A"	9.499	0	9.491	0	$4p\sigma/\sigma^*$		
25^1A"	9.575	0.0058	9.567	0.0057	$4p\sigma/\sigma^*$		
26^3A'	9.617	0	9.610	0	$4p\pi$		
27^1A'	9.6220	0.048	9.616	0.048		$3p\sigma'/\sigma^*$	
28^3A"	9.642	0	9.636	0	$4p\sigma'/\sigma^*$		

Table 6.1: Calculated vertical excitation energies ($TD-DFT/LC-\omega PBE$) and oscillator strengths of methanol (CH_3OH) compared with experimental data (energies in eV).The singlet transitions are show in black, while the triplet transitions are shown in blue.
^{b} indicates broad structure.

6.1.1.2 Rydberg excitation of methanol

All the excited states of methanol have a Rydberg character, some of them mixed with valence orbitals. The first structure of the VUV photoabsorption spectrum, in Figure 6.2 peaks at 6.753 eV, with a maximum of 0.61 Mb, in excellent agreement with previous studies [160, 161, 169]. The two absorption bands with sharp vibronic structures, with peaks at 7.72 and 8.32 eV, are both assigned to 3p Rydberg transition, following the classification of Robin [163, 164] and Nee, Suto and Lee [169]. The calculated energies for each transition, and their respective assignment, are presented in Table 6.1, and the representation of all molecular orbitals are shown in appendix D. The calculations show that the third and the forth exited states are almost degenerated, with calculated energies of 8.424 and 8.429eV for the $aug-cc-pVQZ+R$ set of basis function, and energies of 8.421 and 8.425 eV for $aug-cc-pVTZ+R$, however these are not distinguishable in the photoabsorption spectrum.

We have performed calculations of the first members of the Rydberg series for methanol (Table 6.2), and the quantum defects are used only as an additional tool for the assignment. The identification of Rydberg states was based more firmly on the symmetry and shape of the single occupied orbitals and the values of the oscillator strengths (Table 6.1).

For the members of the Rydberg series converging to the ionic electronic ground state (10.94 eV), we have assigned $3s$, $4s$ $5s$, features at 6.745, 9.231 and 9.983 and 10.43(6) eV with quantum defects of the first two members of 1.19, and the third of 1.22. This is notoriously considered a very high value for a s orbital, but Robin's studies regarding the effects of high pressure gases on Rydberg transitions [163, 164] were taken into account, as was discussed in section 6.1.1.1. Note that the 6.745 eV feature has mixed valence/ Rydberg character, $3s/\sigma^*$.

Vertical energy	δ	Assignment
		(18a") $\rightarrow ns$
6.745	1.19	3s
9.231	1.19	4s
9.983	1.22	5s
		(18a") $\rightarrow np$
$7.72(0)^{(s)}$	0.94	3p
$9.492^{(s)}$	1.06	4p
$10.101^{(s)}$	1.05	5p
		(18a") $\rightarrow np'$
8.315	0.72	3p'
9.641	0.76	4p'
10.221	0.65	5p'

Table 6.2: Energies (eV), quantum defects (δ), and assignments of the ns, np and np' Rydberg series converging to the ionic electronic ground state $(18a'')^{-1}$, with $IE_1 = 10.94eV$, of methanol.

6.1.1.3 Ionisation energies of methanol

Photo-ionisation of methanol has been extensively investigated over the years by several groups [170–174]. The experimental data of the first ionisation energy, which corresponds to the removal of an electron from de $2a''$ orbital, ranges from 10.83 to 10.96 eV among the several studies available in the literature. In this study we take the ionisation energies from Robin [163, 164], listed in Table 6.3.

Orbital	E(eV)
$2a''^{-1}$	10.94
$7a'^{-1}$	12.62
$6a'^{-1}$	15.21
$1a''^{-1}$	15.64
$5a'^{-1}$	17.62
$4a'^{-1}$	22.65
$3a'^{-1}$	32.20
$2a'^{-1}$	292.3
$1a'^{-1}$	538.9

Table 6.3: Experimental vertical ionisation energies (eV) of methanol, from [163, 164].

6.1.1.4 Vibrational excitation of methanol

At least five vibrational modes are clearly identified in the photoabsorption spectrum of methanol, in Figure 6.2. The calculated harmonic modes[2] for the ground state and the first four excited states of methanol are shown in Table 6.5, along with the experimental data in Figure 6.4.

The first excited state, assigned to a transition to a $3s/\sigma^*$ orbital has a smooth week structure in the VUV spectrum, with no visible fine structure, but the calculated harmonic modes are presented in Table 6.5.

The second excited state of methanol is a vibronic structure between 7.6 and 8.2 eV, assigned to a 3p Rydberg transition, were it is possible to observe four distinct vibrational modes: the $O-H$ stretching ($\sim 3311 cm^{-1}$, ν_1), the CH_3 rocking ($\sim 1066 cm^{-1}$, ν_{10} or ν_9), $C-O$ stretching ($\sim 786-806 cm^{-1}$, ν_{11}) and the CH_3 torsion ($\sim 517-548 cm^{-1}$, ν_{12}), shown in Figure 6.4. The assignment of the harmonic modes was made based on the theoretical calculations for the second excited state, shown in Table 6.5, where the frequency of the CH_3 torsion mode in the first $3p\sigma$ state is $425.84 cm^{-1}$. The ν_{11} vibrational mode ($C-O$ stretching) is consistent with previous works, Sominska and Gedanken [175] reported an harmonic of frequency $825 cm^{-1}$, Cheng et al. [165] of $806 cm^{-1}$, and Nee, Suto and Lee [169] of $870 cm^{-1}$.

[2]The calculations of the harmonic modes of methanol were performed by the collaboration reasarch group in Lille University, France, in the purpose of this study.

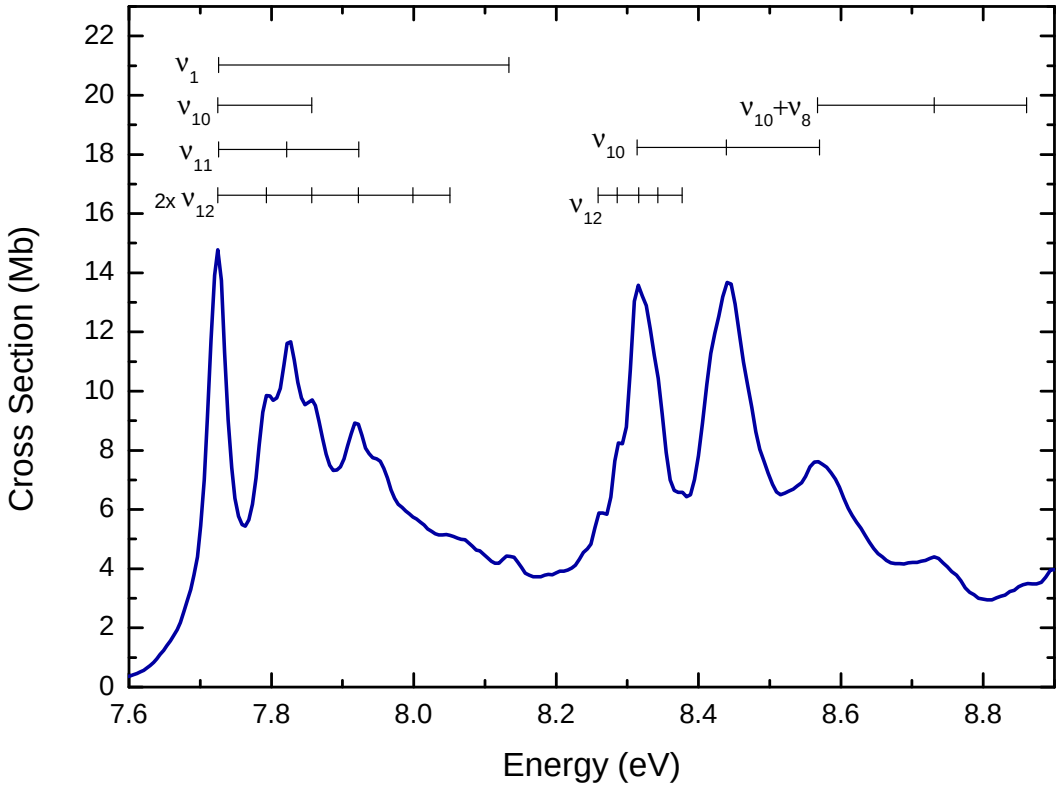

Figure 6.4: VUV photoabsorption spectrum in the energy range of the first and second vibronic structure of methanol.

Only one additional harmonic frequency was reported by Nee, Suto and Lee, of $620-520cm^{-1}$, while Cheng et al. [165] [165] reported harmonics of 3322, 1087 and $573cm^{-1}$, assign to $O-H$ stretching, $C-O-H$ bending and CH_3 wagging modes, respectively.

In the region between 8.2 and 8.9 eV, the calculations show two nearly degenerated transitions from HOMO to $3p\pi(A'')$ and to $3p\sigma'(A')$, but they are not distinguishable in the photoabsorption spectrum. In this range of energy, two vibrational modes of $\sim 1004-1034cm^{-1}$ and $\sim 222-272cm^{-1}$ are discernible. The first, CH_3 rocking (ν_{10} or ν_9) is also reported by Cheng et al. [165] and Sominska and Gedanken [175], both with values of $\sim 1050cm^{-1}$, the second, CH_3 torsion ν_{12}, was only observed by Cheng et al. [165], at of $\sim 198cm^{-1}$. In this region there is a significant difference in the harmonic frequency of the torsion mode, $146.88cm^{-1}$ for the calculations of the third excited state, $3p\pi$, shown in Table 6.5. A third is also observed, at $\sim 1049-1314cm^{-1}$, and is probably a combination of $O-H$ bending (ν_8) and CH_3 rocking (ν_{10} or ν_9) modes.

There are two shoulders (at 8.260 and 8.288 eV) that appear in the left of the electronic transition (at 8.315 eV), with spacing of $\sim 222cm^{-1}$. It is reasonable to assume that the CH_3 torsion (ν_{12}) begins at 8.60 eV. Another possibility is that these weak features are sequence bands, due to closely spaced members and the high population for vibrational excitation in the ground state at room temperature [71, 74, 75, 77].

Rydberg state	Vibrational level	Energy	$\Delta\nu$	Assignment
$3p\sigma$	$\nu_1 = 0$	$7.72eV$		O-H stretching
	$\nu_1 = 1$	$8.13eV$	$3311cm^{-1}$	
	$\nu_{10} = 0$	$7.72eV$		CH_3 rocking
	$\nu_{10} = 1$	$7.86eV$	$1065cm^{-1}$	
	$\nu_{11} = 0$	$7.72eV$		C-O stretching
	$\nu_{11} = 1$	$7.82eV$	$817cm^{-1}$	
	$\nu_{11} = 2$	$7.92eV$	$798cm^{-1}$	
	$\nu_{12} = 0$	$7.72eV$		CH_3 torsion
	$\nu_{12} = 2$	$7.79eV$	$548cm^{-1}$	
	$\nu_{12} = 4$	$7.86eV$	$517cm^{-1}$	
	$\nu_{12} = 6$	$7.92eV$	$548cm^{-1}$	
	$\nu_{12} = 8$	$7.99eV$	$597cm^{-1}$	
	$\nu_{12} = 10$	$8.05eV$	$508cm^{-1}$	
$3p\sigma'/3p\pi$	$\nu_{10} = 0$	$8.31eV$		CH_3 rocking
	$\nu_{10} = 1$	$8.44eV$	$1008cm^{-1}$	
	$\nu_{10} = 2$	$8.57eV$	$1056cm^{-1}$	
	$\nu_{12} = 0$	$8.26eV$		CH_3 torsion
	$\nu_{12} = 1$	$8.29eV$	$226cm^{-1}$	
	$\nu_{12} = 2$	$8.31eV$	$217cm^{-1}$	
	$\nu_{12} = 3$	$8.34eV$	$218cm^{-1}$	
	$\nu_{12} = 4$	$8.38eV$	$274cm^{-1}$	
	$\nu_8 + \nu_{10}$ [a]	$8.57eV$		O-H bending + CH_3 rocking
	$\nu_8 + \nu_{10}$ [a]	$8.86eV$	$2371cm^{-1}$	

Table 6.4: Experimental energies and vibrational frequencies ($\Delta\nu$, in cm^{-1}) for vibrational levels of the Rydberg states.

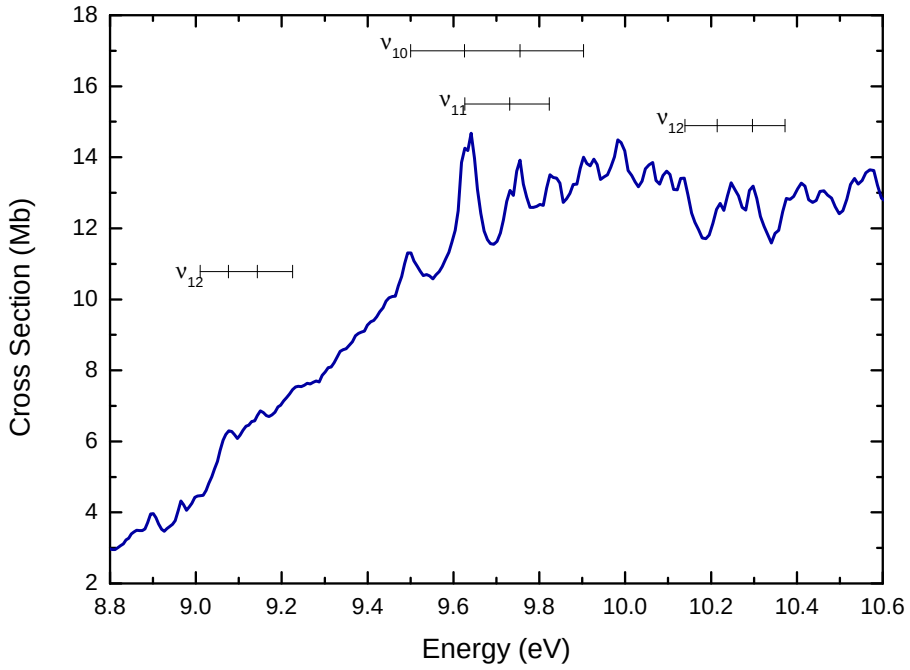

Figure 6.5: VUV photoabsorption spectrum in the range of energy of the third vibronic structure of methanol molecule.

Exp.[a] (cm^{-1})	Calculated[b] (cm^{-1})	Sym.		Mode
	Ground State (staggered)			
222	301	a”	ν_{12}	CH_3 torsion
1004	1040	a’	ν_{11}	C-O stretching
1066	1077	a’	ν_{10}	CH_3 rocking
	1170	a”	ν_9	CH_3 rocking
1314	1366	a’	ν_8	O-H bending
	1477	a’	ν_7	C-H in-plane sym. bending
	1498	a”	ν_6	C-H out-plane asym. bend
	1508	a’	ν_5	C-H in-plane asym. bend
	2993	a’	ν_4	C-H parallel sym. stretch
	3039	a”	ν_3	C-H perp. asym. stretch
	3106	a’	ν_2	C-H perp. asym. stretch
3311	3826	a’	ν_1	O-H stretch
	$3s/\sigma^*(OH)(staggered)$			
	18	a”		CH_3 torsion
	454	a’		O-H bending
	923	a”		CH_3 rocking
	961	a’		C-O stretching
	1035	a’		O-H bending
	1174	a’		C-H in-plane asym. bending
	1294	a’		C-H in-plane sym. bending
	1460	a”		C-H out-plane asym. bending
	1500	a’		CH_3 rocking
	2706	a”		C-H perp. asym. stretching
	2768	a’		C-H paral. sym. stretching
	3064	a’		C-H perp. asym. stretching
	first $3p\sigma(eclipsed)$			
	425	a”		CH_3 torsion
	781	a’		C-O stretching
	979	a”		CH_3 rocking
	1012	a’		CH_3 rocking
	1158	a’		C-H in-plane sym. bending
	1252	a’		O-H bending
	1315	a”		C-H out-plane asym. bending
	1451	a’		C-H in-plane asym. bending
	2964	a’		C-H paral. sym. stretching
	3114	a”		C-H perp. asym. stretching
	3184	a’		C-H perp. asym. stretching
	3556	a’		O-H stretching
	first $3p\pi(eclipsed)$			
	146	a”		CH_3 torsion
	773	a’		CH_3 rocking
	957	a”		CH_3 rocking
	1092	a’		C-H in-plane sym. bending
	1196	a’		C-O stretching
	1255	a”		C-H out-plane asym. bending
	1291	a’		O-H bending
	1449	a’		C-H in-plane asym. bending
	2909	a”		C-H perp. asym. stretching
	2928	a’		C-H paral. sym. stretching
	3093	a’		C-H perp. asym. stretching
	3705	a’		O-H stretching

Table 6.5: The vibrational frequencies (in cm^{-1}) [a] observed in the VUV photoabsorption spectra of methanol [b] and calculated by the collaboration research group in Lille.

The last structure of the VUV methanol spectrum, above 8.8eV, shows some weak vibrational features overlapping with a large increasing continuous structure. According to the theoretical calculations most of the electronic transitions in this regions are concentrated around 9.6eV and 10.1eV, all of them are listed and assigned in Table 6.1.

Nee et al. [169] associated those structures to transitions related with higher Rydberg states, however, as noted in the aforementioned study, only a comparison with isotopic data can confirm this assumptions. In this range of energy, shown in Figure 6.5, it is also possible to identify the $C-O$ stretching vibrational mode (ν_{11}), with frequencies of $853-872cm^{-1}$, the CH_3 rocking (ν_{10}), with frequencies of $1003-1070cm^{-1}$, and also two other harmonics, of $595-603cm^{-1}$ and $616-660cm^{-1}$, both probably associated with the CH_3 torsion (ν_{12}). Nee et al. [169] identifies another Rydberg series, nd initiating with $n=3$ at 8.99eV (72500 cm^{-1}), which coincides with the beginning of a CH_3 torsion vibrational mode (ν_{12}). Unfortunately, due to the successive overlaps, we were not able to identify in the spectrum (Figure 6.5) where this series begins.

6.2 Discussion

The photolysis rates methanol were estimated considering the spectroradiometry technique, where were used the solar actinic flux $F(\lambda)$ from the literature [176], the experimental photoabsorption cross section $\sigma(\lambda)$ and the quantum yield for dissociation[3] [152] using Equation 5.2.

Methanol has a calculated photolysis lifetime of approximate 13 years at 20km, the life time drops to 108 days at 30km, which implies that VUV absorption cannot efficiently break methanol in the lower troposphere. Above 30km, the lifetime rates decrease to less than 100 sunlit days. Nonetheless, the work of Jiménez, Gilles and Ravishankara [177] studied the kinetics of the reaction of the hydroxyl radical with methanol as a function of the temperature given as $3.6\pm0.8\exp^{-(415\pm70)/T}\times10^{-13}cm^3molecule^{-1}s^{-1}$, and most studies available in literature agree well with an average value for room temperature of $9.4\times10^{-13}cm^3molecule^{-1}s^{-1}$ [178–181]. With a tropospheric lifetime of 10 to 14 days [153, 182–184] the reaction with OH is the main sink mechanism for methanol molecules in the troposphere. Indeed, studies on the global budget of methanol [182] report that gas-phase oxidation by OH is responsible for 63% of the global sink balancing, from the total source of $206Tg/yr$, which means that photolysis plays a minor role in the tropospheric removal of methanol.

[3] In the present photolysis rate calculations, we assume the quantum yield for dissociation to be unity.

Chapter

7 Final Considerations

"And whereas sense and memory are but knowledge of fact, which is a thing past and irrevocable, science is the knowledge of consequences, and dependence of one fact upon another."
— Thomas Robbes, Leviathan

7.1 Conclusions

In this thesis we have presented studies for characterization of electronic states of molecules with environmental impact, through VUV-photoabsorption and elastic electron scattering by some of the volatile anaesthetics currently in use, in order to comprehensively describe the underlying molecular mechanisms of these molecules.

The main focus of this contribution, regarding the electron-molecule collision studies, was to validate the use of two different but complementary theoretical methods to describe the scattering dynamics in elastic electron collisions with sevoflurane, isoflurane and halothane anaesthetic compounds in the low- to intermediate-energy region. As far as these molecules are concerned, we have presented for the first time a joint experimental and theoretical investigation on the elastic differential cross sections. Below 20 eV electron impact, these results have shown a reasonable agreement between our experimental data and the Schwinger multichannel method whereas above this energy the independent atom model method describes very well the experimental findings. Also interesting to note is the excellent agreement of the IAM-SCAR+I calculation, including rotational excitations, to describe below 20 eV the asymptotic behaviour of the experimental DCS in the forward direction. Finally, for the entire energy region investigated, 10-50 eV, the methodology implemented shows the relevance of combining both theoretical methods to help describing

the experimental finds. This joint work opens up the possibility to extend these studies to other molecular targets.

Moreover, we present, for isoflurane, sevoflurane and methanol molecules, results from VUV photoabsorption measurements over the energy range 5-10.8eV, together with *ab initio* theoretical calculations of the vertical excitation energies and oscillator strengths. This combined experimental and theoretical study allows a comprehensive description and characterization of the electronic states of these chemical compounds, and also provided the first reliable set of absolute photoabsorption cross sections available and electron excitation transitions for sevoflurane, isoflurane. The measured photoabsorption cross sections were also used to calculate the photolysis lifetime of the molecules in the Earth's atmosphere from ground level up to the limit of the stratopause. Absorption bands attributed to valence and Rydberg transitions were observed, and a number of new assignments proposed on the basis of comparisons with the present ab initio calculations. Regarding the methanol molecule, we were able to observe more transitions than in previous works, and reassigned some of the transitions and the vibrational modes. Such was possible because we have employed more diffuse sets of bases functions and also because the measurements were performed in a high-resolution ($\Delta\lambda = 0.075nm$) experimental set up.

7.2 Future Work

A priority for future work would be the electron-molecule collision energy loss measurements of sevoflurane, isoflurane and halothane molecules, in dipolar and non-dipolar conditions, particular the later to record the first time experimental evidence of transitions to triplet states in the halothane molecule, already predicted by theoretical calculations. In fact, such measurements were planned to be performed within the scope of this work, however due to time constraints that was not possible to do in due time.

It would also be quite interesting to perform the same set of measurements (VUV-photoabsorption and electron-molecule collision), and the related calculations, for other anaesthetics, as Enflurane and Desflurane.

For a fairly complete characterization of the electronic states of volatile anaesthetics that are environmental relevant, we intend to perform electron induced fragmentation measurements, through ion-molecule collision experiments, as far as photo-ionization and dissociative electron attachment measurements.

Appendix

A Hartree-Fock Method

The *Hartree-Fock* Method [58] is the most used approximation in quantum chemistry, capable of providing a good approximate solution to the problem of many electrons. The main idea of the method is to simplify the problem of many electrons in order to make possible its computational implementation.

The method uses a single *Slater* determinant to describe the electronic wave function, which already carries the antisymmetric character of the problem of many electrons, and for that uses the spin-orbitals. Where the molecular orbitals are expanded in terms of a base of atomic orbitals, represented by functions of the Gaussian-Cartesian type, whereupon coefficients are found through the self-consistent method, and constitute the set of basic functions that describes the molecule [56].

A.1 The Slater Determinant

The wave function $\chi_i(\vec{r},\omega)$ to one electron, that describes its spatial distribution and its spin, is called spin-orbital. To describe the wave function of a N electrons system, it's used a combination of spin-orbitals of each electron that obeys the Pauli's principle of the exclusion named *Slater Determinant* [185], which allows to use N functions spin-orbitals (which refers to a single electron), instead of finding a wave function that depends on the coordinates of N electrons.

$$\psi = \psi(\vec{r}_1,\vec{r}_2,\ldots,\vec{r}_N,\omega) = (N!)^{-1/2}\begin{vmatrix} \chi_i(\vec{r}_1,\omega_1) & \chi_j(\vec{r}_1,\omega_1) & \cdots & \chi_k(\vec{r}_1,\omega_1) \\ \chi_i(\vec{r}_2,\omega_2) & \chi_j(\vec{r}_2,\omega_2) & \cdots & \chi_k(\vec{r}_2),\omega_2 \\ \vdots & \vdots & & \vdots \\ \chi_i(\vec{r}_N,\omega_N) & \chi_j(\vec{r}_N,\omega_N) & \cdots & \chi_k(\vec{r}_N,\omega_N) \end{vmatrix} \tag{A.1}$$

$$\chi(\vec{r},\omega) = \varphi(\vec{r})\alpha(\omega) \text{ or } \chi(\vec{r},\omega) = \varphi(\vec{r})\beta(\omega)$$

were φ are functions merely of the spatial coordinates of an electron, called molecular orbitals, α represents the spin up and β represents the spin down.

A.2 Hartree-Fock Approximation

The essence of the *Hartree-Fock* approximation is to replace the problem of many electrons, by a simpler problem, of a single electron, where the electron-electron repulsion is treated as a mean repulsion (mean field approximation). The objective is to obtain a solution of the *Schrödinger* equation for the problem of many electrons:

$$\mathcal{H}_e|\psi\rangle = \mathcal{E}_0|\psi\rangle. \tag{A.2}$$

were (2.1) is the electronic Hamiltonian of the system, given by:

$$\mathcal{H}_e = -\sum_{i=1}^{N}\frac{1}{2}\nabla_i^2 - \sum_{i=1}^{N}\sum_{A=1}^{M}\frac{Z_A}{r_{iA}} + \sum_{i=1}^{N}\sum_{j>i}^{N}\frac{1}{r_{ij}}. \tag{A.3}$$

The first term of the Hamiltonian refers to the kinetic energy of the electrons, the second term refers to the Coulomb interaction between the electrons and nuclei, and the third one to the repulsion between electrons.

As we consider closed-shell systems, the spin part is summed, leaving only the spatial part. This is because there is no correlation in the motion between electrons with opposed spins, which is the case of electrons in a closed-shell orbital. Only the motion of electrons with parallel spins is correlated. We will then have only N/2 molecular orbitals, each of them doubly occupied, corresponding to a singlet type state.

The expectation value of the electronic energy of the ground state is given by:

$$\mathcal{E}_0 = \langle\psi|\mathcal{H}_e|\psi\rangle, \tag{A.4}$$

As the variational method always gives us an upper-value approximation, the wave function that brings us closer to the exact solution of the Hamiltonian operator is one that minimizes the functional of the expectation value:

$$\mathcal{E}[\varphi] = \sum_a \langle\varphi_a|h|\varphi_a\rangle + \frac{1}{2}\sum_{a,b}(\langle\varphi_a\varphi_b|\varphi_a\varphi_b\rangle - \langle\varphi_a\varphi_b|\varphi_b\varphi_a\rangle). \tag{A.5}$$

The minimization criterion is met by the Hartree-Fock equation:

$$\mathcal{F}(i)|\varphi_a(\vec{r}_i)\rangle = \epsilon_a|\varphi_a(\vec{r}_i)\rangle. \tag{A.6}$$

were ϵ_a is the energy associated with the ϕ_a orbital and $\mathcal{F}(i)$ is the effective Hamiltonian of a single electron, called *Fock operator* and given by

$$\mathcal{F}(i) = -\frac{1}{2}\nabla_i^2 - \sum_{A=1}^{N}\frac{Z_A}{\vec{r}_{iA}} + \upsilon^{HF}(i), \tag{A.7}$$

being, the first and second terms of the *Fock operator*, the contributions of kinetic energy and interaction with nuclei, respectively; and $\upsilon^{HF}(i)$ is the effective potential felt by the *i-th* electrons due to all the others, called *Fock potential* and is given by

$$\upsilon^{HF}(i) = \sum_{j}^{N/2} [2\mathcal{J}_j(i) - \mathcal{K}_j(i)], \tag{A.8}$$

were

$$\mathcal{J}_j(\vec{r}_a)\varphi_i(\vec{r}_a) = \left[\int d\vec{r}_b \varphi_j^*(\vec{r}_b)\frac{1}{|\vec{r}_a - \vec{r}_b|}\varphi_j(\vec{r}_b)\right]\varphi_i(\vec{r}_a), \tag{A.9}$$

and

$$\mathcal{K}_j(\vec{r}_a)\varphi_i(\vec{r}_a) = \left[\int d\vec{r}_b \varphi_j^*(\vec{r}_b)\frac{1}{|\vec{r}_a - \vec{r}_b|}\varphi_i(\vec{r}_b)\right]\varphi_j(\vec{r}_a), \tag{A.10}$$

are respectively the Coulomb and exchange operators. The *Coulomb* operator ($\mathcal{J}_j$) represents the *Coulomb* repulsion between two electrons and the exchange operator ($\mathcal{K}_j$) arises from the antisymmetric nature of the determinant and does not have a classical interpretation.

In the Hartee-Fock equation (A.6), the eigenstates are the spins-orbitals and eigenvalues are their respective energies. Since the Fock operator depends on the operators $\mathcal{J}_j$ and $\mathcal{K}_j$, which in turn depend on the spin-orbitals, it is clear that the Fock operator depends on its eigenstates. These factors make the exact solution of these integral-differential equations for molecules impossible. The problem is solved by expanding each molecular orbital into a set of k known basis-functions [186] of Gaussian type:

$$\varphi_i = \sum_{\mu=1}^{k} C_{\mu i}\phi_\mu. \tag{A.11}$$

We define the overlap matrix between two atomic orbitals (which does not necessarily have to be orthogonal):

$$\mathcal{S}_{\mu\nu} = \int d\vec{r}_1 \phi_\mu^*(\vec{r}_1)\phi_\nu(\vec{r}_1), \tag{A.12}$$

and the Fock matrix, which is the matrix representation of the Fock operator $\mathcal{F}(\vec{r}_1)$ with a set of base functions ϕ_μ and corresponds to the effective Hamiltonian of a molecule:

$$F_{\mu\nu} = \int d\vec{r}_1 \phi_\mu^*(\vec{r}_1)\mathcal{F}(\vec{r}_1)\phi_\nu(\vec{r}_1), \tag{A.13}$$

which can also be written as:

$$F_{\mu\nu} = T_{\mu\nu} + V_{\mu\nu}^{nuc} + G_{\mu\nu}, \tag{A.14}$$

were $T_{\mu\nu}$ refers to the kinetic energy of one electron, $V_{\mu\nu}^{nuc}$ to the electron-nuclei interaction and $G_{\mu\nu}$ to the electron-electron interaction, given by:

$$T_{\mu\nu} = \int d\vec{r}_1 \phi_\mu(\vec{r}_1)\left[-\frac{1}{2}\nabla_1^2\right]\phi_\nu(\vec{r}_1), \tag{A.15}$$

$$V_{\mu\nu}^{nuc} = \int d\vec{r}_1 \phi_\mu(\vec{r}_1)\left[\sum_{A=1}^{M} -\frac{Z_A}{|\vec{r}_1 - \vec{r}_A|}\right]\phi_\nu(\vec{r}_1), \tag{A.16}$$

$$G_{\mu\nu} = \sum_{\mu\nu} P_{\lambda\sigma} \left[(\mu\nu|\sigma\lambda) - \frac{1}{2}(\mu\lambda|\sigma\nu) \right], \tag{A.17}$$

were $P_{\lambda\sigma}$ is the density matrix and $(\mu\nu|\sigma\lambda)$ are integral of two electrons:

$$P_{\lambda\sigma} = 2 \sum_{i=1}^{N/2} C_{\lambda i} C_{\sigma i}, \tag{A.18}$$

$$(\mu\nu|\lambda\sigma) = \int d\vec{r}_1 \int d\vec{r}_2 \phi_\mu^*(\vec{r}_1)\phi_\nu(\vec{r}_1) \frac{1}{|\vec{r}_1 - \vec{r}_2|} \phi_\lambda^*(\vec{r}_2)\phi_\sigma(\vec{r}_2). \tag{A.19}$$

Such expansion converts the *Hartree-Fock* equation into a set of algebraic equations that can be solved matrically, called *Hartree-Fock-Roothaan Equations* which are given by:

$$\sum_{\nu=1}^{k} F_{\mu\nu} C_{\nu i} = \epsilon_i \sum_{\nu=1}^{k} \mathcal{S}_{\mu\nu} C_{\nu i}. \tag{A.20}$$

were $C_{\nu i}$ is the matrix of the expansion coefficients.

A.3 The method of Self-Consistent Field

Once the set of basis functions has been defined, as well as its geometry and the charges of the atoms in the molecule, the next step to find the wave function $|\psi_0\rangle$ is to find the Fock Matrix for the closed-shell system, which in turn depends on the matrix of coefficients C, also unknown. Therefore the self consistent field (SCF) computational method is used.

The SCF method consists in the following steps:

1. The integrals for one electron (equations A.15 and A.16), for the interaction between two electrons (equation A.19) and the overlap matrix (equation A.19) are calculates
2. The diagonalization of the overlap matrix and the normalization of the set of base functions are performed.
3. A "guess function" is chosen for the P density matrix, which will works as a starting point.
4. The matrix G is calculated using the equation A.17 and the integrals $(\mu\nu|\sigma\lambda)$.
5. The Fock matrix $F^{(1)}$ is built from the equation (A.14).
6. The eigenvalue problem (equation A.20) is solved, thus determining a set of coefficients $C^{(1)}$.
7. Builds up a new P matrix by the equation A.18, using the new set of coefficients.
8. The G matrix and the Fock matrix $F^{(2)}$ are recalculated.
9. The new Fock matrix is used to solve the new eigenvalue problem and determine a new set of coefficients $C^{(2)}$.

10. The process repeats itself several times, until there is convergence in the electronic energy of the ground state and finally the coefficient matrix C and the eigenvalues $\mathcal{E}_i$ that describe the molecular orbitals are obtained.

The electronic energy, which is the convergence parameter, is calculated by:

$$\mathcal{E}_0 = \frac{1}{2}\sum_{\mu}\sum_{\nu} P_{\mu\nu}(T_{\mu\nu} + V_{\mu\nu}^{nuc} + F_{\mu\nu}). \tag{A.21}$$

Appendix

B Natural Transitions Orbitals of Sevoflurane Molecule

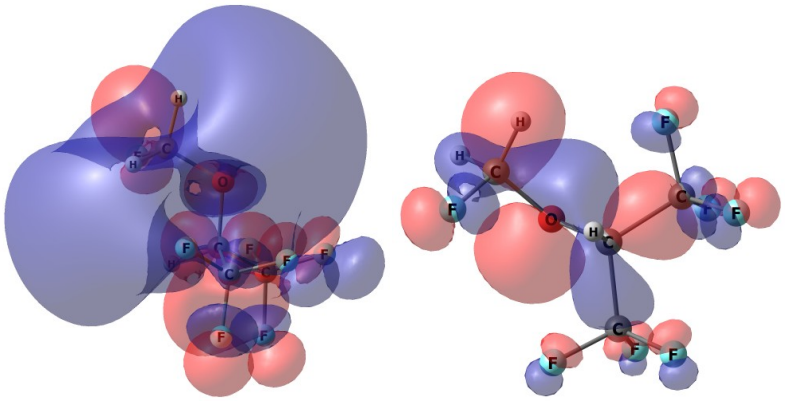

(a) $3s/\sigma^*$ (b) HOMO

Figure B.1: $1^3A: 3s/\sigma^* \leftarrow HOMO$

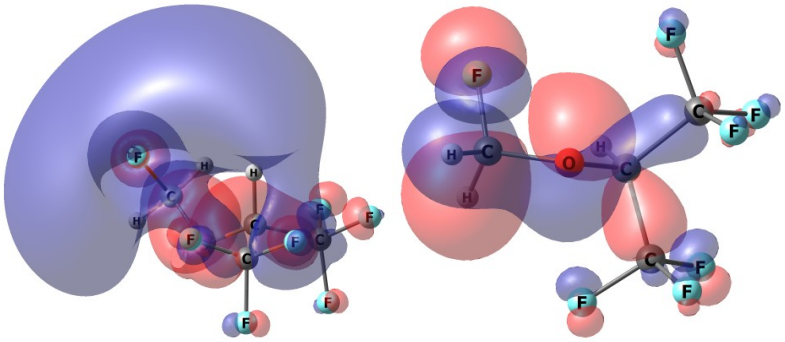

(a) $3p$ (b) HOMO

Figure B.2: $2^3A: 3p \leftarrow HOMO$

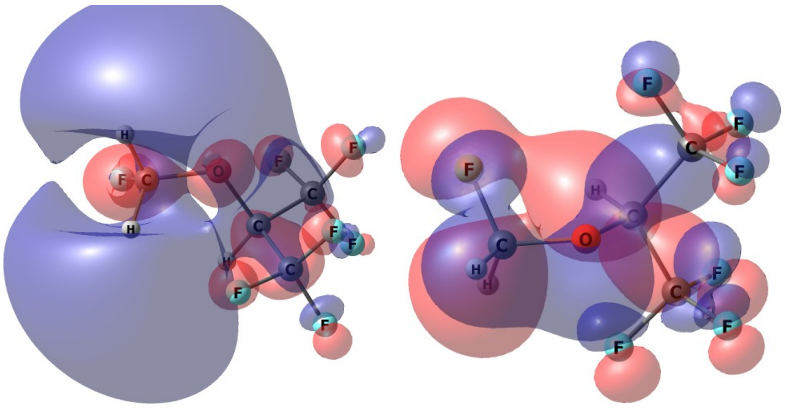

(a) $\sigma^*(C-Cl)$ (b) HOMO

Figure B.3: $3^1A: 3s/\sigma^* \leftarrow HOMO$

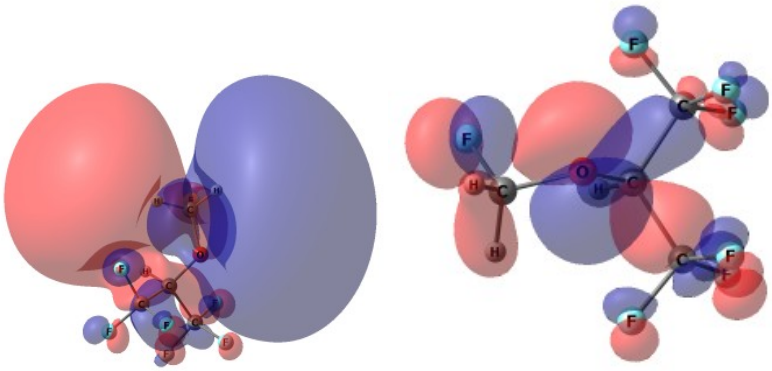

(a) $3p$ (b) HOMO

Figure B.4: $4^3A: 3p \leftarrow HOMO$

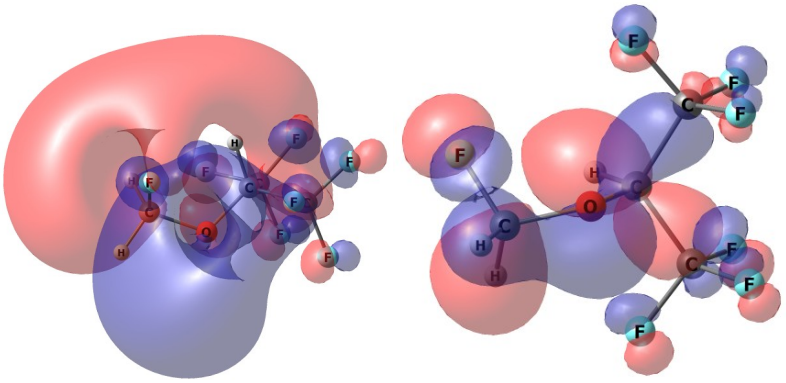

(a) $3p$ (b) HOMO-4

Figure B.5: $5^1A: 3p \leftarrow HOMO$

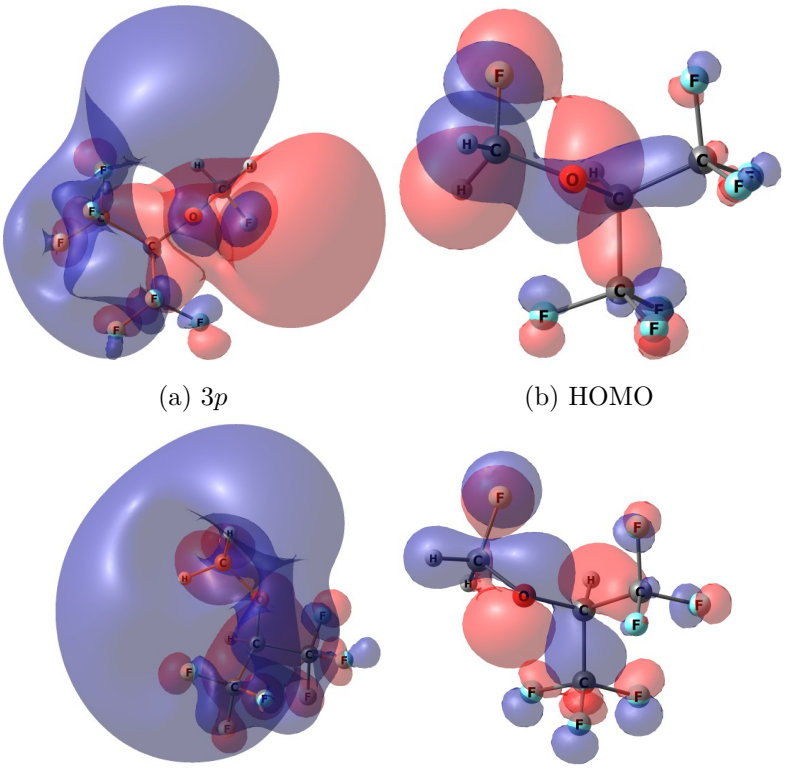

(a) $3p$ (b) HOMO

(c) $3s/\sigma^(C-O)$ (d) HOMO

Figure B.6: $6^3A: 3p \leftarrow HOMO$
$+3s/\sigma^* \leftarrow HOMO-1$

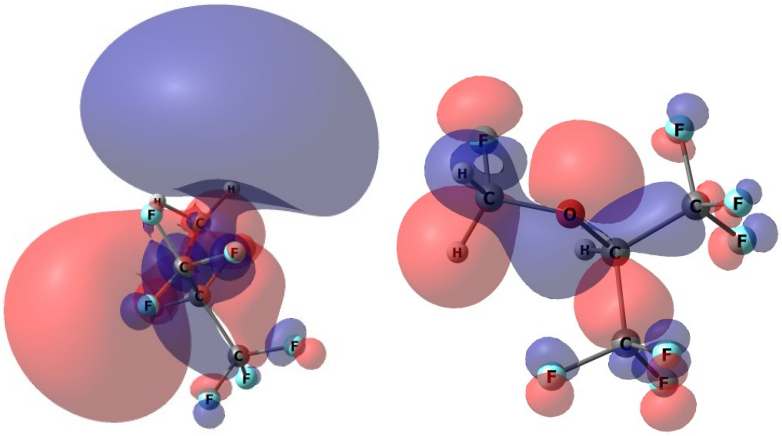

(a) $3p$ (b) HOMO

Figure B.7: $7^1A: 3p \leftarrow HOMO$

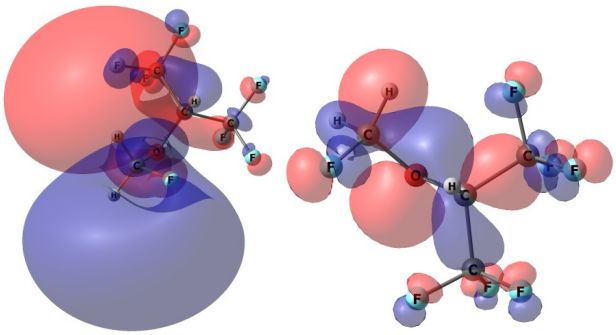

(a) $3p$ (b) HOMO

Figure B.8: $8^3A: 3p \leftarrow HOMO$

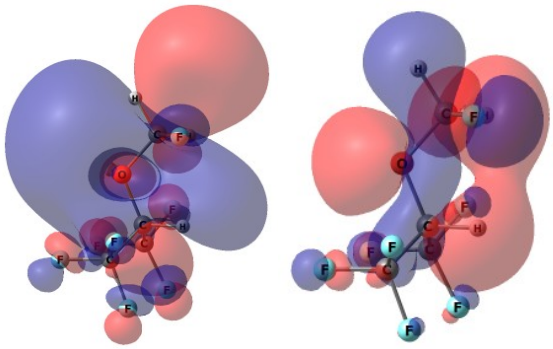

(a) $3d$ (b) HOMO

Figure B.9: $9^3A: 3d \leftarrow HOMO$

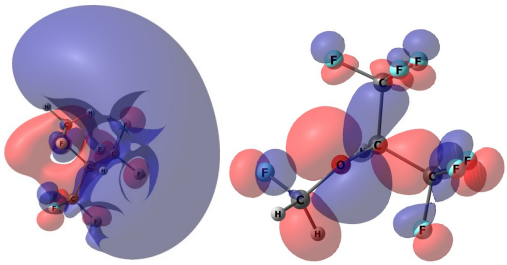

(a) $3p$ (b) HOMO

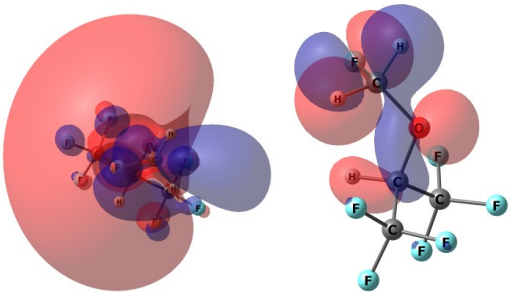

(c) $3s/\sigma^*$ (d) HOMO

Figure B.10: $10^1A: 3p \leftarrow HOMO$
$+3s/\sigma^* \leftarrow HOMO-1$

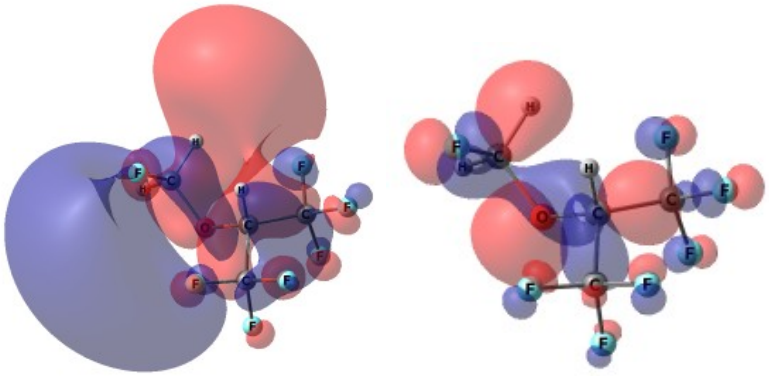

(a) $3p$ (b) HOMO

Figure B.11: $11^1A: 3p \leftarrow HOMO$

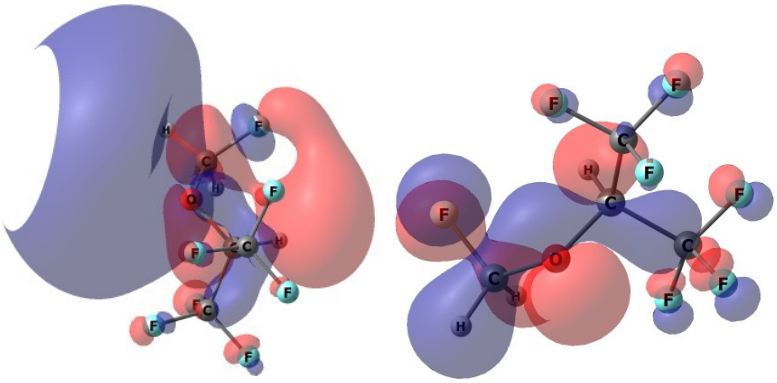

(a) $3p$ (b) HOMO-1

Figure B.12: $12^3A: 3p \leftarrow HOMO-1$

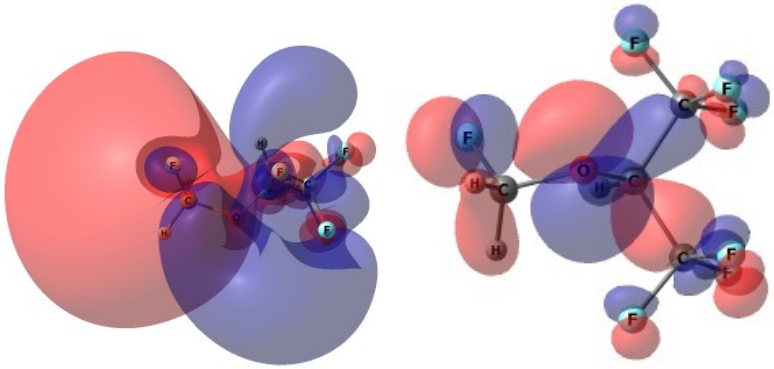

(a) $3d$ (b) HOMO

Figure B.13: $13^3A: 3d \leftarrow HOMO$

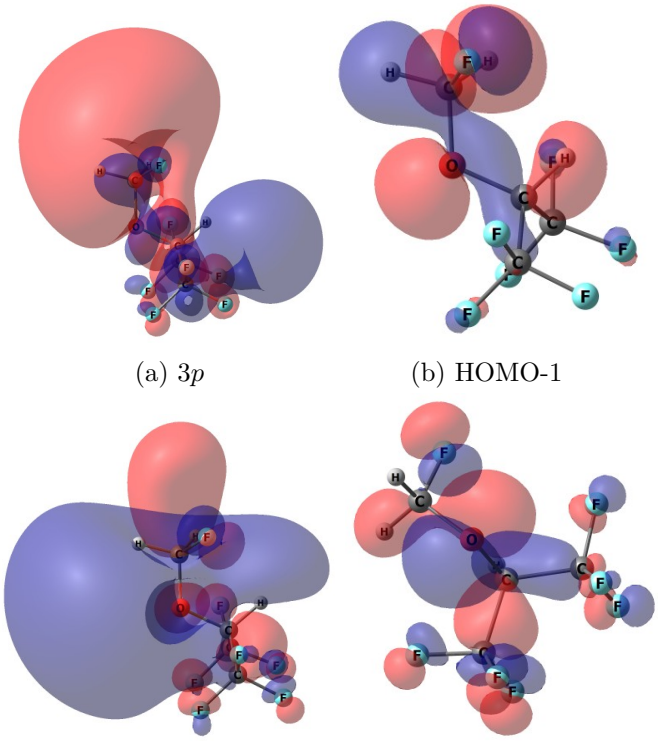

(a) $3p$ (b) HOMO-1

(c) $3d$ (d) HOMO

Figure B.14: $14^1A: 3p \leftarrow HOMO$
$+\,3p \leftarrow HOMO-1$

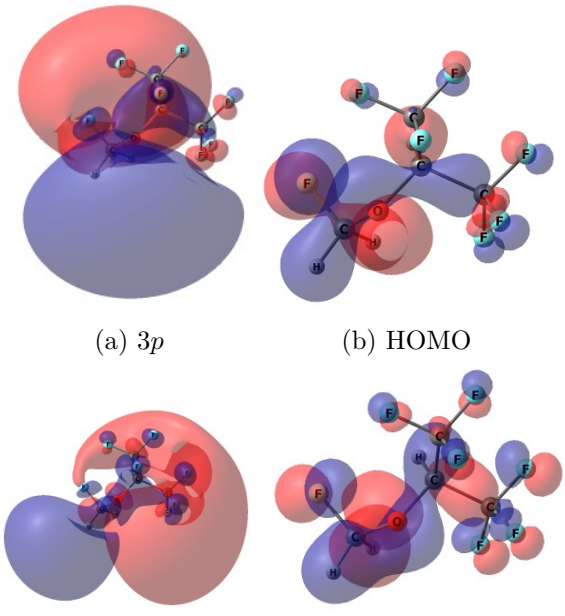

(a) $3p$ (b) HOMO

(c) $3p$ (d) HOMO-1

Figure B.15: $15^1A: 3p \leftarrow HOMO$
$+\,3p \leftarrow HOMO-1$

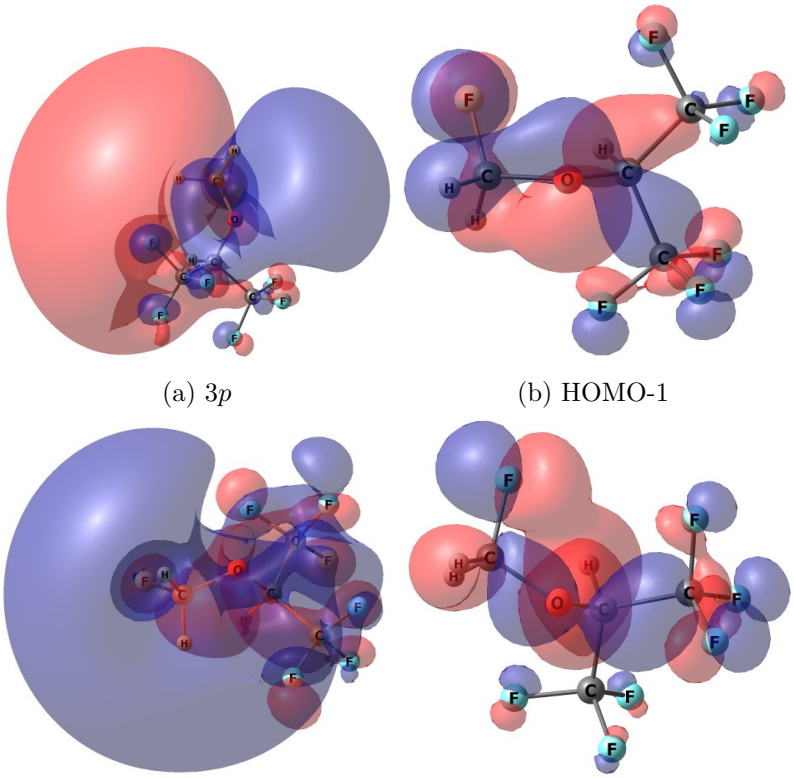

(a) $3p$ (b) HOMO-1

(c) $3s/\sigma^*$ (d) HOMO-3

Figure B.16: $16^1A: 3p \leftarrow HOMO$
$+3s/\sigma^* \leftarrow HOMO-3$

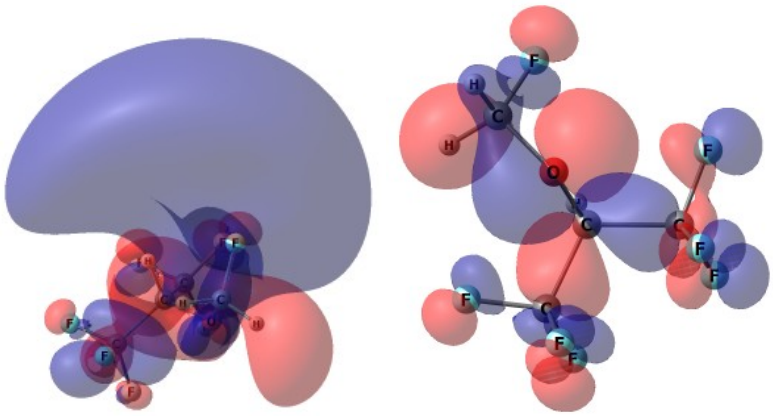

(a) $4s$ (b) HOMO

Figure B.17: $17^31A: 4s \leftarrow HOMO$

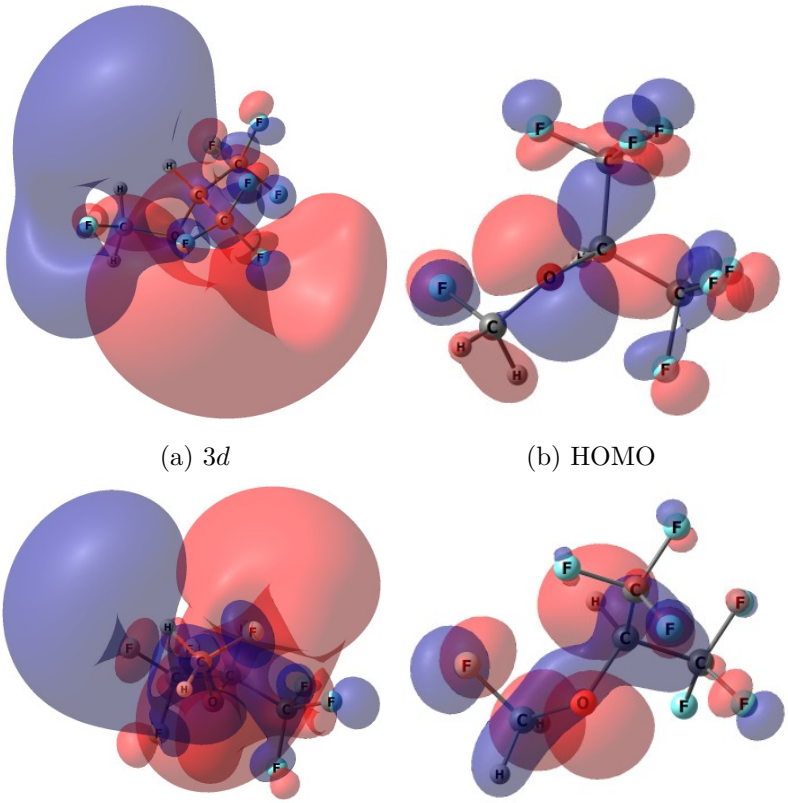

(a) $3d$ (b) HOMO

(c) $3d$ (d) HOMO-1

Figure B.18: $18^3A: 3d \leftarrow HOMO$
$+3d \leftarrow HOMO-1$

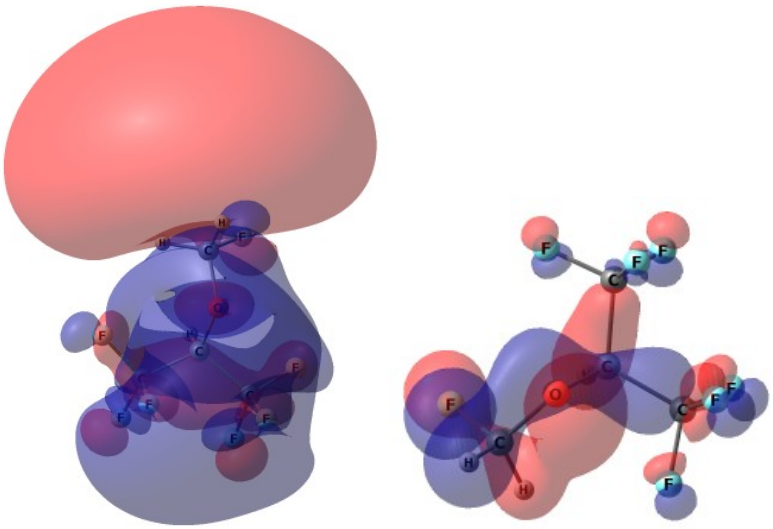

(a) $3p$ (b) HOMO

Figure B.19: $19^1A: 3p \leftarrow HOMO$

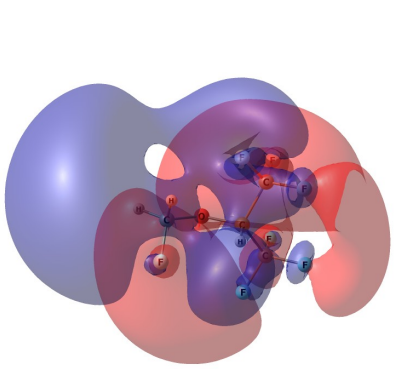

(a) $3d$

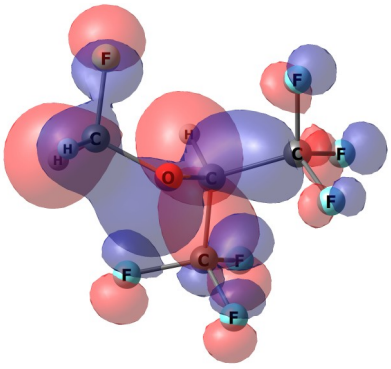

(b) HOMO

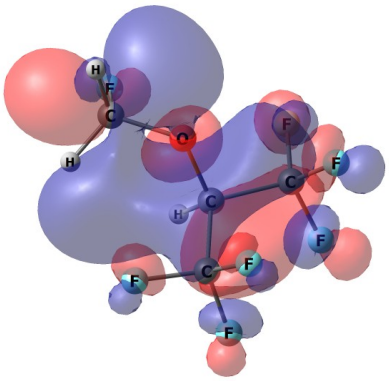

(c) σ^*

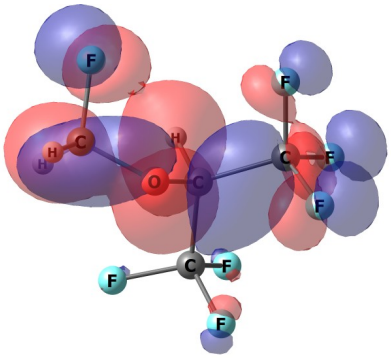

(d) HOMO-2

Figure B.20: $20^3A: \ 3d \leftarrow HOMO$
$+\sigma^* \ \leftarrow HOMO-2$

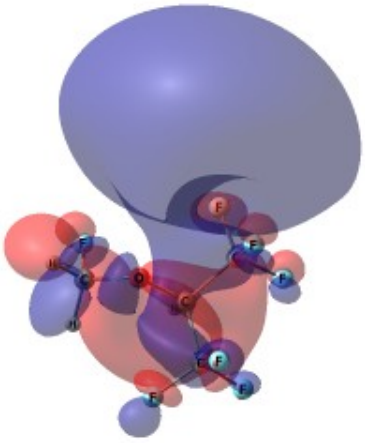

(a) $3d$

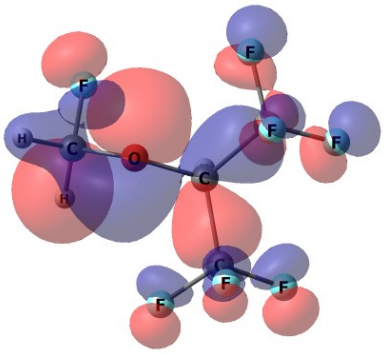

(b) HOMO

Figure B.21: $21^1A: \ 3d \leftarrow HOMO$

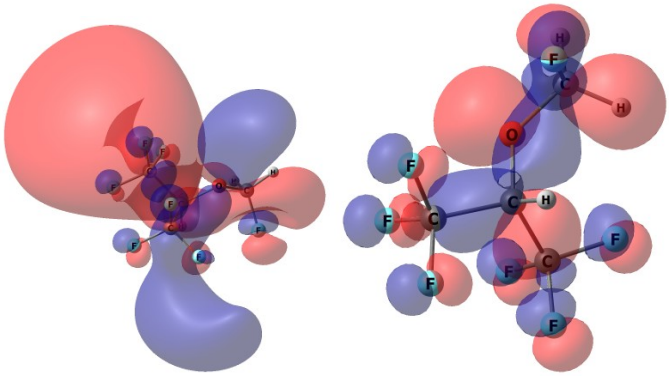

(a) $3d$ (b) HOMO

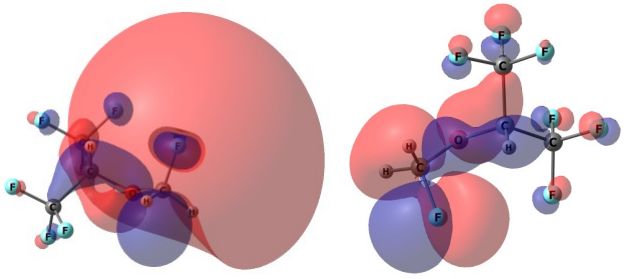

(c) $3s/\sigma^*$ (d) HOMO-3

Figure B.22: $22^3A: 3d \leftarrow HOMO$
$+\,3s/\sigma^* \leftarrow HOMO-3$

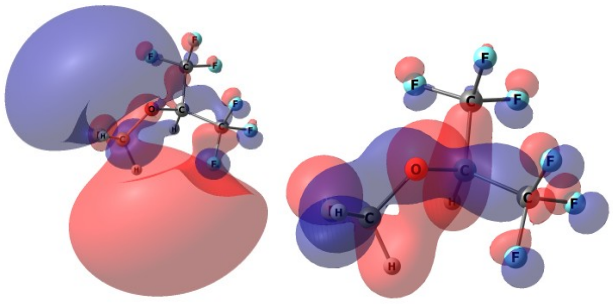

(a) $3d$ (b) HOMO

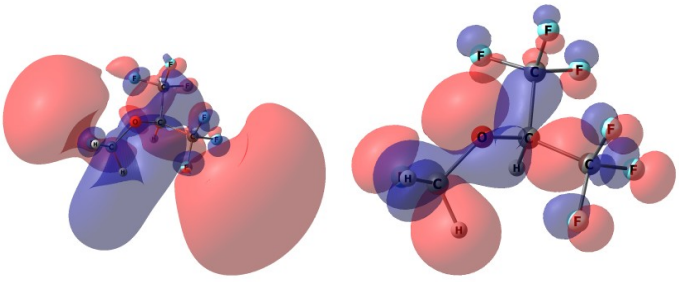

(c) $3p$ (d) HOMO-1

Figure B.23: $23^1A: 3d \leftarrow HOMO$
$+\,3p \leftarrow HOMO-1$

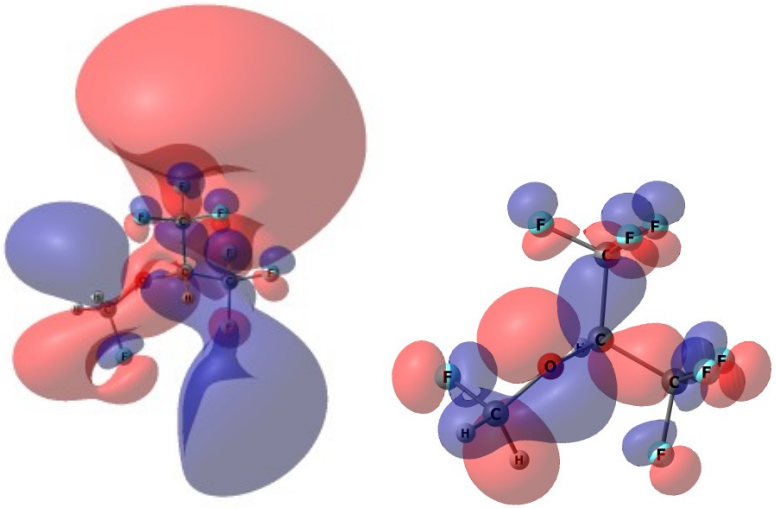

(a) $3d$ (b) HOMO

(c) $3s/\sigma^*$ (d) HOMO-3

Figure B.24: $24^3A: 3d \leftarrow HOMO$
$+\,3s/\sigma^* \leftarrow HOMO-3$

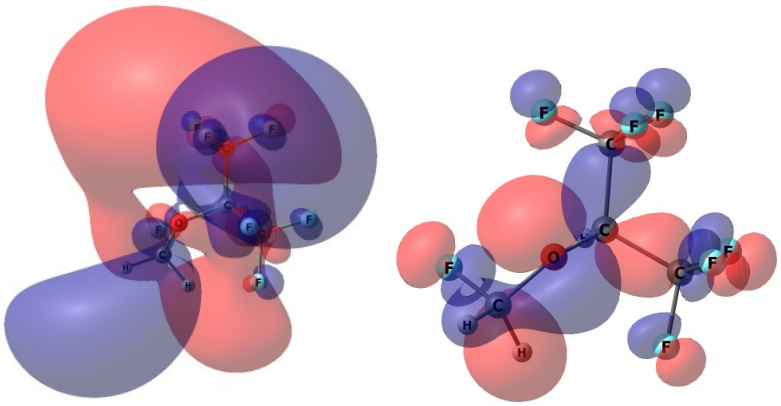

(a) $3d$ (b) HOMO

Figure B.25: $25^1A: 3d \leftarrow HOMO$

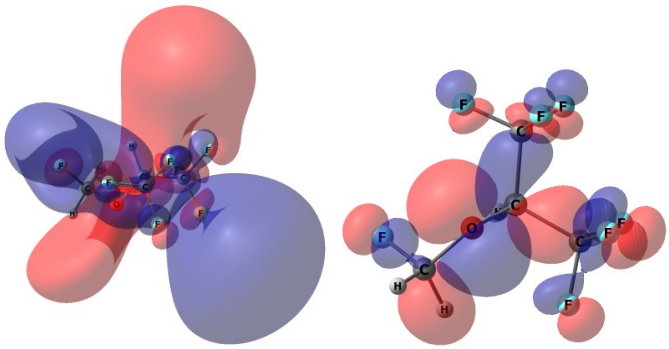

(a) $4p$ (b) HOMO

Figure B.26: $26^3A: 4p \leftarrow HOMO$

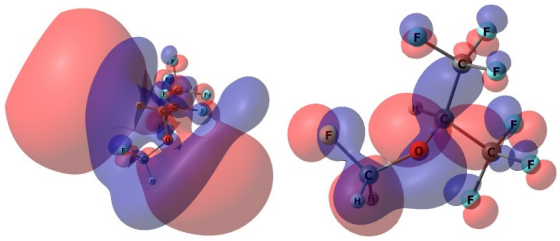

(a) $3d$ (b) HOMO

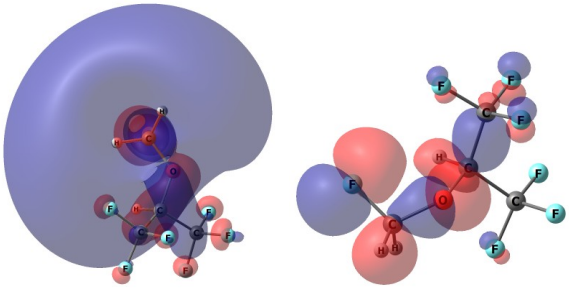

(c) $3s/\sigma^*$ (d) HOMO-3

Figure B.27: $27^1A: 3d \leftarrow HOMO$
$+\,3s/\sigma^* \leftarrow HOMO-3$

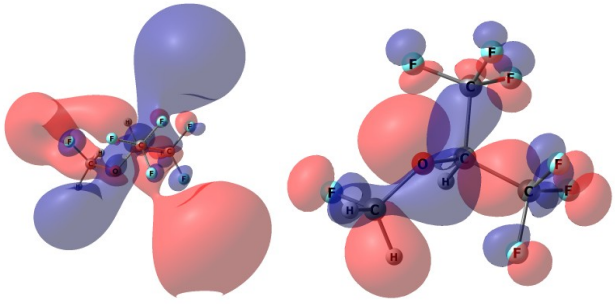

(a) $3d$ (b) HOMO

Figure B.28: $28^1A: 3d \leftarrow HOMO$

Appendix

C Natural Transitions Orbitals of Isoflurane Molecule

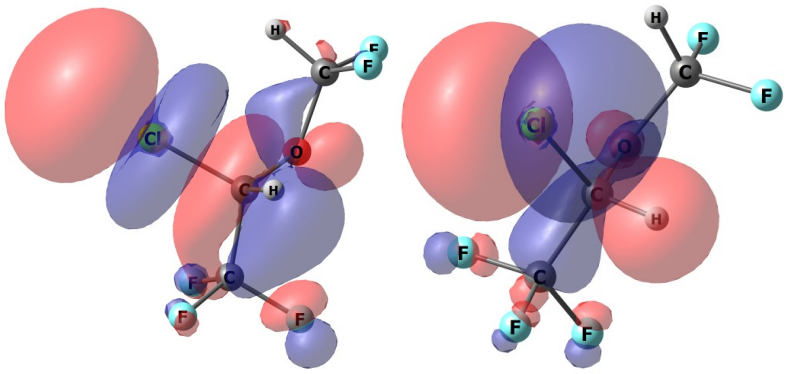

(a) $\sigma^*(C-Cl)$ (b) HOMO

Figure C.1: $1^3A: \sigma^*(C-Cl) \leftarrow HOMO$

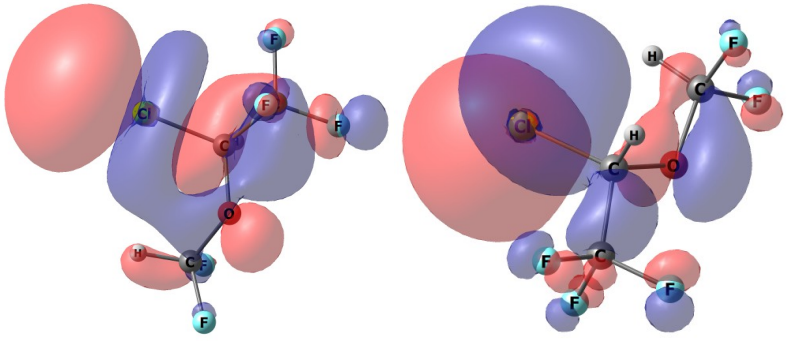

(a) $\sigma^*(C-Cl)$ (b) HOMO-1

Figure C.2: $2^3A: \sigma^*(C-Cl) \leftarrow HOMO-1$

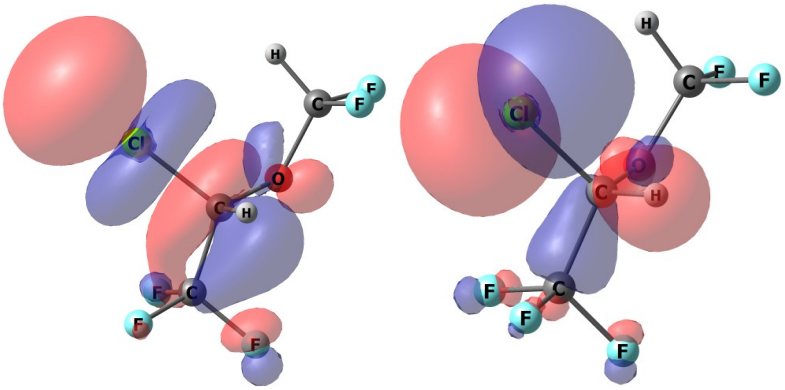

(a) $\sigma^*(C-Cl)$ (b) HOMO

Figure C.3: $3^1A: \sigma^*(C-Cl) \leftarrow HOMO$

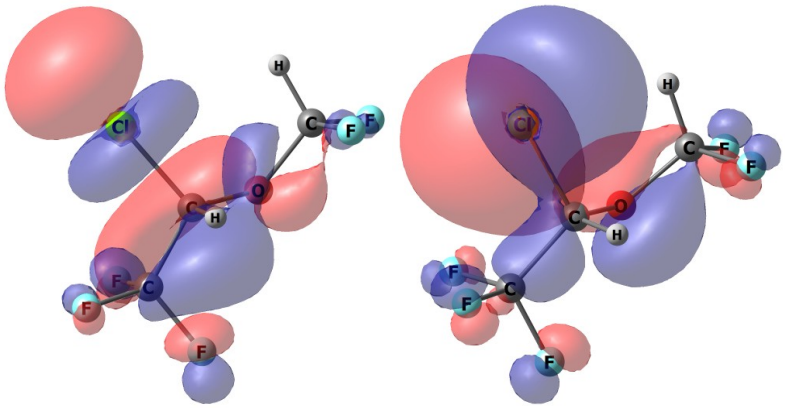

(a) $\sigma^*(C-Cl)$ (b) HOMO-1

Figure C.4: $4^1A: \sigma^*(C-Cl) \leftarrow HOMO-1$

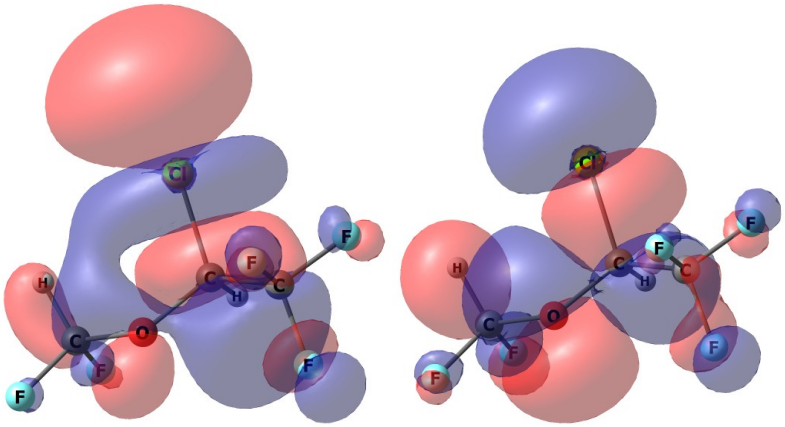

(a) $\sigma^*(C-Cl)$ (b) HOMO-4

Figure C.5: $5^3A: \sigma^*(C-Cl) \leftarrow HOMO-4$

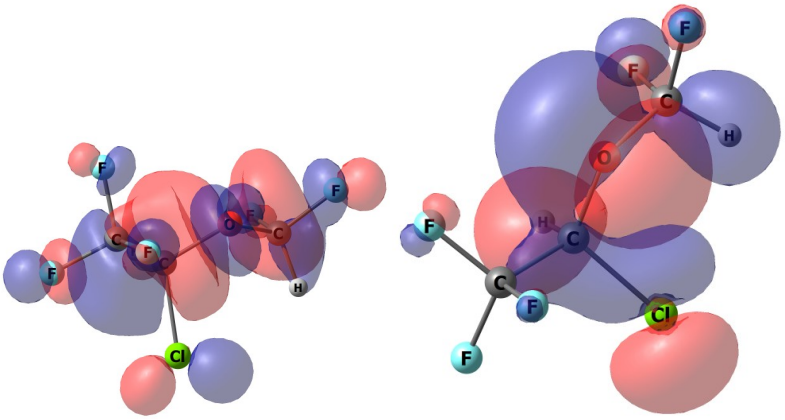

(a) $\sigma^*(C-O)$ (b) HOMO-2

Figure C.6: $6^3A:\ \sigma^*(C-O) \leftarrow HOMO-2$

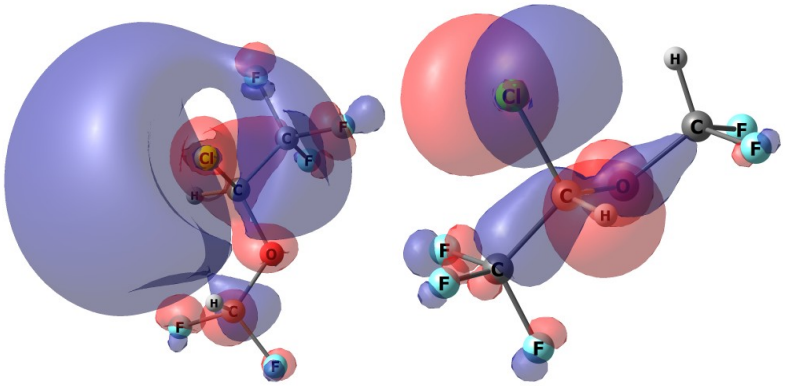

(a) $3s/\sigma^*(C-H)$ (b) HOMO

Figure C.7: $7^3A:\ 3s/\sigma^*(C-H) \leftarrow HOMO$

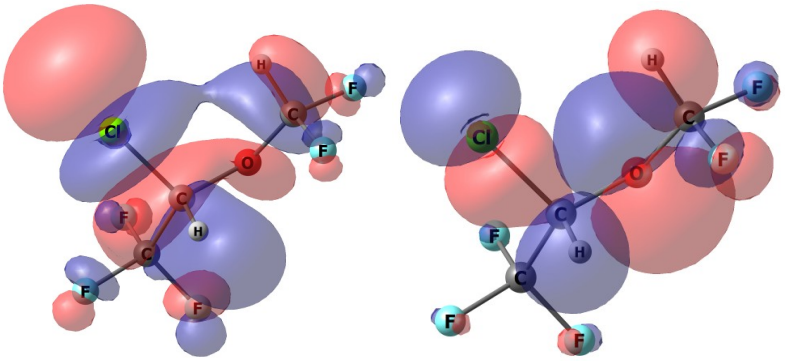

(a) $\sigma^*(C-Cl)$ (b) HOMO-4

Figure C.8: $8^1A:\ \sigma^*(C-Cl) \leftarrow HOMO-4$

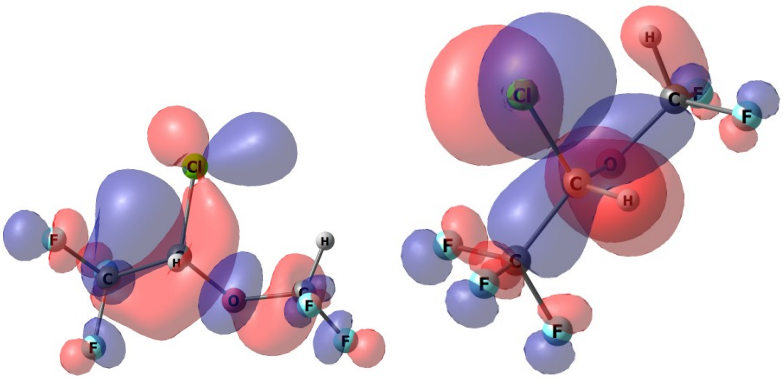

(a) $\sigma^*(C-O)$ (b) HOMO

Figure C.9: $9^3A: \sigma^*(C-O) \leftarrow HOMO$

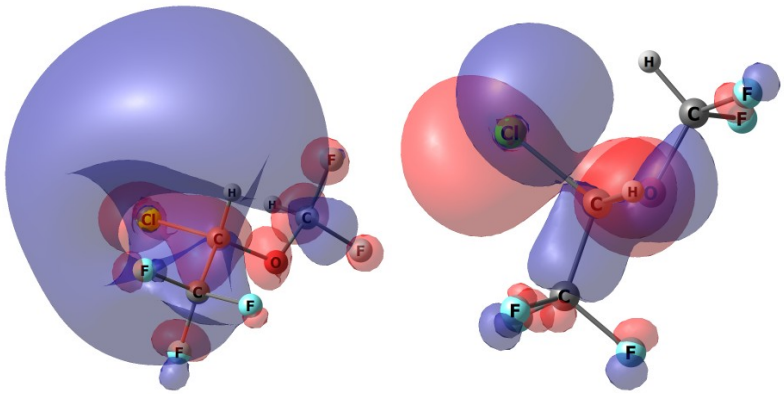

(a) $3s/\sigma^*(C-H)$ (b) HOMO

Figure C.10: $10^1A: 3s/\sigma^* \leftarrow HOMO(C-H)$

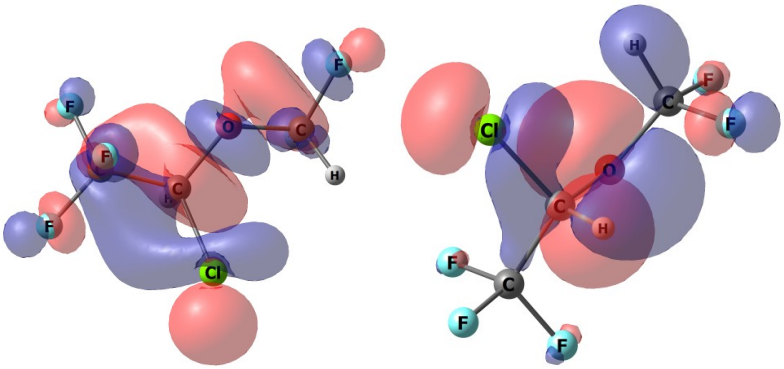

(a) $\sigma^*(C-O)$ (b) HOMO-4

Figure C.11: $11^1A: \sigma^*(C-O) \leftarrow HOMO-4$

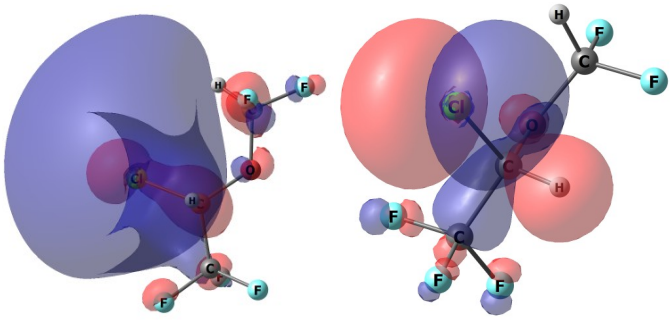

(a) $3s/\sigma^*(C-Cl)$ (b) HOMO

Figure C.12: $12^3A:\ 3s/\sigma^*(C-Cl) \leftarrow HOMO$

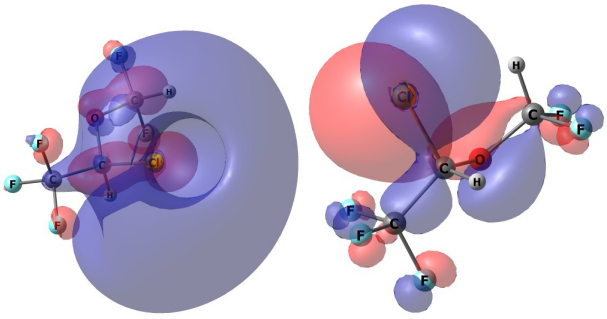

(a) $3s/\sigma^*(C-Cl)$ (b) HOMO

Figure C.13: $13^1A:\ 3s/\sigma^*(C-Cl) \leftarrow HOMO$

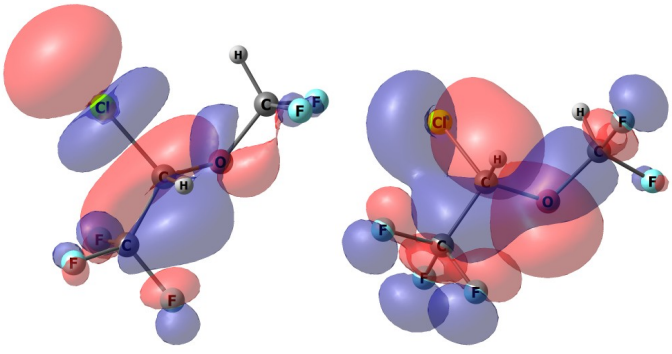

(a) $\sigma^*(C-Cl)$ (b) HOMO-3

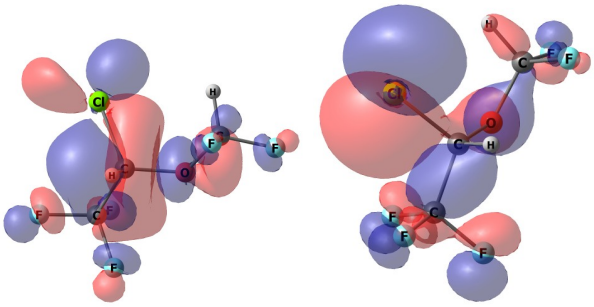

(c) $\sigma^(C-O)$ (d) HOMO

Figure C.14: $14^3A:\ \sigma^*(C-Cl) \leftarrow HOMO-3$
$+\sigma^*(C-O) \leftarrow HOMO$

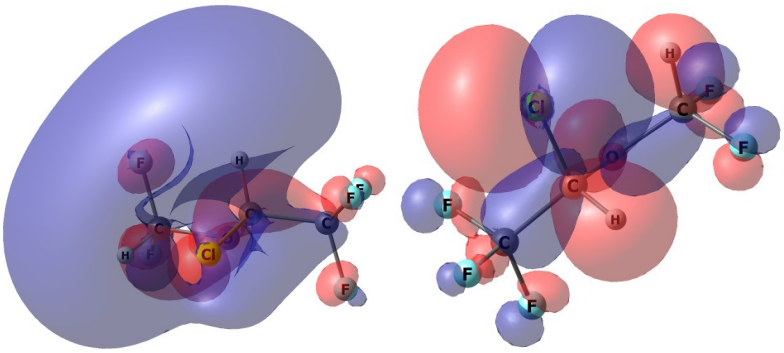

(a) $3s/\sigma^*$ (b) HOMO-1

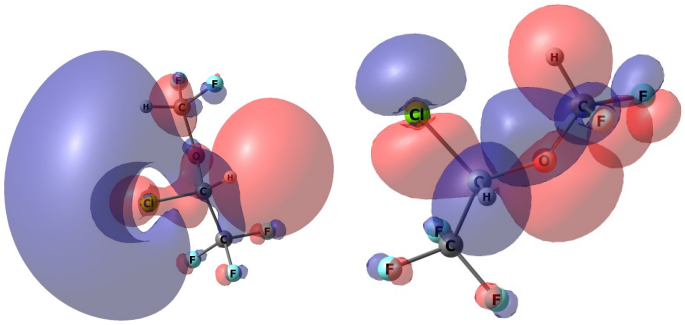

(c) $3s/\sigma^(C-O)$ (d) HOMO-2

Figure C.15: $15^3A: 3s/\sigma^* \leftarrow HOMO-1$
$+3s/\sigma^*(C-O) \leftarrow HOMO-2$

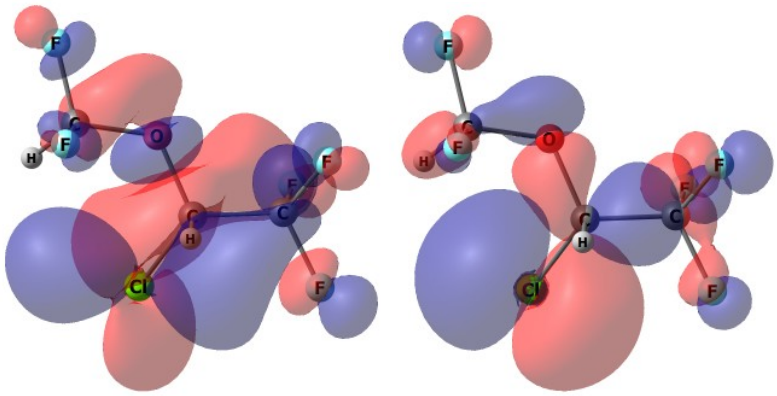

(a) $\sigma^*(C-O)$ (b) HOMO

Figure C.16: $16^3A: \sigma^*(C-O) \leftarrow HOMO$

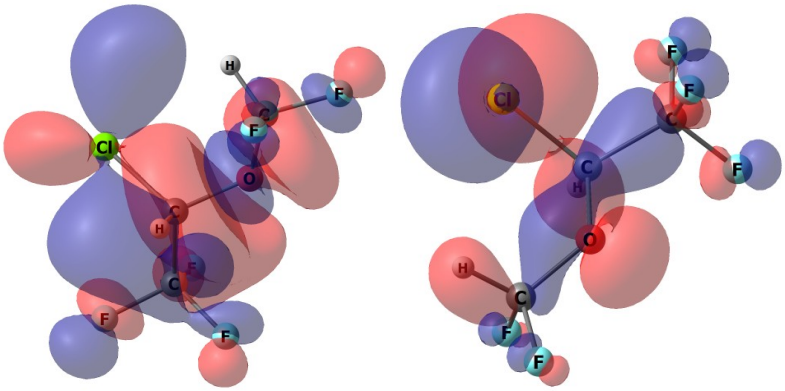

(a) $\sigma^*(C-O)$ (b) HOMO

Figure C.17: $17^1A:\ \sigma^*(C-O) \leftarrow HOMO$

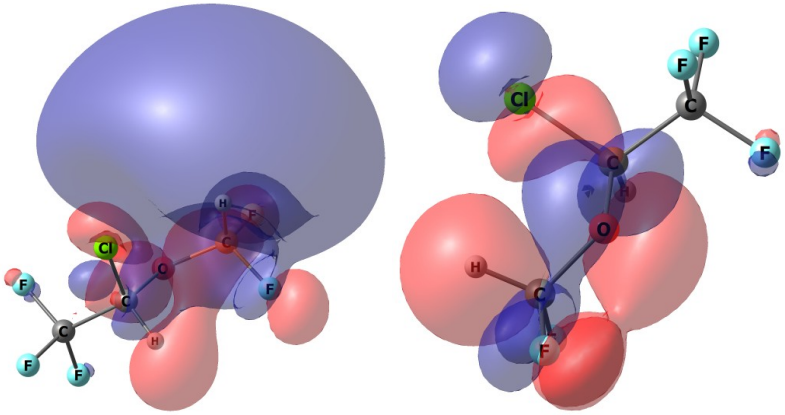

(a) $3s/\sigma^*$ (b) HOMO-4

Figure C.18: $18^3A:\ 3s/\sigma^* \leftarrow HOMO-4$

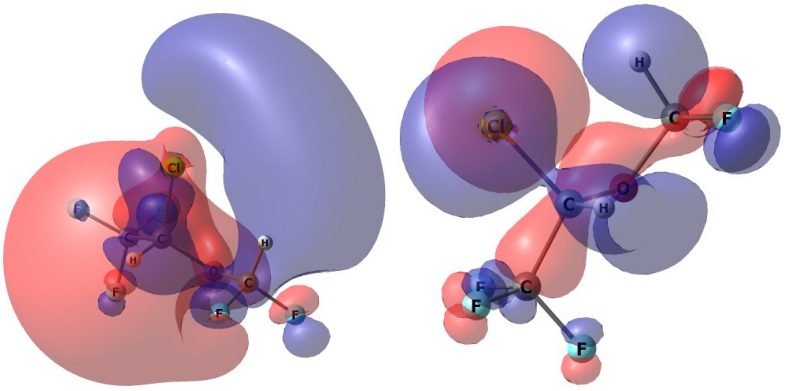

(a) $3p$ (b) HOMO

Figure C.19: $19^3A:\ 3p \leftarrow HOMO$

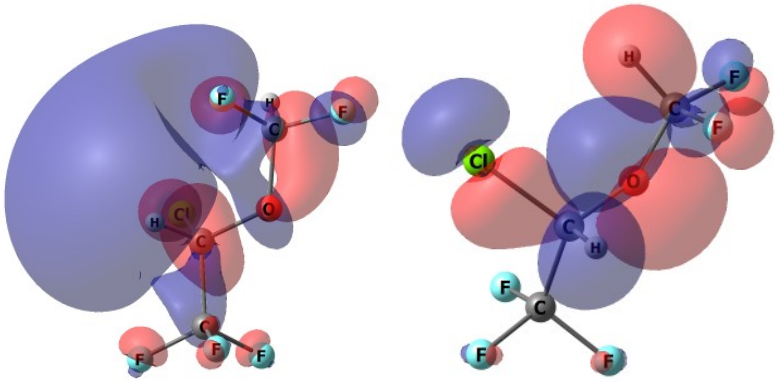

(a) $3s/\sigma^*$ (b) HOMO-4

Figure C.20: $20^1A: 3s/\sigma^*(C-O) \leftarrow HOMO-4$

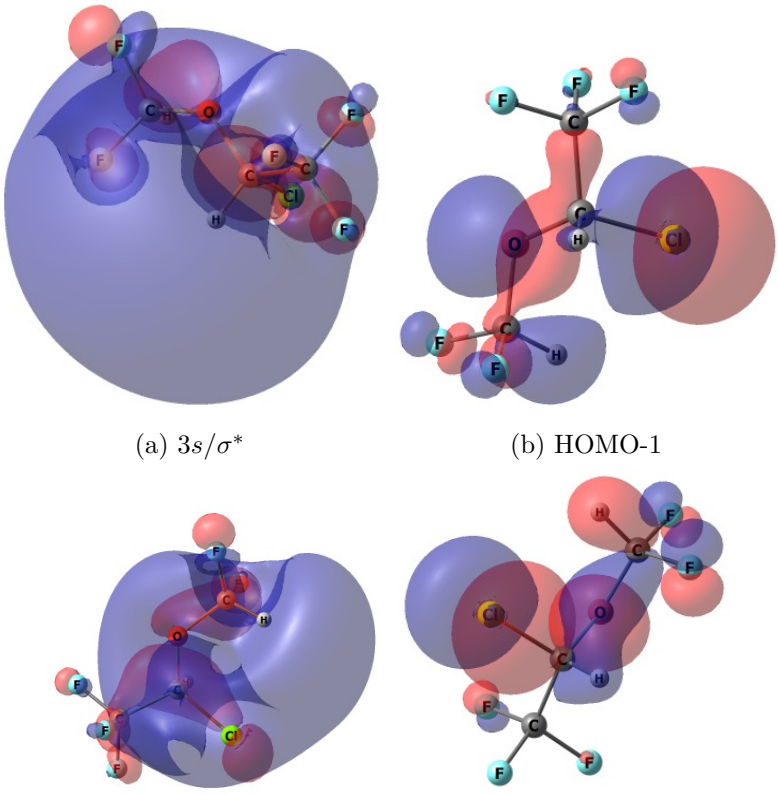

(a) $3s/\sigma^*$ (b) HOMO-1

(c) $3s/\sigma^(C-O)$ (d) HOMO-2

Figure C.21: $21^3A: 3s/\sigma^* \leftarrow HOMO-1$
$+3s/\sigma^*(C-O) \leftarrow HOMO-2$

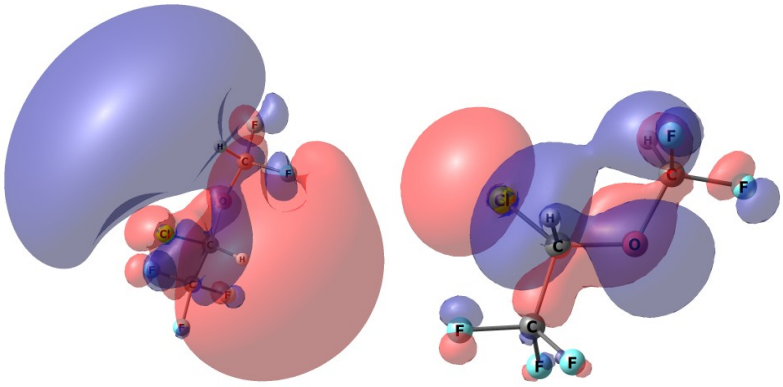

(a) $3p$ (b) HOMO-1

Figure C.22: $22^1A: 3p \leftarrow HOMO-1$

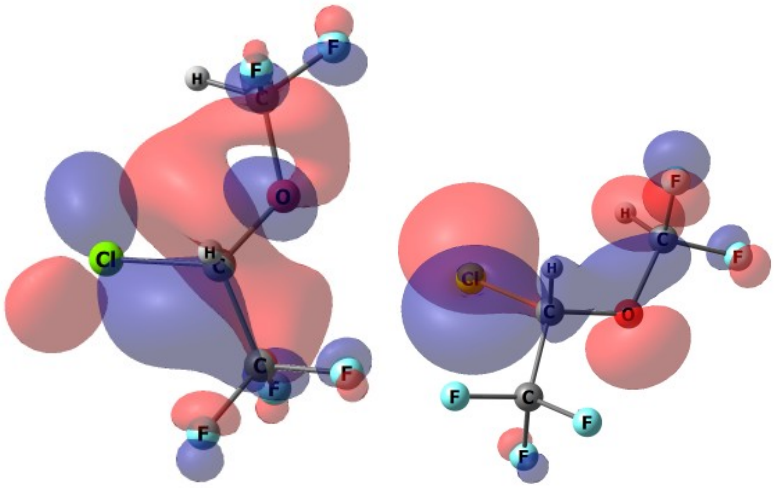

(a) σ^* (b) HOMO-4

Figure C.23: $23^3A: \sigma^*(C-O) \leftarrow HOMO-2$

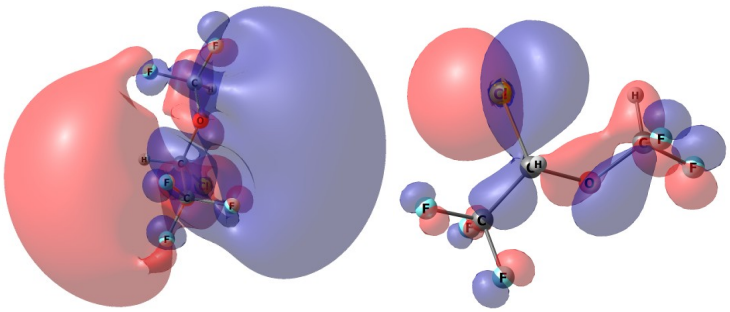

(a) $3p/\sigma^*$ (b) HOMO-1

Figure C.24: $24^3A: 3p/\sigma^*(C-O) \leftarrow HOMO-1$

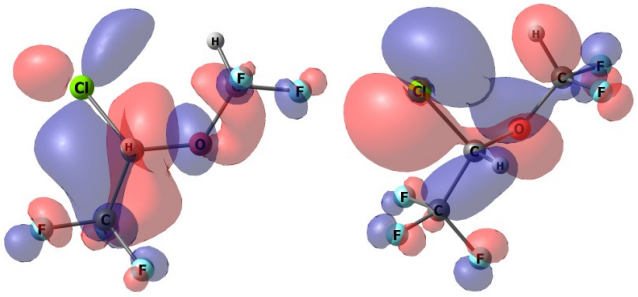

(a) σ^* (b) HOMO-2

Figure C.25: $25^3A: \sigma^*(C-O) \leftarrow HOMO-2$

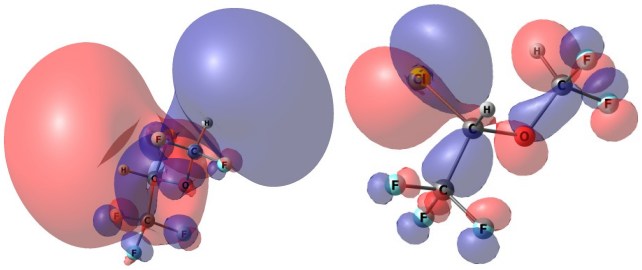

(a) $3p/\sigma^*$ (b) HOMO-2

Figure C.26: $26^1A: 3p/\sigma^*(C-O) \leftarrow HOMO-2$

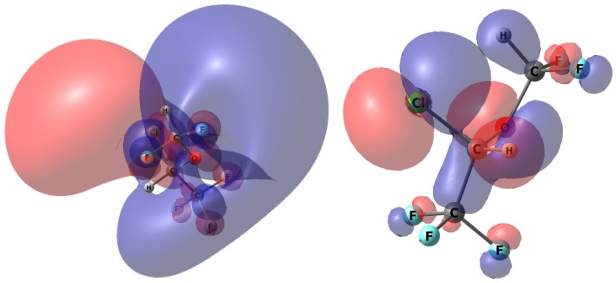

(a) $3p$ (b) HOMO-1

Figure C.27: $27^3A: 3p \leftarrow HOMO-1$

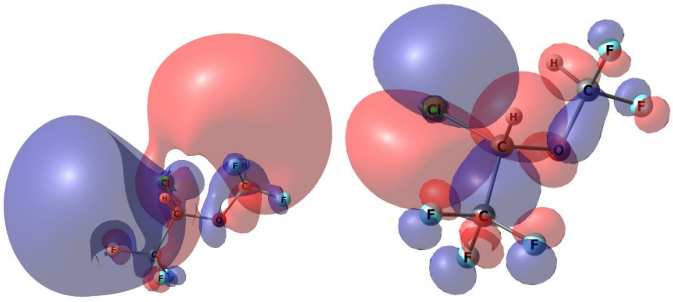

(a) $3p$ (b) HOMO-3

Figure C.28: $28^3A: 3p \leftarrow HOMO-3$

Appendix

D Natural Transitions Orbitals of Methanol Molecule

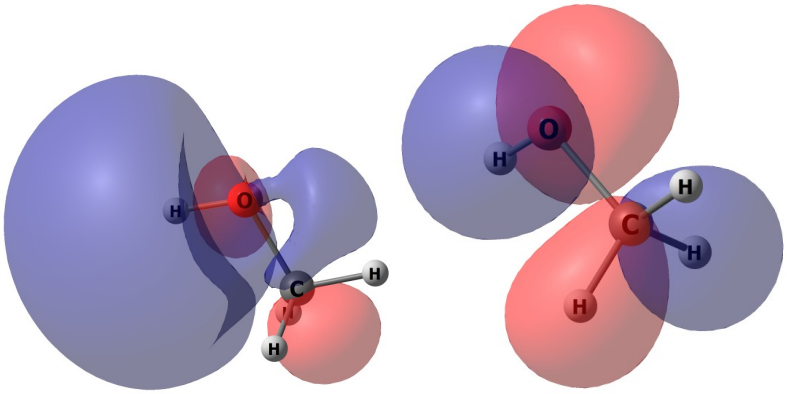

(a) $3s/\sigma^*(O-H)$ (b) $HOMO(2a'')$

Figure D.1: $1^3A'' : 3s/\sigma^*(O-H) \leftarrow HOMO\,(2a'')$

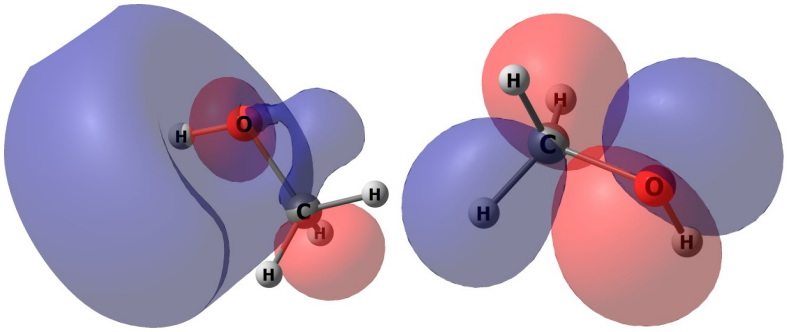

(a) $3s/\sigma^*(O-H)$ (b) $HOMO(2a'')$

Figure D.2: $2^1A'' : 3s/\sigma^*(O-H) \leftarrow HOMO\,(2a'')$

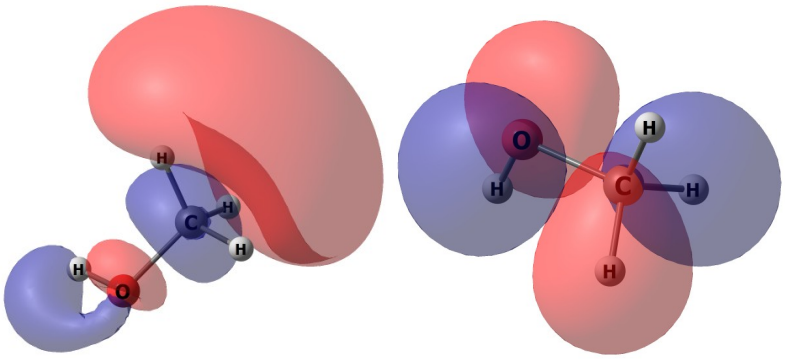

(a) $3p\sigma$ (b) $HOMO(2a'')$

Figure D.3: $3^3A' : 3p\sigma \leftarrow HOMO\,(2a'')$

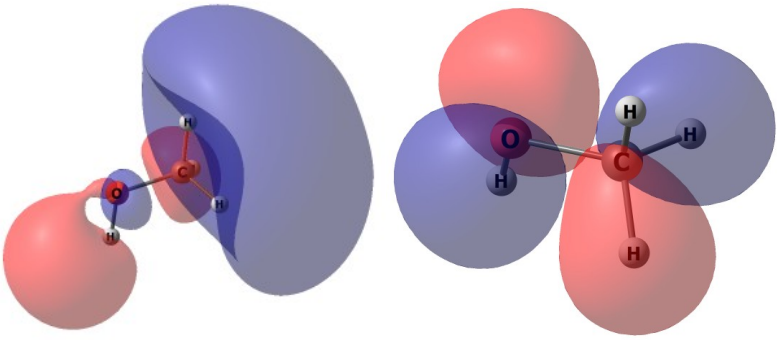

(a) $3p\sigma$ (b) $HOMO(2a'')$

Figure D.4: $4^1A'' : 3p\sigma \leftarrow HOMO\,(2a'')$

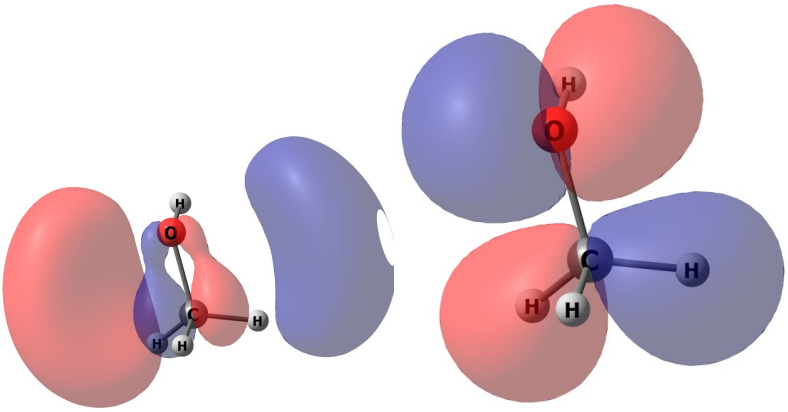

(a) $3p\pi$ (b) $HOMO(2a'')$

Figure D.5: $5^3A' : 3p\pi \leftarrow HOMO\,(2a'')$

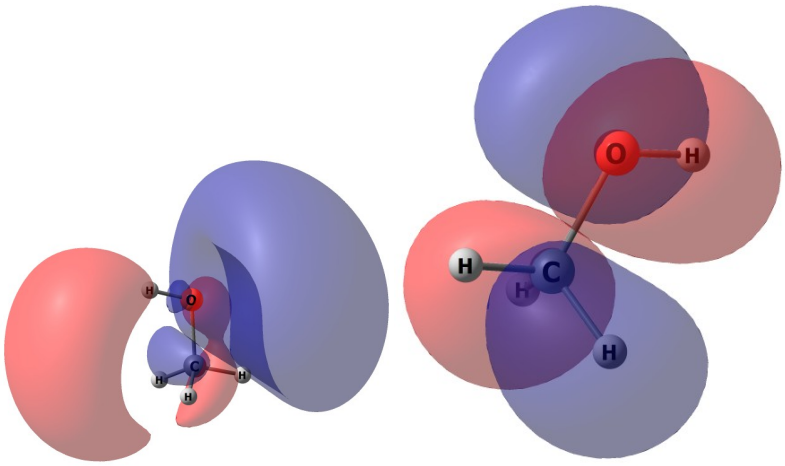

(a) $3p\sigma'$ (b) $HOMO(2a'')$

Figure D.6: $6^3A'' : 3p\sigma' \leftarrow HOMO\,(2a'')$

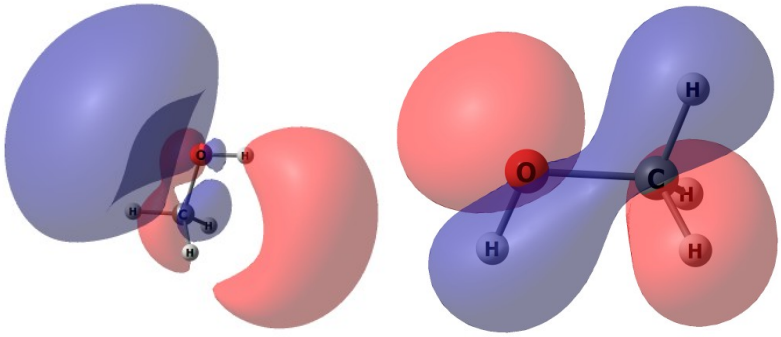

(a) $3s/\sigma^*(O-H)$ (b) $HOMO-1(7a')$

Figure D.7: $7^3A' : 3s/\sigma^*(O-H) \leftarrow HOMO-1\,(7a')$

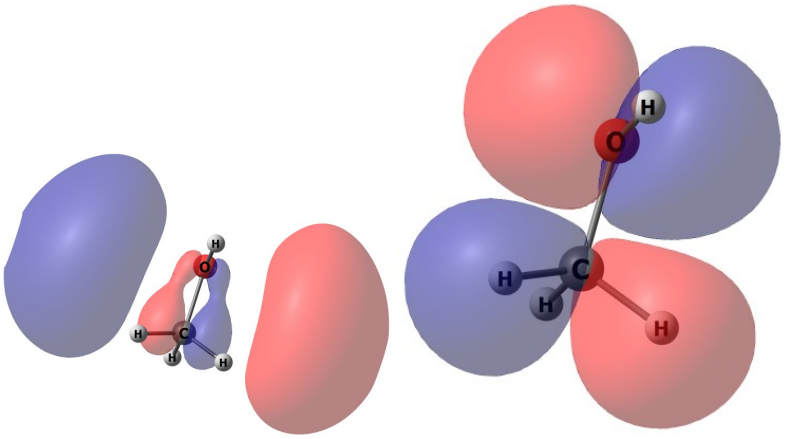

(a) $3p\pi$ (b) $HOMO(2a'')$

Figure D.8: $8^1A' : 3p/\pi \leftarrow HOMO\,(2a'')$

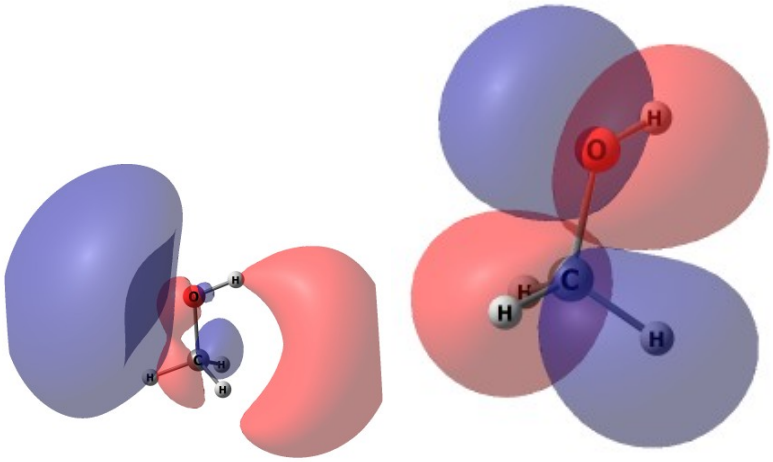

(a) $3p\sigma'$ (b) $HOMO(2a'')$

Figure D.9: $9^1A' : 3p\sigma \leftarrow HOMO\,(2a'')$

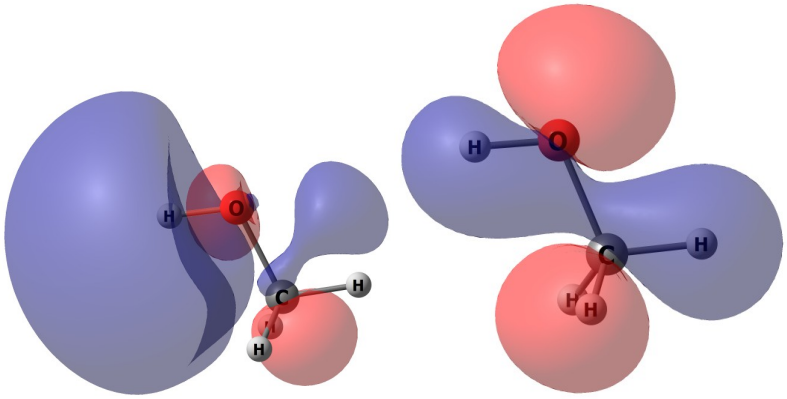

(a) $3s/\sigma^*(O-H)$ (b) $HOMO-1(7a')$

Figure D.10: $10^1A' : 3s/\sigma^*(O-H) \leftarrow HOMO-1\,(7a')$

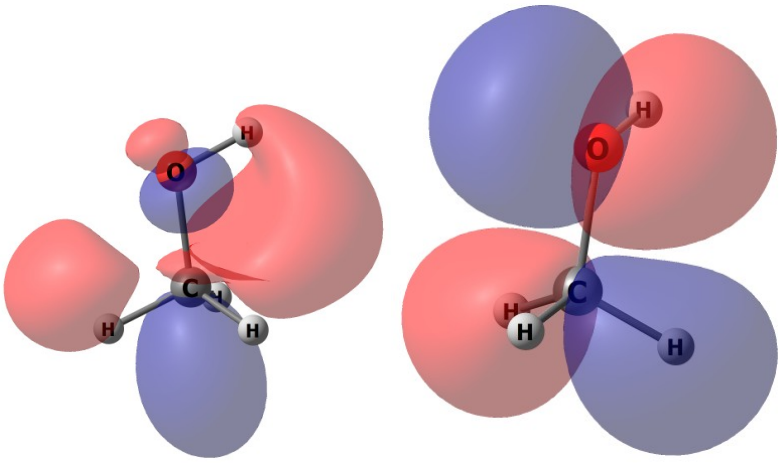

(a) $3d\sigma$ (b) $HOMO(2a'')$

Figure D.11: $11^3A'' : 3d\sigma \leftarrow HOMO\,(2a'')$

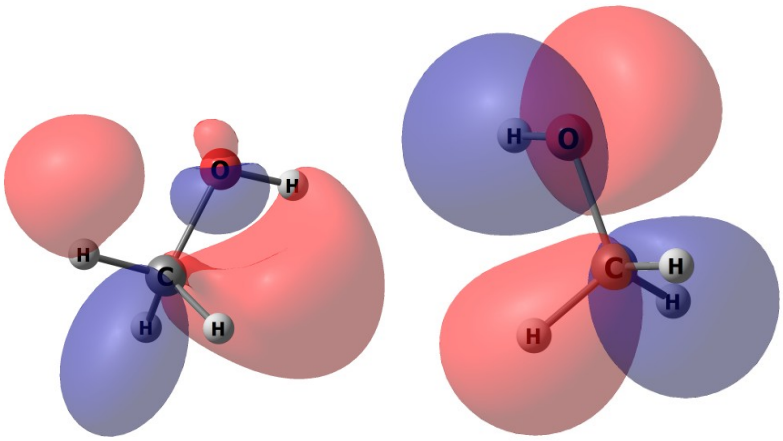

(a) $3d\sigma$ (b) $HOMO(2a'')$

Figure D.12: $12^1A'' : 3d\sigma \leftarrow HOMO\,(2a'')$

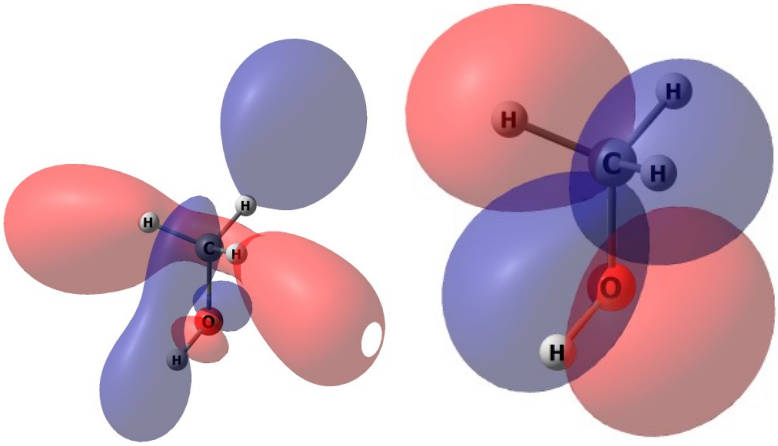

(a) $3d\sigma'$ (b) $HOMO(2a'')$

Figure D.13: $13^3A'' : 3d\sigma' \leftarrow HOMO\,(2a'')$

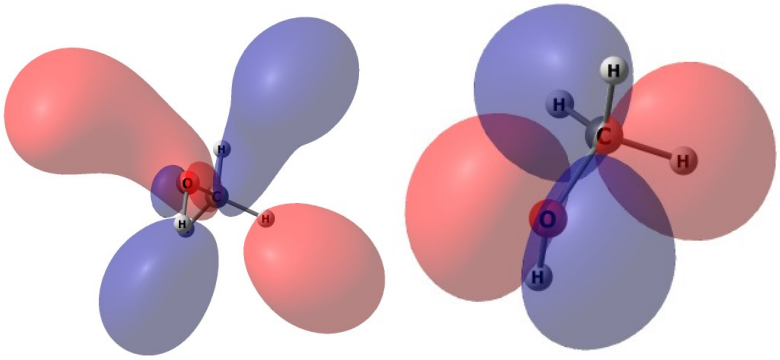

(a) $3d\pi$ (b) $HOMO-1(7a')$

Figure D.14: $14^3A' : 3d\pi \leftarrow HOMO-1\,(7a')$

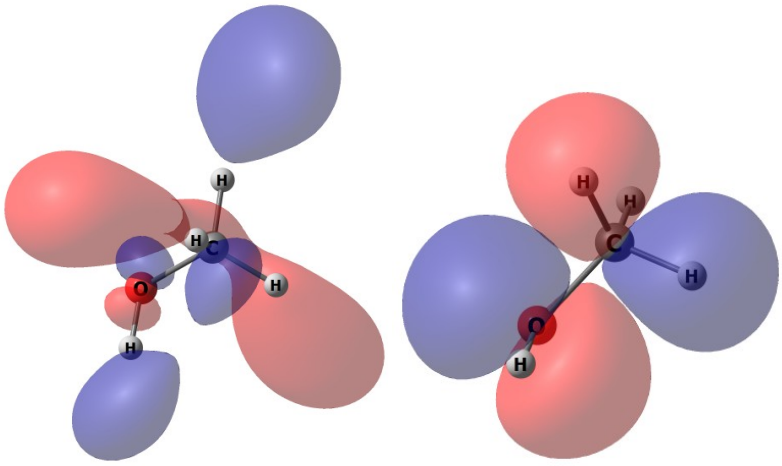

(a) $3d\sigma$ (b) $HOMO(2a'')$

Figure D.15: $15^1A'' : 3d\sigma \leftarrow HOMO\,(2a'')$

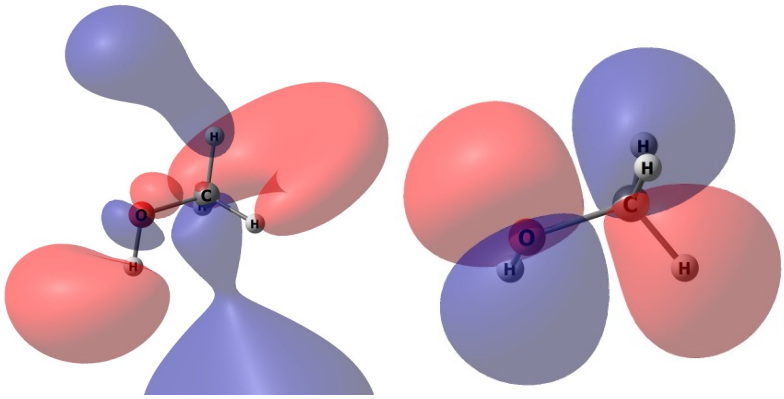

(a) $3d\sigma''$ (b) $HOMO(2a'')$

Figure D.16: $16^3A'' : 3d\sigma'' \leftarrow HOMO\,(2a'')$

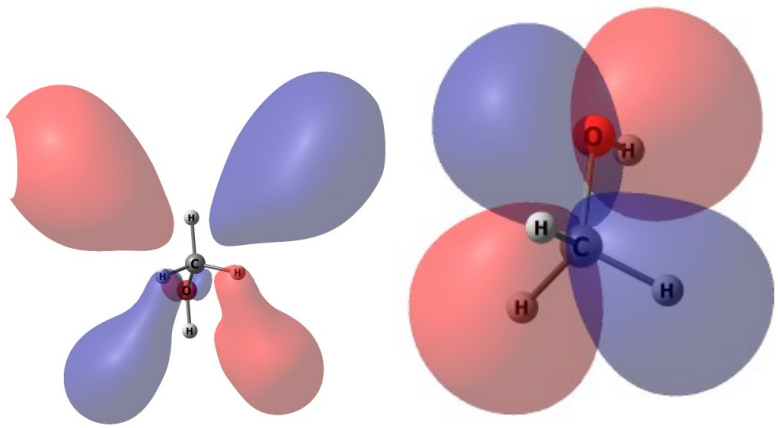

(a) $3d\pi'$ (b) $HOMO(2a'')$

Figure D.17: $17^3A' : 3d\pi' \leftarrow HOMO\,(2a'')$

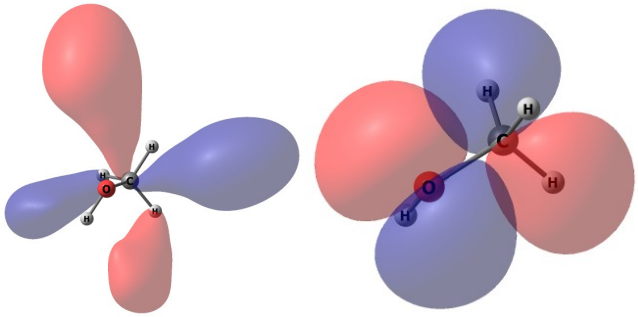

(a) $3d\pi$ (b) $HOMO(2a'')$

Figure D.18: $18^1A'$: $3d\pi \leftarrow HOMO\,(2a'')$

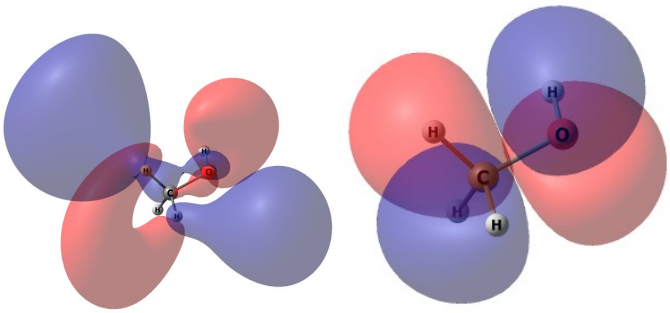

(a) $3d\sigma''$ (b) $HOMO(2a'')$

Figure D.19: $19^1A''$: $3d\sigma'' \leftarrow HOMO\,(2a'')$

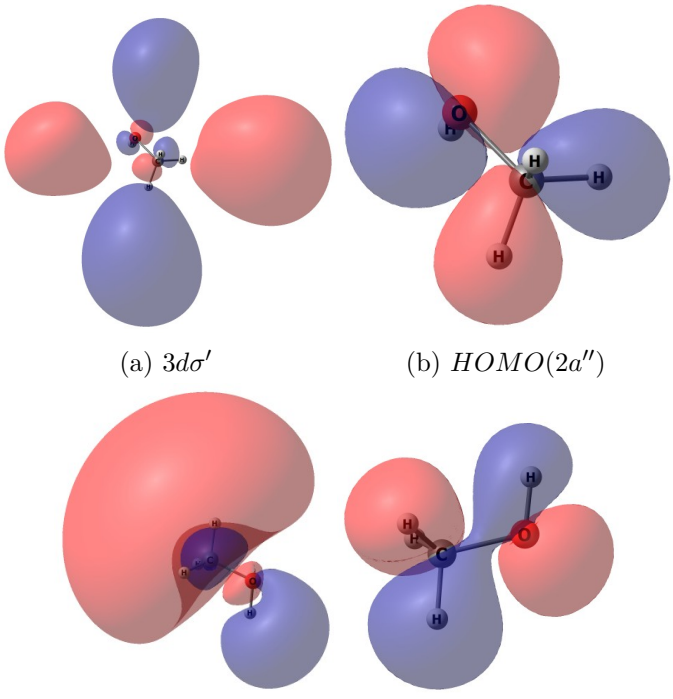

(a) $3d\sigma'$ (b) $HOMO(2a'')$

(c) $3p\pi'$ (d) $HOMO-1\,(7a')$

Figure D.20: $20^3A'$: $3d\sigma' \leftarrow HOMO\,(2a'')$
$+\,3p\pi' \leftarrow HOMO-1\,(7a')$

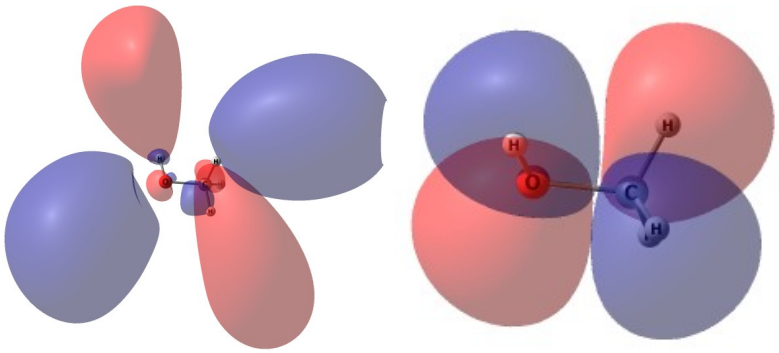

(a) $3d/\sigma^*$ (b) $HOMO(2a'')$

Figure D.21: $21^3A'' : 3d/\sigma^* \leftarrow HOMO\,(2a'')$

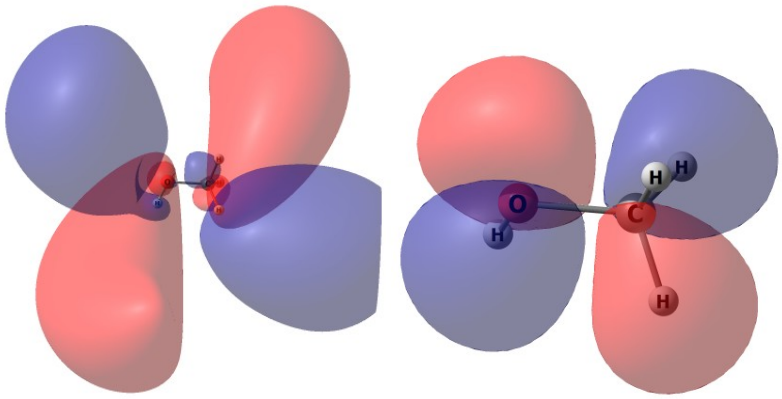

(a) $3d/\sigma^*$ (b) $HOMO(2a'')$

Figure D.22: $22^1A'' : 3d/\sigma^* \leftarrow HOMO\,(2a'')$

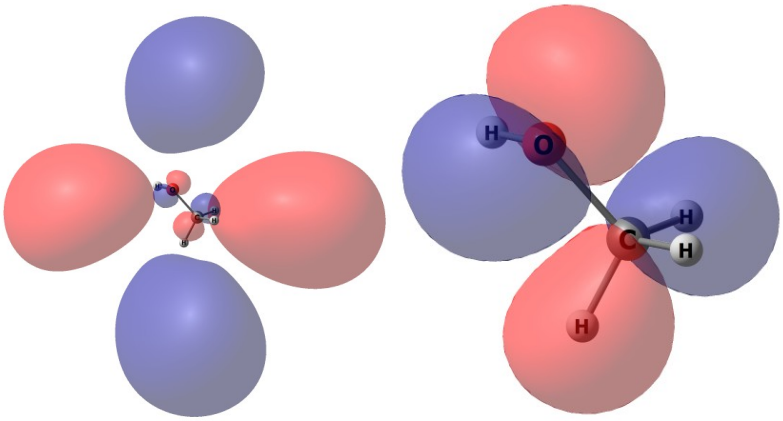

(a) $3d/\sigma^*$ (b) $HOMO(2a'')$

Figure D.23: $23^1A' : 3d/\sigma^* \leftarrow HOMO\,(2a'')$

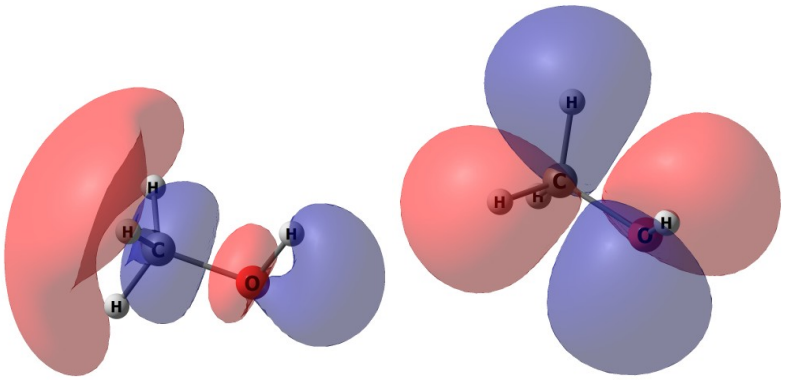

(a) $4p/\sigma^*$ (b) $HOMO(2a'')$

Figure D.24: $24^3A'' : 4p/\sigma^* \leftarrow HOMO\,(2a'')$

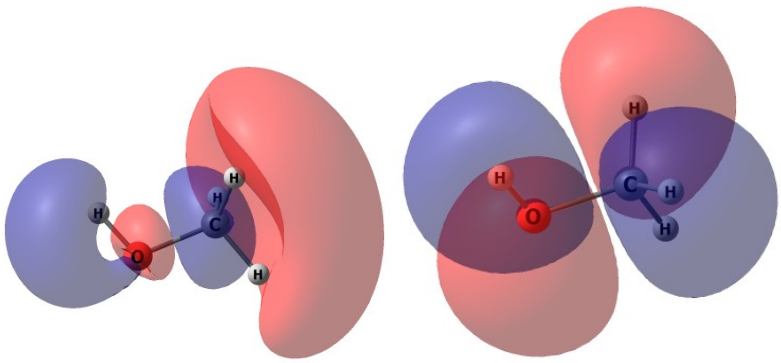

(a) $4p/\sigma^*$ (b) $HOMO(2a'')$

Figure D.25: $25^1A'' : 4p/\sigma^* \leftarrow HOMO\,(2a'')$

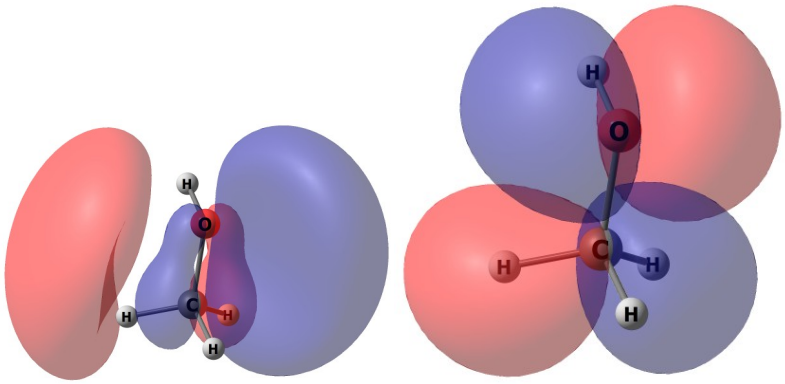

(a) $4p\pi$ (b) $HOMO(2a'')$

Figure D.26: $26^3A'' : 4p\pi \leftarrow HOMO\,(2a'')$

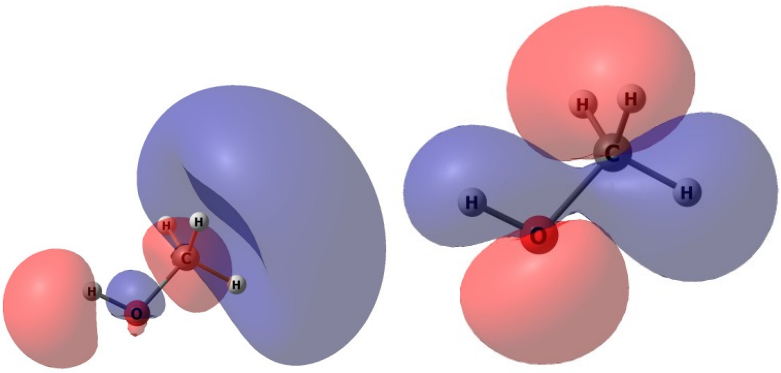

(a) $3p/\sigma^*$ (b) $HOMO-1(7a')$

Figure D.27: $27^1A'$: $3p/\sigma^* \leftarrow HOMO\,(7a')$

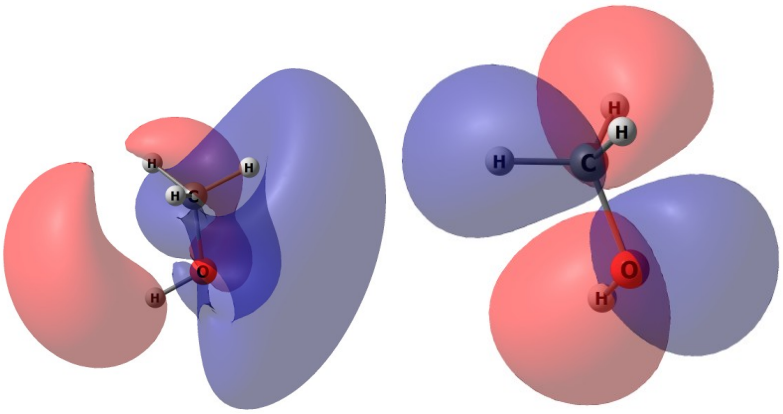

(a) $4p/\sigma^*$ (b) $HOMO(2a'')$

Figure D.28: $28^3A''$: $4p/\sigma^* \leftarrow HOMO\,(2a'')$

References

[1] D. F. Halpern. *Organofluorine Compounds in Medicinal Chemistry and Biomedical Applications*. 48th. Elsevier, 1993.

[2] M. K. Vollmer, T. S. Rhee, M. Rigby, D. Hofstetter, M. Hill, F. Schoenenberger, and S. Reimann. "Modern inhalation anesthetics: Potent greenhouse gases in the global atmosphere." In: *Geophysical Research Letters* 42 (2015), p. 1606.

[3] C. M. Ball and R. N. Westhorpe. "Halothane." In: *Anaesthesia and Intensive Care Journal* 35 (2007), p. 3.

[4] C. M. Ball and R. N. Westhorpe. "Desflurane." In: *Anaesthesia and Intensive Care Journal* 35 (2007), p. 657.

[5] C. M. Ball and R. N. Westhorpe. "Enflurane." In: *Anaesthesia and Intensive Care Journal* 35 (2007), p. 323.

[6] C. M. Ball and R. N. Westhorpe. "Isoflurane." In: *Anaesthesia and Intensive Care Journal* 35 (2007), p. 465.

[7] C. M. Ball and R. N. Westhorpe. "Sevoflurane." In: *Anaesthesia and Intensive Care Journal* 35 (2007), p. 835.

[8] J. S. Yasny and J. White. "Environmental Implications of Anesthetic Gases." In: *Anesthesia Progress* 59 (2012), p. 154.

[9] T. Langbein, H. Sonntag, D. Trapp, A. Hoffmann, W. Malms, E. P. Roth, V. Mors, and R. Zellner. "Volatile anaesthetics and the atmosphere: atmospheric lifetimes and atmospheric effects of halothane, enflurane, isoflurane, desflurane and sevoflurane." In: *British Journal of Anaesthesia* 82 (1999), p. 66.

[10] Y. Shiraishi and K. Ikeda. "Uptake and biotransformation of sevof lurane in humans: A comparative study of sevof lurane with halothane, enflurane, and isoflurane." In: *Journal of Clinical Anesthesia* 2 (1990), p. 381.

[11] M. P. S. Andersen, O. J. Nielsen, B. Karpichev, T. J. Wallington, and S. P. Sander. "Atmospheric chemistry of isoflurane, desflurane, and sevoflurane: Kinetics and mechanisms of reactions with chlorine atoms and oh radicals and global warming potentials." In: *Journal of Physical Chemistry A* 116 (2012), p. 5806.

[12] P. Limão-Vieira. "Electronic Excitation and Dissociation of Global Warming and Ozone Depleting Molecules." PhD thesis. University College of London, 2003.

[13] URL: https://earthobservatory.nasa.gov/Features/EnergyBalance/.

[14] G. L. Stephens, J. Li, M. Wild, C. A. Clayson, N. Loeb, S. Kato, T. L'Ecuyer, P. W. Stackhouse, M. Lebsock, and T. Andrews. "An update on Earth's energy balance in light of the latest global observations." In: *Nature Geoscience* 5 (2012), p. 691.

[15] M. Wild, D. Folini, C. Schär, N. Loeb, E. Dutton, and G. Konig-Langlo. "The Earth's radiation balance and its representation in CMIP5 models." In: *Geophysical Research Abstracts EGU General Assembly* 15 (2013), p. 2013.

[16] Ø. Hodnebrog, M. Etminan, J. S. Fuglestvedt, G. Marston, G. Myhre, C. J. Nielsen, K. P. Shine, and T. J. Wallington. "Global warming potentials and radiative efficiencies of halocarbons and related compounds: A comprehensive review." In: *Reviews of Geophysics* 51 (2013), p. 300.

[17] F. J. Melendez and M. A. Palafox. "Geometry and frequencies of the halothane molecule." In: *Journal of Molecular Structure* 493 (1999), p. 179.

[18] URL: https://www.ipcc.ch/publications_and_data/ar4/wg1/en/ch2s2-10-2.html.

[19] F. Cherubini, G. P. Peters, T. Berntsen, A. H. Strømman, and E. Hertwich. "CO2emissions from biomass combustion for bioenergy: Atmospheric decay and contribution to global warming." In: *GCB Bioenergy* 3 (2011), p. 413.

[20] Z. Farooq, D. A. Chestakov, B. Yan, G. C. Groenenboom, W. J. van der Zande, and D. H. Parker. "Photodissociation of singlet oxygen in the UV region." In: *Physical Chemistry Chemical Physics* 16 (2014), p. 3305.

[21] G. K. Moortgat and A. R. Ravishankara. *Ozone Depletion and Related Topics: Photochemistry of Ozone*. Second Edi. Vol. 4. Elsevier, 2014, p. 370.

[22] M. Nicolet and P. Mange. "The dissociation of oxygen in the high atmosphere." In: *Journal of Geophysical Research* 59 (1954), p. 15.

[23] J. G. Speight and J. G. Speight. *Chemical Transformations in the Environment*. Elsevier, 2017, pp. 305–353.

[24] C. A. Jones, E. Huberman, M. L. Cunningham, and M. J. Peak. "Mutagenesis and Cytotoxicity in Human Epithelial Cells by Far- and Near-Ultraviolet Radiations: Action Spectra." In: *Radiation Research* 110 (1987), p. 244.

[25] A. Ringvold. “Damage of the cornea epithelium caused by ultraviolet radiation.” In: *Acta Ophthalmologica* 61 (2009), p. 898.

[26] M. R. Zelle. “Biological Effects of Ultraviolet Radiation.” In: *IRE Transactions on Medical Electronics* ME-7 (1960), p. 130.

[27] J. Cadet, E. Sage, and T. Douki. “Ultraviolet radiation-mediated damage to cellular DNA.” In: *Mutation Research/Fundamental and Molecular Mechanisms of Mutagenesis* 571 (2005), p. 3.

[28] J.-L. Ravanat, T. Douki, and J. Cadet. “Direct and indirect effects of UV radiation on DNA and its components.” In: *Journal of Photochemistry and Photobiology B* 63 (2001), p. 88.

[29] R. Huggenberger and M. Detmar. “The Cutaneous Vascular System in Chronic Skin Inflammation.” In: *Journal of Investigative Dermatology Symposium Proceedings* 15 (2011), p. 24.

[30] M. W. Greaves and J. Søndergaard. “Pharmacologic Agents Released in Ultraviolet Inflammation Studied by Continuous Skin Perfusion.” In: *Journal of Investigative Dermatology* 54 (1970), p. 365.

[31] R. W. Young. “Solar radiation and age-related macular degeneration.” In: *Survey of ophthalmology* 32 (1988), p. 252.

[32] J. E. Roberts. “Ultraviolet Radiation as a Risk Factor for Cataract and Macular Degeneration.” In: *Eye & Contact Lens: Science & Clinical Practice* 37 (2011), p. 246.

[33] G. Jenkins. “Molecular mechanisms of skin ageing.” In: *Mechanisms of Ageing and Development* 123 (2002), p. 801.

[34] Y. Matsumura and H. N. Ananthaswamy. “Toxic effects of ultraviolet radiation on the skin.” In: *Toxicology and Applied Pharmacology* 195 (2004), p. 298.

[35] J. D’Orazio, S. Jarrett, A. Amaro-Ortiz, and T. Scott. “UV Radiation and the Skin.” In: *International Journal of Molecular Sciences* 14 (2013), p. 12222.

[36] F. R. de Gruijl. “Skin cancer and solar UV radiation.” In: *European Journal of Cancer* 35 (1999), p. 2003.

[37] K. Hanninen. “The Role of Excited Oxygen Molecules in the Formation of the Secondary Ozone Layer at 87 to 97 km.” In: *Environment and Ecology Research* 6 (2018), p. 74.

[38] URL: http://www.oxidationtech.com/blog/ozone-produced-naturally-from-uv-light/.

[39] J. C. Farman, B. G. Gardiner, and J. D. Shanklin. “Large losses of total ozone in Antarctica reveal seasonal ClO x /NO x interaction.” In: *Nature* 315 (1985), p. 207.

[40] *Nasa Ozone Watch: Ozone hole history facts.* URL: https://ozonewatch.gsfc.nasa.gov/facts/history{_}SH.html (visited on 06/26/2018).

[41] R. Lindsey. *World of Change: Antarctic Ozone Hole : Feature Articles.* 2009. (Visited on 06/26/2018).

[42] S. Solomon, R. R. Garcia, F. S. Rowland, and D. J. Wuebbles. "On the depletion of Antarctic ozone." In: *Nature* 321 (1986), p. 755.

[43] T. M. L. Wigley. "Future CFC concentrations under the Montreal Protocol and their greenhouse-effect implications." In: *Nature* 335 (1988), p. 333.

[44] R. G. Prinn and A. Golombek. "Global atmospheric chemistry of CFC-123." In: *Nature* 34 (1990), p. 47.

[45] S.-M. Fan and D. J. Jacob. "Surface ozone depletion in Arctic spring sustained by bromine reactions on aerosols." In: *Nature* 359 (1992), p. 522.

[46] J. C. McConnell, G. S. Henderson, L. Barrie, J. Bottenheim, H. Niki, C. H. Langford, and E. M. J. Templeton. "Photochemical bromine production implicated in Arctic boundary-layer ozone depletion." In: *Nature* 355 (1992), p. 150.

[47] J. W. T. Spinks. "Photosensitised Decomposition of Ozone by Bromine." In: *Nature* 128 (1931), p. 548.

[48] M. J. Prather and R. T. Watson. "Stratospheric ozone deplection and future levels of atmospheric chlorine and bromine." In: *Nature* 344 (1990), p. 729.

[49] M. J. Molina and F. S. Rowland. "Stratospheric sink for chlorofluoromethanes: Chlorine atomc-atalysed destruction of ozone." In: *Nature* 249 (1974), p. 810.

[50] R. G. W. Norrish and G. H. J. Neville. "Photosensitised Decomposition of Ozone by Chlorine." In: *Nature* 131 (1933), p. 544.

[51] Samuel Eden. "Spectroscopic and Electron Impact of Molecules Relevant to Plasma Etching." PhD thesis. University of London, 2003.

[52] P. A. Kandell. "Spectroscopic Studies of Atmospheric Molecules Related to Global Warming." PhD thesis. University of London, 2003.

[53] W. B. Demore, C. J. Howard, S. P. Sander, A. R. Ravishankara, D. M. Golden, C. E. Kolb, R. F. Hampson, M. J. Molina, and M. J. Kurylo. *Chemical Kinetics and Photochemical Data for Use in Stratospheric Modeling, Evaluation Number 12.* Tech. rep. Jet Propulsion Laboratory, 1997.

[54] A. C. Brown, C. E. Canosa-Mas, A. D. Parr, J. M. T. Pierce, and R. P. Wayne. "Tropospheric lifetimes of halogenated anaesthetics." In: *Nature* 342 (1989), p. 635.

[55] J. S. Daniel, S Solomon, R. W. Portmann, and R. R. Garcia. "Stratospheric ozone destruction: The importance of bromine relative to chlorine." In: *Journal of Geophysical Research* 104 (1999), p. 871.

[56] E. Lange. "Espalhamento de pósitrons por moléculas de metano, fluoretos de metano e tetrafluoreto de carbono." Master's thesis. UFPR, 2013.

[57] T. Schlick. *Molecular Modeling and Simulation: An Interdisciplinary Guide*. Springer, 2010.

[58] N. S. O. A. Szabo. *Modern Quantum Chemistry - Introduction to Advanced Electronic Structure Theory*. Dover, 1996.

[59] N. H. Morgan and K. Coutinho. *Métodos de Química Teórica e Modelagem Molecular*. Editora da Física, 2007.

[60] R. F. Da Costa, M. T.D. N. Varella, M. H. F. Bettega, and M. A. P. Lima. "Recent advances in the application of the Schwinger multichannel method with pseudopotentials to electron-molecule collisions." In: *European Physical Journal D* 69 (2015), p. 159.

[61] S. Obara and A. Saika. "General recurrence formulas for molecular integrals over Cartesian Gaussian functions." In: *The Journal of Chemical Physics* 89 (1988), p. 1540.

[62] P. Limão-Vieira. "Electronic Excitation and Dissociation of Global Warmin and Ozone Depleting Molecules." PhD thesis. University College London, 2003.

[63] A. Giuliani. "Furan and Some Selected Derivatives - A Valence Shell Spectroscopy Study by Photon and Electron Impact Methods." PhD thesis. Université de Liège, 2004.

[64] A. J. Lees. *Photophysics of organometallics*. Springer-Verlag, 2010.

[65] C. Sandorfy. "Rydberg states in chemistry." In: *International Journal of Quantum Chemistry* 19 (1981), p. 1147.

[66] M. Seaton. "Quantum defect theory." In: *Reports on Progress in Physics* 46 (1983), p. 167.

[67] N. Kosugi. "Orbital picture in molecular inner-shell excited states of Rydberg-valence mixed character." In: *Brazilian Journal of Physics* 35 (2005), p. 957.

[68] N. Kosugi. "Valence in the Rydberg/continuum region in molecular inner-shell spectroscopy." In: *Journal of Electron Spectroscopy and Related Phenomena* 144 (2005), p. 1203.

[69] F. Ferreira da Silva. "Espectroscopia de estados eletrónicos de moléculas de interesse biológicos por radiação sincrotrão : acetona e pirimidina." PhD thesis. FCT-UNL, 2007.

[70] B. H. Bransden and C. J. Joachain. *Physics of Atoms and Molecules*. Longman, 1983.

[71] J. M. Hollas. *Modern Spectroscopy*. 4th. Wiley, 2004, pp. 13–7.

[72] URL: https://chem.libretexts.org/Bookshelves/Physical_and_Theoretical_Chemistry_Textbook_Maps/Supplemental_Modules_(Physical_and_Theoretical_Chemistry)/Spectroscopy/Vibrational_Spectroscopy/Vibrational_Modes/Combination_Bands%2C_Overtones_and_Fermi_Resonances.

[73] W. R. Moomaw and J. F. Skinner. "Vibronic Spectra and Energy Levels of Polyatomic Molecules A physical chemistry experiment." In: *Journal of Chemical Education* 48 (1971), p. 304.

[74] W. R. Moomaw and J. F. Skinner. "Vibronic spectra and energy levels of polyatomic molecules. A physical chemistry experiment." In: *Journal of Chemical Education* 48 (2009), p. 304.

[75] G. Graner. "What can molecular spectroscopy tell us about hot bands?" In: *Rev. Mexicana Astron. Astrof.* 23 (1992), p. 79.

[76] L. H. Xu, A. M. Andrews, and G. T. Fraser. "Study of the overtone C-O stretching band of methanol by multiple resonance spectroscopy." In: *The Journal of Chemical Physics* 103 (1995), p. 14.

[77] L. H. Sutcliffe and A. D. Walsh. "Far ultra-violet absorption spectrum of trifluoro methyl iodide." In: *Transactions of the Faraday Society* 57 (1961), p. 873.

[78] C. J. Joachain. *Quantum Collision Theory*. North-Holland, 1987.

[79] M. A. P. Lima and V. Mckoy. "Aspects of the Schwinger multichannel variational formulation." In: *Physical Review A* 38 (1988), p. 501.

[80] E. Feenberg. "The scattering of slow electrons by neutral atoms." In: *Physical Review* 40 (1932), p. 40.

[81] J. J. Sakurai and J. Napolitano. *Modern Quantum Physics*. second edition. Cambridge University Press, 2013.

[82] G. Herzberg. *Spectra of diatomic molecules*. Princeton: D. Van Nostrand Compagny, 1966.

[83] P. W. Atkins and R. Friedman. *Molecular quantum mechanics*. Oxford University Press, 2011.

[84] U. Cooper and J. W. Fano. "Spectral Distribuition of Atomic Oscillator Strengths." In: *Reviws of Modern Physics* 40 (1968), p. 441.

[85] R. C. Hilborn. "Einstein coefficients, cross sections, f values, dipole moments, and all that." In: *American Journal of Physics* 50 (1982), p. 982.

[86] P Hannaford. "The Oscillator Strength in Atomic Absorption Spectroscopy 1." In: *Microchemical Journal* 63 (1999), p. 43.

[87] J. Ameixa. "Electronic States Characterization of the Anesthetic Halothane by High Resolution Electron Energy Loss Spectroscopy." Master's thesis. Faculdade de Ciências e Tecnologia da Universidade NOVA de Lisboa, 2015.

[88] L. G. Christophorou. *Electron - Molecular and Their Applications*. Vol. 1. Academic Press, Iic, 1984.

[89] K. D. Sevier. *Low energy electron spectrometry*. Wiley-Interscience, 1972, p. 397.

[90] C. E. Kuyatt. "Electrostatic Lenses, by E. Harting and F. H. Read Reviewer." In: *Review of Scientific Instruments* 49 (1978), p. 551.

[91] G. Reich. "On the significance of mean free path to vacuum physics and technology." In: *Vacuum* 41 (1990), p. 2041.

[92] URL: http://www.isa.au.dk.

[93] S. Eden, P. Limão-Vieira, S. Hoffmann, and N. J. Mason. "VUV photoabsorption in CF3X (X=Cl, Br, I) fluoro-alkanes." In: *Chemical Physics* 323 (2006), p. 313.

[94] M. H. Palmer, T. Ridley, S. V. Hoffmann, N. C. Jones, M. Coreno, M. de Simone, C. Grazioli, M. Biczysko, A. Baiardi, and P. Limão-Vieira. "Interpretation of the vacuum ultraviolet photoabsorption spectrum of iodobenzene by ab initio computations." In: *The Journal of Chemical Physics* 142 (2015), p. 134302.

[95] F. Ferreira da Silva, E. Lange, P. Limão-Vieira, N. C. Jones, S. V. Hoffmann, M. J. Hubin-Franskin, J. Delwiche, M. J. Brunger, R. F. C. Neves, M. C. A. Lopes, E. M. De Oliveira, R. F. Da Costa, M. T.D. N. Varella, M. H. F. Bettega, F. Blanco, G. Garcia, M. A. P. Lima, and D. B. Jones. "Electronic excitation of furfural as probed by high-resolution vacuum ultraviolet spectroscopy, electron energy loss spectroscopy, and ab initio calculations." In: *Journal of Chemical Physics* 143 (2015), p. 144308.

[96] F. Blanco and G. García. "Screening corrections for calculation of electron scattering from polyatomic molecules." In: *Physics Letters A* 317 (2003), p. 458.

[97] F. Blanco and G. García. "Screening corrections for calculation of electron scattering differential cross sections from polyatomic molecules." In: *Physics Letters A* 330 (2004), p. 230.

[98] F. Blanco and G. García. "Improvements on the quasifree absorption model for electron scattering." In: *Physical Review A* 67 (2003), p. 9.

[99] M. E. Riley and D. G. Truhlar. "Approximations for the exchange potential in electron scattering." In: *The Journal of Chemical Physics* 63 (1975), p. 2182.

[100] X. Zhang, J. Sun, and Y. Liu. "A New Approach to the Correlation Polarization Potential - Low-Energy Electron Elastic Scattering by He Atoms." In: *Journal of Physics B* 25 (1992), p. 1893.

[101] A. Zecca, G. P. Karwasz, and R. S. Brusa. "Electron scattering by Ne , Ar and Kr at intermediate and high energies , 0 . 5 – 10 keV." In: *Journal of Physics B:Journal of Physics B:* 33 (2000), p. 843.

[102] H. William. *Numerical Recipes in Fortran.* 2nd ed. Cambridge University Press, 1994.

[103] F. Calogero. *Variable Phase Approach to Potential Scattering.* Academic, New York, 1994.

[104] H. S.W. M. N. F. Mott. *The Theory of Atomic Collisions.* Oxford Univ. Press, 1965.

[105] F. Blanco, J. Rosado, A. Illana, and G. García. "Comparison of two screening corrections to the additivity rule for the calculation of electron scattering from polyatomic molecules." In: *Physics Letters A* 374 (2010), p. 4420.

[106] F. Blanco and G. García. "Calculated cross sections for electron elastic and inelastic scattering from DNA and RNA bases." In: *Physics Letters A* 360 (2007), p. 707.

[107] F. Blanco, A. Muñoz, D. Almeida, F. F. Da Silva, P. Limão-Vieira, M. C. Fuss, A. G. Sanz, and G. García. "Modelling low energy electron and positron tracks in biologically relevant media." In: *European Physical Journal D* 67 (2013), p. 1.

[108] S. d'Almeida Sanchez. "O Aprimoramento do Método Multicanal de Schwinger para o Espalhamento de Pósitrons por Átomos Moléculas." PhD thesis. Unicamp, 2008.

[109] M. T.d. N. Varella. "Densidade de Probabilidade de Aniquilação e Outras Aplicações do Método Multicanal de Schwinger ao Espalhamento de Pósitrons e Elétrons." PhD thesis. Unicamp, 2001.

[110] E. Joukoski. "Espalhamento de elétrons por moléculas de NF_3 e SnY_4 (Y = Cl, Br, I)." PhD thesis. UFPR, 2002.

[111] A. do Rocio Lopes. "polarização do Alvo Moleculas no Espalhamento de Elétrons." PhD thesis. Unicamp, 2007.

[112] B. A. Lippmann and J. Schwinger. "Variational Princiyles for Scattering Processes." In: *Physical Review* 79 (1950), p. 469.

[113] M. A. P. Lima, L. M. Brescansin, A. J. R. Da Silva, C. Winstead, and V. McKoy. "Applications of the Schwinger multichannel method to electron-molecule collisions." In: *Physical Review A* 41 (1990), p. 327.

[114] K. Takatsuka and V. Mckoy. "Theory of electronically inelastic scattering of electrons by molecules." In: *Physical Review A* 30 (1984), p. 1734.

[115] F. Arretche, R. F. da Costa, S. d. A. Sanchez, A. N. S. Hisi, E. M. de Oliveira, M. T.d. N. Varella, and M. A. P. Lima. "Similarities and differences in e±-molecule scattering: Applications of the Schwinger multichannel method." In: *Nuclear Instruments and Methods in Physics Research, Section B: Beam Interactions with Materials and Atoms* 247 (2006), p. 13.

[116] J. R. Taylor. *Scattering Theory The Quantum Theory of Nonrelativistic Collisions*. John Wiley & Sons, Inc., 1972.

[117] M. H. F. Bettega, L. G. Ferreira, and M. A. P. Lima. "Local-Density Norm-Conserving Pseudopotentials." In: *Physical Review A* 47 (1993), p. 1111.

[118] D. Duflot, F. Ferreira da Silva, E. Lange, N. C. Jones, S. V. Hoffmann, M. A. Smialek, and M. J. Brunger. "Valence and lowest Rydberg electronic states of phenol investigated by synchrotron radiation and theoretical methods." In: *Journal of Chemical Physics* 145 (2016), p. 034302.

[119] O. A. Vydrov and G. E. Scuseria. "Assessment of a long-range corrected hybrid functional." In: *The Journal of Chemical Physics* 125 (2006), p. 234109.

[120] O. A. Vydrov, J. Heyd, A. V. Krukau, and G. E. Scuseria. "Importance of short-range versus long-range Hartree-Fock exchange for the performance of hybrid density functionals." In: *The Journal of Chemical Physics* 125 (2006), p. 074106.

[121] O. A. Vydrov, G. E. Scuseria, and J. P. Perdew. "Tests of functionals for systems with fractional electron number." In: *The Journal of Chemical Physics* 126 (2007), p. 154109.

[122] M. J. Frisch, G. W. Trucks, H. B. Schlegel, G. E. Scuseria, M. A. Robb, J. R. Cheeseman, G. Scalmani, V. Barone, B. Mennucci, G. A. Petersson, H. Nakatsuji, M. Caricato, X. Li, H. P. Hratchian, A. F. Izmaylov, J. Bloino, G. Zheng, J. L. Sonnenberg, M. Hada, M. Ehara, K. Toyota, R. Fukuda, J. Hasegawa, M. Ishida, T. Nakajima, Y. Honda, O. Kitao, H. Nakai, T Vreven, J. A. Montgomery, J. A. Peralta, M. Ogliaro F. andBearpark, J. J. Heyd, E. Brothers, K. N. Kudin, V. N. Staroverov, R. Kobayashi, J. Normand, K. Raghavachari, A. Rendell, J. C. Burant, S. S. Iyengar, J. Tomasi, M. Cossi, N. Rega, J. M. Millam, M. Klene, J. E. Knox, J. B. Cross, V. Bakken, C. Adamo, J. Jaramillo, R. Gomperts, R. E. Stratmann, A. J. Yazyev O. and. Austin, R. Cammi, C. Pomelli, J. W. Ochterski, R. L. Martin, K. Morokuma, V. G. Zakrzewski, G. A. Voth, P. Salvador, J. J. Dannenberg, S. Dapprich, A. D. Daniels, O. Farkas, J. B. Foresman, J. V. Ortiz, J. Cioslowski, and D. J. Fox. *Gaussian 09*. Gaussian, Inc., Wallingford CT,Gaussian, Inc., Wallingford CT. 2009.

[123] T. H. Dunning. "Gaussian basis sets for use in correlated molecular calculations. I. The atoms boron through neon and hydrogen." In: *The Journal of Chemical Physics* 90 (1989), p. 1007.

[124] K. Kaufmann, W. Baumeister, and M. Jungen. "Universal Gaussian basis sets for an optimum representation of Rydberg and continuum wavefunctions." In: *Journal of Physics B* 22 (1989), p. 2223.

[125] R. L. Martin. "Natural transition orbitals." In: *The Journal of Chemical Physics* 118 (2003), p. 4775.

[126] M. J. Brunger. "International Reviews in Physical Chemistry Electron scattering and transport in biofuels , biomolecules and biomass fragments." In: *International Reviews in Physical Chemistry* 36 (2017), p. 333.

[127] D. B. Jones, R. F. Da Costa, M. T. N. Varella, M. H. Bettega, M. A. Lima, F. Blanco, G. Garcia, and M. J. Brunger. "Integral elastic, electronic-state, ionization, and total cross sections for electron scattering with furfural." In: *Journal of Chemical Physics* 144 (2016), p. 144303.

[128] F. Blanco and G. García. "Interference effects in the electron and positron scattering from molecules at intermediate and high energies." In: *Chemical Physics Letters* 635 (2015), p. 321.

[129] F. Ferreira Da Silva, E. Lange, P. Limão-Vieira, N. C. Jones, S. V. Hoffmann, M. J. Hubin-Franskin, J. Delwiche, M. J. Brunger, R. F. C. Neves, M. C. A. Lopes, E. M. De Oliveira, R. F. Da Costa, M. T.D. N. Varella, M. H. F. Bettega, F. Blanco, G. García, M. A. P. Lima, and D. B. Jones. "Electronic excitation of furfural as probed by high-resolution vacuum ultraviolet spectroscopy, electron energy loss spectroscopy, and ab initio calculations." In: *Journal of Chemical Physics* 143 (2015), p. 144308.

[130] R. F. Da Costa, E. M. De Oliveira, M. H. F. Bettega, M. T.D. N. Varella, D. B. Jones, M. J. Brunger, F. Blanco, R. Colmenares, P. Limão-Vieira, G. Garcia, and M. A. P. Lima. "Electron collisions with phenol: Total, integral, differential, and momentum transfer cross sections and the role of multichannel coupling effects on the elastic channel." In: *Journal of Chemical Physics* 142 (2015), p. 104304.

[131] D. F. Pastega, E. Lange, J. Ameixa, A. S. Barbosa, F. Blanco, G. García, M. H. F. Bettega, P. Limão-Vieira, and F. Ferreira da Silva. "Combined experimental and theoretical study on the differential elastic scattering cross sections for acetone by electron impact energy of 7.0–50 eV." In: *Physical Review A* 93 (2016), p. 032708.

[132] A. S. Barbosa, M. T.D. N. Varella, S. D. Sanchez, J. Ameixa, F. Blanco, G. Garcia, P. Limão-Vieira, F. Ferreira Da Silva, and M. H. F. Bettega. "Theoretical and experimental study on electron interactions with chlorobenzene: Shape resonances and differential cross sections." In: *Journal of Chemical Physics* 145 (2016), p. 084311.

[133] K. Krupa, E. Lange, F. Blanco, A. S. Barbosa, D. F. Pastega, S. D. Sanchez, M. H. Bettega, G. García, P. Limão-Vieira, and F. Ferreira Da Silva. "Experimental and theoretical electron-scattering cross-section data for dichloromethane." In: *Physical Review A* 97 (2018), p. 1.

[134] V. K. Dolmatov, M. Y. Amusia, and L. V. Chernysheva. "Electron elastic scattering off A-C60 : The role of atomic polarization under confinement." In: *Physical Review A* 92 (2015), p. 042709.

[135] A. Lesarri, A. Vega-Toribio, R. D. Suenram, D. J. Brugh, and J.-U. Grabow. "The conformational landscape of the volatile anesthetic sevoflurane." In: *Physical Chemistry Chemical Physics* 12 (2010), p. 9624.

[136] T. J. A. Craddock, P. Kurian, J. Preto, K. Sahu, S. R. Hameroff, M. Klobukowski, and J. A. Tuszynski. "Anesthetic Alterations of Collective Terahertz Oscillations in Tubulin Correlate with Clinical Potency: Implications for Anesthetic Action and Post-Operative Cognitive Dysfunction." In: *Scientific Reports* 7 (2017), p. 9877.

[137] J. J. Dom, B. J. Van Der Veken, B. Michielsen, S. Jacobs, Z. Xue, S. Hesse, H. M. Loritz, M. A. Suhm, and W. A. Herrebout. "On the weakly C-H π hydrogen bonded complexes of sevoflurane and benzene." In: *Physical Chemistry Chemical Physics* 13 (2011), p. 14142.

[138] E Lange, F Ferreira da Silva, N. C. Jones, S. V. Hoffmann, D Duflot, and P Limão-vieira. "The lowest-lying electronic states of isoflurane and sevoflurane in the 5.0 – 10.8 eV energy range investigated by experimental and theoretical methods." In: *Chemical Physics Letters* 716 (2019), p. 42.

[139] M. J. Arcario, C. G. Mayne, and E. Tajkhorshid. "Atomistic models of general anesthetics for use in in silico biological studies." In: *Journal of Physical Chemistry B* 118 (2014), p. 12075.

[140] Y. Nagashima, T. Suzuki, S. Terada, S. Tsuji, and K. Misawa. "In vivo molecular labeling of halogenated volatile anesthetics via intrinsic molecular vibrations using nonlinear Raman spectroscopy." In: *Journal of Chemical Physics* 134 (2011), p. 024525.

[141] P. E. I. Tang, I. Zubryzcki, and Y. A. N. Xu. "Ab Initio Calculation of Structures and Anesthetics : Halothane and Sevoflurane." In: *Journal of Computational Chemistry* 22 (2001), p. 436.

[142] F. F. Da Silva, D. Duflot, S. V. Hoffmann, N. C. Jones, F. N. Rodrigues, A. M. Ferreira-Rodrigues, G. G. B. De Souza, N. J. Mason, S. Eden, and P. Limão-Vieira. "Electronic State Spectroscopy of Halothane As Studied by ab Initio Calculations, Vacuum Ultraviolet Synchrotron Radiation, and Electron Scattering Methods." In: *Journal of Physical Chemistry A* 119 (2015), p. 8503.

[143] D. E. Woon and T. H. Dunning. "Gaussian basis sets for use in correlated molecular calculations. III. The atoms aluminum through argon." In: *The Journal of Chemical Physics* 98 (1993), p. 1358.

[144] J. Ferreira, A. Seabra, G. Dolgounitcheva, O. Zakrzewski, and V. Ortiz. *Application and testing of diagonal, partial third-order electron propagator approximation, Quantum Mechanical Prediction of Thermochemical Data.* Ed. by D. Kluwer. The Netherlands, 2001.

[145] O. Ortiz, J. Zakrzewski, V.G, and Dolgounircheva. *Conceptual Perspectives in Quantum Chemistry*. Kluwer Academic, Boston, 1997.

[146] C. graphical software for visualization of quantum chemistry computations. URL: https://www.chemcraftprog.com.

[147] F. Ferreira da Silva, D. Duflot, S. V. Hoffmann, N. C. Jones, F. N. Rodrigues, A. M. Ferreira-Rodrigues, G. G. B. de Souza, N. J. Mason, S. Eden, and P. Limão-Vieira. "Electronic State Spectroscopy of Halothane As Studied by ab Initio Calculations, Vacuum Ultraviolet Synchrotron Radiation, and Electron Scattering Methods." In: *Journal of Physical Chemistry A* 119 (2015), p. 8503.

[148] J.-L. Calais and E. Kryachko, eds. *Conceptual Perspectives in Quantum Chemistry*. Springer Netherlands, 1997.

[149] M. P. S. Andersen, S. P. Sander, O. J. Nielsen, D. S. Wagner, T. J. Sanford, and T. J. Wallington. "Inhalation anaesthetics and climate change." In: *British Journal of Anaesthesia* 105 (2010), p. 760.

[150] P. Limão-Vieira, A. Giuliani, J. Delwiche, R. Parafita, R. Mota, D. Duflot, J. P. Flament, E. Drage, P. Cahillane, N. J. Mason, S. V. Hoffmann, and M. J. Hubin-Franskin. "Acetic acid electronic state spectroscopy by high-resolution vacuum ultraviolet photo-absorption, electron impact, He(I) photoelectron spectroscopy and ab initio calculations." In: *Chemical Physics* 324 (2006), p. 339.

[151] R. K. Talukdar, G. L. Vaghjiani, and A. R. Ravishankara. "Photodissociation of bromocarbons at 193, 222, and 248 nm: Quantum yields of Br atom at 298 K." In: *The Journal of Chemical Physics* 96 (1992), p. 8194. DOI: 10.1063/1.462324. URL: http://aip.scitation.org/doi/10.1063/1.462324.

[152] Y. Kanaya, Y. Kajii, and H. Akimoto. "Solar actinic flux and photolysis frequency determinations by radiometers and a radiative transfer model at Rishiri Island: Comparisons, cloud effects, and detection of an aerosol plume from Russian forest fires." In: *Atmospheric Environment* 37 (2003), p. 2463.

[153] G. W. Schade and A. H. Goldstein. "Seasonal measurements of acetone and methanol: Abundances and implications for atmospheric budgets." In: *Global Biogeochemical Cycles* 20 (2006), p. 1.

[154] M.-T. Lee, G. L. C. de Souza, L. E. Machado, L. M. Brescansin, A. S. dos Santos, R. R. Lucchese, R. T. Sugohara, M. G. P. Homem, I. P. Sanches, and I Iga. "Electron scattering by methanol and ethanol: a joint theoretical-experimental investigation." In: *The Journal of chemical physics* 136 (2012), p. 114311.

[155] M. P. Bernstein, S. A. Sandford, L. J. Allamandola, S. Chang, and M. A. Scharberg. "Organic Compounds Produced by Photolysis of Realistic Interstellar and Cometary Ice Analogs Containing Methanol." In: *The Astrophysical Journal* 454 (1995), p. 327.

[156] P Ehrenfreund and S. B. Charnley. "Organic Molecules in the Interstellar Medium, Comets, and Meteorites: A Voyage from Dark Clouds to the Early Earth." In: *Annual Review of Astronomy and Astrophysics* 38 (2000), p. 427.

[157] R. T. Garrod, S. L. W. Weaver, and E. Herbst. "Complex Chemistry in Star-forming Regions: An Expanded Gas-Grain Warm-up Chemical Model." In: *The Astrophysical Journal* 682 (2008), p. 283.

[158] K. I. Öberg, R. T. Garrod, E. F. van Dishoeck, and H. Linnartz. "Formation rates of complex organics in UV irradiated CH 3 OH-rich ices." In: *Astronomy and Astrophysics* 504 (2009), p. 891.

[159] J. C. Laas, R. T. Garrod, E. Herbst, and S. L. Widicus Weaver. "Contributions from grain surface and gas phase chemistry to formation of methyl formate and irs structural isomers." In: *The Astrophysical Journal* 728 (2011), p. 71.

[160] A. J. Harrison, B. J. Cederholm, and M. A. Terwilliger. "Absorption of Acyclic Oxygen Compounds in the Vacuum Ultraviolet. I. Alcohols." In: *The Journal of Chemical Physics* 30 (1959), p. 355.

[161] D. R. Salahub and C. Sandorfy. "The far-ultraviolet spectra of some simple alcohols and fluoroalcohols." In: *Chemical Physics Letters* 8 (1971), p. 71.

[162] H. Tsubomura, K. Kimura, K. Kaya, J. Tanaka, and S. Nagakura. "Vacuum Ultraviolet Absorption Spectra of Saturated Organic Compounds with Non-bonding Electrons." In: *Bulletin of the Chemical Society of Japan* 37 (1964), p. 417.

[163] M. B. Robin. "Excited Eletronic States of the Simple Alcohols." In: *Journal of Electron Spectroscopy and Related Phenomena* 1 (1972), p. 13.

[164] M. B. Robin. *Higher Excited States of Polyatomic Molecules.* Vol. 1. Academic Press, 1974, p. 255. ISBN: 0-12-589903-3.

[165] B.-M. Cheng, M. Bahou, W.-C. Chen, C.-h. Yui, Y.-P. Lee, and L. C. Lee. "Experimental and theoretical studies on vacuum ultraviolet absorption cross sections and photodissociation of CH[3OH, CH3OD, CD3OH, and CD3OD." In: *The Journal of Chemical Physics* 117 (2002), p. 1633.

[166] M. B. Robin and N. A. Kuebler. "Pressure Effects on Vacuum Ultraviolet Spectra." In: *Journal of Molecular Spectroscopy* 33 (1970), p. 274.

[167] Y. Shao et al. "Advances in molecular quantum chemistry contained in the Q-Chem 4 program package." In: *Molecular Physics* 113 (2015), p. 184.

[168] C. C. Bonang, D. J. Anderson, S. M. Cameron, P. B. Kelly, and J. D. Getty. "Ultraviolet Raman scattering from simple alcohols and a related diol as a study of low-lying Rydberg-valence state characteristics." In: *The Journal of Chemical Physics* 99 (1993), p. 6245.

[169] J. Nee, M. Suto, and L. Lee. "Photoexcitation processes of CH3OH: Rydberg states and photofragment fluorescence." In: *Chemical Physics* 98 (1985), p. 147.

[170] K. A. G. Macneil and R. N. Dixon. "High-resolution photoelectron spectroscopy of methanol and dewterates derivatives." In: *Jounal of Electron Spectroscopy and Related Phenomena,* 11 (1995), p. 315.

[171] M. I. Al-Joboury and D. W. Turner. "Molecular Photoelectron Espectroscopy. Part II A Summary of Ionization Potentials." In: *Journal of the Chemical Society* (1967), p. 373.

[172] J. Berkowitz. "Photoionization of CH3OH, CD3OH, and CH3OD: Dissociative ionization mechanisms and ionic structures." In: *The Journal of Chemical Physics* 69 (1978), p. 3044.

[173] B. Brehm, V. Fuchs, and P. Kebarle. "Autoionization and fragmentation processes in methanol and ethanol." In: *International Journal of Mass Spectrometry and Ion Physics* 6 (1971), p. 279.

[174] M. J. S. Dewar and S. D. Worley. "Photoelectron Spectra of Molecules. I. Ionization Potentials of Some Organic Molecules and Their Interpretation." In: *The Journal of Chemical Physics* 50 (1969), p. 654. DOI: 10.1063/1.1671114. URL: http://aip.scitation.org/doi/10.1063/1.1671114.

[175] E. Sominska and A. Gedanken. "The Absorption Spectrum of a Supersonically Expanded Beam of Methanol in the Vacuum Ultraviolet Region." In: *Journal of Molecular Spectroscopy* 238 (1996), p. 234.

[176] NASA. *Chemical Kinetics and Photochemical Data for Use in Stratospheric Modeling, Evaluation Number 12.* Tech. rep. 1997.

[177] E. Jiménez, M. K. Gilles, and A. R. Ravishankara. "Kinetics of the reactions of the hydroxyl radical with CH_3OH and C_2H_5OH between 235 and 360 K." In: *Journal of Photochemistry and Photobiology A: Chemistry* 157 (2003), p. 237.

[178] W. P. Hess and F. P. Tully. "Hydrogen-Atom Abstraction from Methanol by OH." In: *J Phys. Chem.* 93 (1989), p. 1944.

[179] I. M. Campbell, D. F. McLaughlin, and B. J. Handy. "Rate constants for reactions of hydroxyl radicals with alcohol vapours at 292 K." In: *Chemical Physics Letters* 38 (1976), p. 362.

[180] R. Overend and G. Paraskevopoulos. "Rates of hydroxyl radical reactions. 4. Reactions with methanol, ethanol, 1-propanol, and 2-propanol at 296 K." In: *The Journal of Physical Chemistry* 82 (1978), p. 1329.

[181] A. R. Ravishankara and D. D. Davis. "Kinetic rate constants for the reaction of hydroxyl with methanol, ethanol, and tetrahydrofuran at 298 K." In: *The Journal of Physical Chemistry* 82 (1978), p. 2852.

[182] D. J. Jacob, B. D. Field, Q. Li, D. R. Blake, J. de Gouw, C. Warneke, A. Hansel, A. Wisthaler, H. B. Singh, and A. Guenther. "Global budget of methanol: Constraints from atmospheric observations." In: *Journal of Geophysical Research D: Atmospheres* 110 (2005), p. 1.

[183] C. Warneke, T. Karl, H. Judmaier, A. Hansel, A. Jordan, W. Lindinger, and P. J. Crutzen. "Acetone, methanol, and other partially oxidized volatile organic emissions from dead plant matter by abiological processes: Significance for atmospheric HO(X) chemistry." In: *Global Biogeochemical Cycles* 13 (1999), p. 9.

[184] D. B. Millet, D. J. Jacob, T. G. Custer, J. A. de Gouw, A. H. Goldstein, T. Karl, H. B. Singh, B. C. Sive, R. W. Talbot, C. Warneke, and J. Williams. "New constraints on terrestrial and oceanic sources of atmospheric methanol." In: *Atmospheric Chemistry and Physics* 8 (2008), p. 6887. ISSN: 1680.

[185] J. C. Slater. "The theory of complex spectra." In: *Physical Review* 34 (1929), p. 1293.

[186] C. C. J. Roothaan. "New developments in molecular orbital theory." In: *Reviews of Modern Physics* 23 (1951), p. 69.

Annex

I List of Publications

- **Theoretical and experimental cross sections for electron scattering by halothane**
  Leticia Maioli, Marcio Bettega, Francisco Blanco, Gustavo Garcia, Emanuele Lange, Paulo Limao-Vieira, and Filipe Ferreira da Silva
  Eur. Phys. J. D **73** (2019) 181

- **The lowest-lying electronic states of isoflurane and sevoflurane in the 5.0-10.8 eV energy range investigated by experimental and theoretical methods**
  E Lange, F Ferreira da Silva, N C Jones, S V Hoffmann, D Duflot, and P Limão-Vieira
  Chem. Phys. Lett. **716** (2019) 42 – 48

- **Experimental and theoretical electron scattering cross section data for dichloromethane**
  K Krupa, E Lange, F Blanco, A S Barbosa, D F Pastega, S d'A Sanchez, M H F Bettega, G García, P Limão-Vieira, and F Ferreira da Silva
  Phys. Rev. A **97** (2018) 042702-1 - 042702-8.

- **Elastic Differential Cross Sections for Electron Scattering with Dichloromethane**
  E Lange, K Krupa, J Ameixa, A S Barbosa, D F Pastega, P Limão-Vieira, M H F Bettega, F Blanco, G García, F Ferreira da Silva
  J. Phys. Conf. Series **875** (2017) 062036-1

- **Valence and lowest Rydberg electronic states of phenol investigated by synchrotron radiation and theoretical methods**
  P Limão-Vieira, D Duflot, F Ferreira da Silva, E Lange, N C Jones, S V Hoffmann, M A Śmiałek, D B Jones and M J Brunger
  J. Chem. Phys. **145** (2016) 034302-1 - 034302-11.

- **Combined experimental and theoretical study on the differential elastic scattering cross sections for acetone by electron impact energy of 7.0 to 50 eV**
  D F Pastega, E Lange, J Ameixa, A Barbosa de Souza, F Blanco, G García, M H F Bettega, P Limão-Vieira, F Ferreira da Silva
  Phys. Rev. A, **93** (2016) 032708-1 – 032708-7.

- **Electronic Excitation of Furfural as probed by High-Resolution Vacuum Ultraviolet Spectroscopy, Electron Energy Loss Spectroscopy and ab initio Calculations**
  F Ferreira da Silva, E Lange, P Limão-Vieira, N C Jones, S V Hoffmann, M-J Hubin-Franskin, J Delwiche, M J Brunger, R F C Neves, M C A Lopes, E M de Oliveira, R F da Costa, M T do N Varella, M H F Bettega, F Blanco, G García, M A P Lima, and D B Jones
  J. Chem. Phys., **143** (2015) 144308-1 – 144308-13.

- **Electron induced fragmentation of sulphur containing biological prototypes: thiaproline and taurine**
  E Lange, G Meneses, T Cunha, J Krasuska, J Kopyra, G García, F Ferreira da Silva, P Limão-Vieira
  J. Phys. Conf. Series, **635** (2015) 072069.